



HAL
open science

Guidance navigation and control solutions for unmanned heterogeneous vehicles during a collaborative mission

David Vissière

► **To cite this version:**

David Vissière. Guidance navigation and control solutions for unmanned heterogeneous vehicles during a collaborative mission. Mathematics [math]. École Nationale Supérieure des Mines de Paris, 2008. English. NNT : 2008ENMP1540 . pastel-00004492

HAL Id: pastel-00004492

<https://pastel.hal.science/pastel-00004492>

Submitted on 22 Dec 2008

HAL is a multi-disciplinary open access archive for the deposit and dissemination of scientific research documents, whether they are published or not. The documents may come from teaching and research institutions in France or abroad, or from public or private research centers.

L'archive ouverte pluridisciplinaire **HAL**, est destinée au dépôt et à la diffusion de documents scientifiques de niveau recherche, publiés ou non, émanant des établissements d'enseignement et de recherche français ou étrangers, des laboratoires publics ou privés.

DAVID VISSIERE

GUIDANCE, NAVIGATION,
AND CONTROL SOLUTIONS
FOR UNMANNED
HETEROGENEOUS
VEHICLES IN A
COLLABORATIVE MISSION

DAVID VISSIERE

École Nationale Supérieure des Mines de Paris, Centre Automatique et
Systèmes, 60, Bd. Saint-Michel, 75272 Paris Cedex 06, France.

E-mail : david.vissiere@polytechnique.org

Key words and phrases. — Unmanned, autonomous vehicles, navigation, guidance, control, UAV, UGV, pedestrian, Kalman filter, extended Kalman filter, data fusion, observer, parameter estimation, path planning, trajectory generation.

Mots clés. — Autonomie, véhicule autonome, navigation, guidage, pilotage, contrôle, véhicule aérien autonome, véhicule terrestre autonome, soldat, fantassin, filtre de Kalman, filtre de Kalman étendu, fusion de données, observateur, estimation de paramètres, planification de trajectoire, génération de trajectoire.

July 30, 2008

**GUIDANCE, NAVIGATION, AND
CONTROL SOLUTIONS FOR
UNMANNED HETEROGENEOUS
VEHICLES IN A COLLABORATIVE
MISSION**

DAVID VISSIERE

Résumé (Solution de guidage navigation pilotage pour véhicules autonomes hétérogènes en vue d'une mission collaborative)

L'application classique des techniques d'estimation et de contrôle, basées sur des capteurs de haute performance, à des systèmes utilisant des capteurs de performances médiocres mais adaptés aux besoins nouveaux des troupes légères et à leurs contraintes est un enjeu pour l'avenir. Le travail présenté dans ce mémoire concerne le développement et l'application expérimentale de solutions de guidage-navigation-pilotage à de tels systèmes.

Nous étudions d'abord le cas d'un robot terrestre sur lequel nous apportons une preuve de convergence pour une technique d'évitement d'obstacle décentralisée. Nous implémentons expérimentalement avec succès un algorithme de planification de trajectoire hors ligne dont nous utilisons les résultats en temps réel pour réaliser, via un estimateur non linéaire, un bouclage par retour dynamique.

Dans un deuxième temps, nous mettons en évidence l'aspect critique lié au système informatique embarqué temps-réel nécessaire pour pouvoir envisager un vol autonome sur une plate-forme aérienne instable du type hélicoptère. Nous décrivons le système que nous avons développé et l'électronique embarquée utilisée. Ce système permet d'obtenir, avec une fiabilité et une fréquence suffisante, l'ensemble des informations des capteurs et sert à calculer des lois de commande.

Le développement d'un modèle rigoureux pour notre hélicoptère échelle réduite s'est fait en 3 étapes successives, nous nous sommes d'abord basés sur les études proposés dans la littérature pour élaborer un premier modèle dynamique d'hélicoptère modèle réduit, puis, dans un deuxième temps, nous avons construit un estimateur d'état incluant ce modèle dynamique de l'engin, recalé par les capteurs. Les résultats de filtrage obtenus ont permis dans un troisième temps d'améliorer le modèle par des phases successives d'identification et de réglages. L'implémentation en temps-réel de l'estimateur sur le calculateur embarqué a été réalisée ensuite ainsi que la stabilisation.

Les erreurs d'estimation du cap lors de l'utilisation des différentes plate-formes (terrestre comme aérienne) nous ont guidé vers une utilisation nouvelle du champ magnétique ou plutôt de ses perturbations. Par une technique que nous exposons nous montrons comment utiliser les perturbations du champ magnétique pour améliorer considérablement l'estimation de position d'une centrale bas-coût au point qu'elle devient un instrument de localisation.

CONTENTS

Introduction	5
Contexte, historique	7
Présentation du rapport	11
Introduction	11
Travail sur les véhicules terrestres	12
Travail sur les hélicoptères	14
Travail sur le podomètre du fantassin	15
Conclusion et perspectives	15
Part I. Control of unmanned ground vehicles	17
1. Issues in unmanned mobile systems	19
1.1. Non-holonomic systems and underactuated systems	19
1.2. Trajectory tracking and path tracking	20
1.3. Some known issues	21
1.4. Dynamic inversion	22
1.5. Multivehicle cooperative control	23
2. Guidance, navigation, control, and obstacle avoidance for a UGV	25
2.1. Introduction	26
2.2. Experimental testbed	27
2.3. Vehicle dynamic model	28

2.4. Decentralized obstacle avoidance algorithm	28
2.5. Trajectory generation	38
2.6. Dynamic feedback control law and indoor results	41
2.7. Trajectory and state reconstruction, outdoor results	42
2.8. Future directions	44
Part II. Navigation and control solutions for an experimental VTOL UAV	47
3. An embedded real-time navigation system	49
3.1. Introduction	49
3.2. Requirements	51
3.3. Sensors performances and protocols	53
3.4. MPC555 micro-controller : sensors and actuators interface ..	55
3.5. Embedded PC : computation board	56
3.6. Successive iterations and issues raised	58
4. Autonomous flight of a small-scale helicopter using a model- based observer	63
4.1. Introduction	64
4.2. Experimental small-scale helicopter	66
4.3. Experimental setup, vibrations and electrical issues	70
4.4. Small-scale helicopter: rigid-body model	75
4.5. Small-scale helicopter: rotor dynamics	79
4.6. Small-scale helicopter: tail rotor	87
4.7. Modeling improvements, Filter design	88
4.8. Experimental estimation results	98
4.9. Stabilization in hovering mode	104
4.10. Future directions	106
Part III. Positioning techniques using magnetic field disturbances	113
5. Taking advantage of magnetic-field disturbances in navigation	115
5.1. Introduction	116
5.2. Problem statement	120

5.3. Using magnetic field gradients increase observability	123
5.4. A possible filter design	125
5.5. Gain in observability	130
6. Direct measurement of magnetic-field gradients for navigation	137
6.1. Introduction	137
6.2. Measuring magnetic fields gradients to derive velocity	138
6.3. Gain of observability	140
6.4. Filter design and experimental results	148
6.5. Future directions	150
Bibliography	155

INTRODUCTION

CONTEXTE, HISTORIQUE

Quand j'ai commencé ce travail en Août 2004, les activités liées aux drones connaissaient leur plein envol aux Etats Unis et commençaient à intéresser fortement les européens.

La Délégation Générale pour l'Armement (DGA) par l'intermédiaire de plusieurs plans d'étude amont (PEA) a souhaité développer son expertise sur les systèmes de navigation embarquables sur des engins de petite taille.

L'utilisation de capteurs de performance médiocre, légers et peu coûteux correspond à un besoin nouveau des forces à destination des troupes légères. Il est très vite apparu que les techniques traditionnelles de contrôle-commande, basées sur des capteurs de haute performance, utilisant des algorithmes complexes mais éprouvés ne permettraient pas de répondre aux besoins pour des engins légers, sensibles aux perturbations, disposant d'une charge utile réduite.

Dès 2004 les résultats du premier challenge mini drones du concours DGA ONERA ont montré les difficultés liées aux systèmes échelle réduite.

On a pensé à tort qu'il serait plus facile de donner de l'autonomie à des engins de taille réduite.

Pour le Laboratoire de Recherches Balistiques et Aérodynamiques (LRBA), centre de la défense expert en systèmes de navigation, la compréhension des difficultés liées à ces systèmes est devenu un enjeu d'avenir.

De 2004 à 2007 j'ai eu l'occasion de travailler sur la problématique des systèmes de navigation bas-coût dans le cadre d'une collaboration entre le LRBA et l'ENSMP, et de faire ainsi un thèse sur cette problématique

nouvelle.

Le plan de mon exposé suivra l'évolution de nos travaux de 2004 à 2007. Je dis nous car j'ai eu la chance d'être entouré d'une équipe compétente, tant au niveau du LRBA où m'ont rejoint Johann Forgeard technicien Pilote, Alain Pierre Martin ingénieur expert en navigation, Pierre Finance ouvrier spécialisé et où j'ai encadré de nombreux stagiaires sur ce projet (Eric Dorveaux, Nicolas Douziech, Alain Vissière, Sebastien , Emmanuel Chaplais, Quentin Desile, Pierre-Jean Bristeau) que du côté de l'Ecole des Mines avec un environnement particulièrement simulant sur le plan scientifique avec Philippe Martin et son doctorant Erwann Salaun, qui continuent à travailler sur les drones, Jonathan Chauvin, Laure Sinègre, Silvere Bonnabel avec qui j'ai partagé les tables du labo, Pierre Rouchon qui m'a permis de découvrir l'Automatique à l'Ecole Polytechnique il y a 8 ans, et enfin Nicolas Petit qui m'a encadré, supporté et soutenu depuis mon stage de fin d'étude sous sa tutelle en 2002 à la raffinerie de Feyzin (Total).

Au delà du cadre de travail exceptionnel, c'est un environnement particulièrement motivant et agréable qui m'a été offert.

Mon premier support de travail a été le robot mobile Pioneer. Il m'a permis d'appliquer un certain nombre de méthodes liées à la boucle guidage-navigation-pilotage, mais surtout de mesurer l'étendue des difficultés liées à la mise en place expérimentale d'un développement réalisé en simulation et la pertinence de l'expérience. Il aura fallu en pointillé presque 2 ans pour avoir un modèle réaliste du Pioneer, trouver et prouver une méthode d'évitement d'obstacle décentralisée efficace, réaliser un filtre non linéaire d'estimation de trajectoire satisfaisant, un bouclage par retour dynamique et mettre en place une méthode efficace de planification de trajectoire. Implémenter l'ensemble sur la plateforme expérimentale a représenté une lourde tâche. La plupart des résultats ont été publiés dans l'article [83].

Les difficultés liées au reverse engineering sur le Pioneer équipé d'origine d'un système informatique embarqué avec un OS Linux, l'expérience du CAS acquise sur le concours DGA où il obtient les 1ère et 4ième places,

la criticité enfin des flots de données dans le cadre d'une plateforme aérienne m'ont conduit à développer mon propre système informatique temps-réel embarqué pour les applications liées aux véhicules autonomes. Avec Johann Forgeard deux ans ont été nécessaires pour mettre au point les 3 versions successives de la carte électronique embarquée, du logiciel temps-réel d'acquisition des données sur micro contrôleur et de la carte de calcul. L'ensemble fonctionnant en temps-réel avec moins de 1 trames de perdue pour 1000 envoyées et jamais plus de deux d'affilée. Ces travaux ont fait l'objet de la publication [90].

En parallèle du travail mené sur le système informatique embarqué temps-réel nous avons travaillé avec Alain Pierre Martin sur la mise au point d'un observateur type EKF pour estimer l'état de l'hélicoptère ainsi que sur le développement d'un modèle précis d'hélicoptère échelle réduite, pour la commande, mais aussi et surtout pour améliorer l'estimation d'état. Un premier essai en extérieur a été fait en avril 2006, les résultats de l'estimateur étaient alors insuffisants. Avec Pierre-Jean Bristeau qui pour son travail durant son stage a obtenu le grand prix d'option de l'École Polytechnique, nous avons mis au point un modèle plus précis pour l'hélicoptère utilisé et développé le filtre final aujourd'hui embarqué. Ce travail a fait l'objet de la publication [82]. Ce projet m'aura demandé 2 ans de travail et des compétences portant sur plusieurs disciplines difficiles à mettre en oeuvre.

Au printemps 2006, une visite lors du salon Eurosatory au stand de Vectronix m'a fait prendre conscience de l'absence de solution de positionnement en intérieur pour les applications militaires. Durant l'été puis l'automne, nous avons travaillé avec Alain Pierre Martin au développement d'une nouvelle solution, en reproduisant d'abord celle de Vectronix. L'utilisation des magnétomètres et les difficultés que nous avons rencontrées avec l'hélicoptère (notamment pour l'estimation du cap), montraient l'existence de perturbations importantes du champ magnétique en particulier en intérieur. Nous avons alors eu l'idée d'utiliser le champ magnétique, ou plutôt ses gradients, qui sous l'hypothèse d'un champ stationnaire relie le champ magnétique à la vitesse du corps.

Cette découverte a fait l'objet d'un dépôt de brevet de notre part [86] et les résultats et méthodes employées ont été publiés dans [84] et [85].

Il semble aujourd'hui que si les difficultés liées aux systèmes de navigation bas-coût peuvent être surmontées par une étude technique rigoureuse et des algorithmes de guidage navigation pilotage performants, les défaillances liées aux capteurs notamment le GPS sont critiques, en particulier pour les engins à voilures tournantes. La recherche de solutions au problème d'estimation en prenant en compte les faiblesses capteurs est un axe de travail important, les résultats sont capitaux pour l'entrée de systèmes de navigation bas-coût en opération dans les forces.

PRÉSENTATION DU RAPPORT

Introduction

Dans ce document, nous allons mettre en perspective le travail effectué pendant les trois dernières années (2004-2007) en collaboration entre les personnels du LRBA et ceux de l'École des Mines de Paris. Nous avons cherché à développer des techniques rendant autonomes des véhicules ayant un intérêt pour les applications militaires. Les spécificités des applications envisagées sont les suivantes: environnement extérieur ou intérieur souvent incertain, besoin de véhicules de types divers, fréquente indisponibilité des signaux GPS.

Il est apparu rapidement qu'un important travail de validation expérimentale serait nécessaire pour nous permettre de proposer des solutions réalistes. A cette fin nous avons décidé de considérer trois types de locomotion: véhicule à roues, véhicule aérien à voilure tournante, piéton.

Nous avons développé une technologie commune de système embarqué dont les performances sont compatibles avec les trois cas envisagés. Ces travaux ont fait l'objet de la publication [90]. Puis, nous avons étudié chacun des systèmes de locomotion en soulignant les difficultés et en proposant des méthodes adaptées.

Dans un premier temps, nous avons établi les spécifications des logiciels embarqués à bord des véhicules et le type d'information qui devraient être communiquées à un utilisateur distant opérant depuis une station sol.

Ensuite nous avons défini différents scénarios d'utilisations opérationnelles. Au cours de cette étude, nous avons réalisé qu'il était crucial

de mettre au point une méthode d'autonomie permettant de prendre en compte des contraintes d'évitement entre les différents engins à utiliser. Cette méthode doit aussi être adaptée à la physique de chacun des porteurs et, dans le but d'être performante, tirer parti des spécificités de leurs dynamiques.

Nous avons proposé la méthode de contrôle suivante : ramener chaque système à un simple point matériel grâce à un régulateur de bas niveau sophistiqué et adapté aux équations différentielles régissant son mouvement. Dans chaque cas, un modèle de connaissance a été considéré.

Une fois les systèmes considérés ramenés à des points matériels, on peut les intégrer dans tout type de scénarios. En particulier, dans un cadre collaboratif type ordonnancement, un véhicule est donc simplement un point matériel avec des limitations (contraintes) d'encombrement et de déplacement à vitesse et accélération limitée. Pour être pertinente dans les scénarios que nous avons définis, la méthode de contrôle doit être versatile, c'est à dire capable de prendre en compte des changements dans le scénario tel qu'un obstacle non connu à l'avance.

Travail sur les véhicules terrestres

Les véhicules Pioneer sur lesquels nous avons travaillé sont ceux du Laboratoire de Recherche en Balistique et Aérodynamique. Dans un premier temps, nous avons identifié un modèle dynamique de ces véhicules prenant la forme d'un système "uni-cycle". Ce système est "plat" [29, 30]. Ainsi, par bouclage dynamique, c'est à dire par changement de variables précédé d'une extension des équations dynamiques par des intégrateurs purs, le véhicule se ramène à la dynamique de ses sorties plates (ici son centre de gravité). La dynamique équivalente est du quatrième ordre. D'un point de vue applicatif, il est important de prendre en compte la puissance limitée des moteurs mettant en mouvement les quatre roues indépendantes. En nous inspirant de [21, 59, 74, 20, 22], nous avons développé une technique de planification de trajectoire sous contraintes, tirant pleinement partie de la platitude du système. Les contraintes sont les limitations des moteurs, auxquelles on a ajouté les obstacles connus à l'avance. Les problèmes d'optimisation sous contraintes correspondant

aux différents scénarios d'utilisation sont détaillés dans le Chapitre 2. Lorsque l'environnement est incertain, et qu'en particulier des obstacles imprévus sont détectés au cours de la mission, il est nécessaire de prendre des actions correctives immédiates. Pour cela nous avons mis au point une méthode reposant sur les "forces gyroscopiques" [17], garantissant l'évitement d'obstacles, sous des conditions analytiques que nous avons établies.

Au cours de ces travaux, nous avons pu identifier que les technologies de localisation étaient le principal frein à l'expérimentation pratique. Il est en effet indispensable de disposer d'estimations fiables des composantes de l'état du système que l'on souhaite contrôler. Cette logique vaut pour toute méthode de contrôle, y-compris celle que nous avons proposée. Nous avons donc équipé les véhicules Pioneer d'un système de localisation GPS et rajouté des capteurs odométriques dont nous avons hybridé les signaux pour obtenir une estimation fiable de la localisation des véhicules. Il s'est révélé difficile, mais faisable, de modifier le système logiciel embarqué fourni avec les véhicules afin d'y intégrer les algorithmes de fusion de données. En outre, la puissance de calcul disponible était assez faible, ce qui nous a demandé de réaliser certains autres algorithmes hors-ligne sur des machines distantes. Une autre limitation du système embarqué que nous voulons mentionner est la variabilité de la cadence d'exécution des mesures et des commandes. Elle est la source de certaines dégradations de performances qui ne sont pas critiques dans le cas du véhicule Pioneer. Dans l'avenir, nous préférerons à ce système fourni par le constructeur, notre système embarqué présenté au Chapitre 3.

En conclusion, nous avons pu, comme le montrent les résultats de planification et d'asservissement des trajectoires, mettre en œuvre avec succès notre technique. Cette méthode est performante et pertinente en raison de son faible coût en terme de moyens de calculs et par la qualité des asservissements obtenus. En dépit des limites du système temps-réel fourni avec le véhicule, les résultats ont été concluants, ce qui montre la robustesse de cette approche. Ces travaux ont fait l'objet de la publication [83].

D'un point de vue méthodologique, nous pensons que les limites du système temps-réel ne se sont pas montrées critiques dans le cas des véhicules

terrestres car ceux-ci sont assez lents et ne sont pas instables par nature. Dans le cas des véhicules aériens qui suit, la situation est très différente.

Travail sur les hélicoptères

Les véhicules aériens à voilure tournante que nous avons considérés sont des hélicoptères Vario Benzin Acrobatic dont le rotor principal mesure 1.8 m. Nous avons acheté, équipé, et instrumentés les hélicoptères Vario Benzin Acrobatic sur lesquels nous avons travaillé. Nous avons également conçu et réalisé l'ensemble du système électronique embarqué ainsi que le système temps-réel pour les raisons évoquées précédemment. Ce système, inspiré du système des robots terrestres Pioneer, utilise une architecture ouverte Linux.

Tout comme les véhicules terrestres, l'hélicoptère est un système dynamique qui se ramène, une fois stabilisé par bouclage, à un point matériel pour l'étude des algorithmes permettant un haut niveau d'autonomie. Néanmoins, il possède des différences bien marquées : il est rapide et présente un comportement instable en boucle ouverte. C'est d'ailleurs pour cette raison que nous l'avons choisi : il est capable de manœuvres agressives.

On pourra, dans un futur proche, appliquer à l'hélicoptère les mêmes techniques de planification de trajectoire (par exemple en spécifiant des points de passage en tant qu'ordres de haut niveau) et aussi en les intégrant dans des scénarios d'ordonnancement.

En revanche, pour réaliser expérimentalement la stabilisation, qui est équivalente à la transformation en un point matériel, les difficultés sont nombreuses. Une fois de plus, la localisation est un problème central. Il n'existe pas (dans la gamme des prix inférieurs à 20000 euros) de capteur permettant de mesurer avec précision l'attitude de l'hélicoptère. Or, il est important, si on veut pouvoir utiliser de manière généralisée de tels vecteurs aériens en tant que drones, de limiter les coûts de construction. Cela implique de rester dans la gamme "low-cost" (bas coût). En complément des capteurs, il est naturel d'utiliser une technique d'hybridation de données. Les performances requises en termes d'estimation de données sont assez importantes. Ceci est dû au caractère agressif de la dynamique

de l'hélicoptère. En particulier, il est important de respecter les cadences de mesures, de calcul et de commande : le système temps-réel doit être précis et non pas fluctuant. En outre, il est utile, pour obtenir une précision suffisante d'estimation, de considérer un modèle assez complet de l'hélicoptère, prenant en compte des effets aérodynamiques entres autres. Ce travail est détaillé au Chapitre 4. Il a abouti avec succès à un vol stationnaire autonome. Ils ont fait l'objet de la publication [82].

Travail sur le podomètre du fantassin

Les travaux que nous avons menés sur le déplacement des piétons à l'intérieur de bâtiments ont porté sur le développement d'une méthode nouvelle de positionnement par fusion de données magnétométriques et inertielles sans avoir recours au GPS. C'est un problème important pour les troupes d'assaut ainsi que dans de nombreuses applications civiles, comme le secours à des personnes dans des bâtiments où la visibilité est très réduite (comme lors d'incendies avec fumée épaisse notamment). La technologie GPS est inutilisable dans de telles situations et nous avons cherché à développer une méthode permettant de s'en affranchir. Ces travaux, qui ont fait l'objet d'un dépôt de brevet [86] suivi de publications [85, 84] sont également à l'origine d'un travail de recherche dans le pôle de compétitivité SYSTEM@TIC (projet LOCINDOOR).

Conclusion et perspectives

Nous pensons avoir mis en évidence une méthode générale de contrôle, utilisable dans le cadre du contrôle collaboratif d'engins hétérogènes tels que des véhicules terrestres et des engins aériens à voilure tournante. Grâce à des régulations de bas niveau, les deux types de véhicules considérés sont chacun équivalent à un point matériel et un ensemble de contraintes.

Nous avons réalisé cette transformation sur deux engins expérimentaux et il nous a fallu en construire complètement un (l'hélicoptère).

Il est crucial d'utiliser un système temps-réel dont on maîtrise l'architecture logicielle, pour pouvoir lui adjoindre des sous systèmes physiques

ou logiciels, tout en garantissant ses performances. Néanmoins aujourd’hui, nous pensons que le véritable goulot d’étranglement aux futurs progrès dans le domaine des drones et véhicules terrestres autonomes sont les capteurs et que la technologie limitant les applications est l’hybridation en vue de la localisation (au sens des systèmes dynamiques, c’est à dire la connaissance de tous les états). Dans cet esprit, nous avons travaillé à d’autres techniques, telles que la localisation magnétométrique [85], [84]. Je vais continuer à travailler, en partenariat avec le Centre Automatique et Systèmes sur le thème de l’autonomie des engins terrestres et aériens en inscrivant le travail qui va suivre dans la continuité du travail qui a été réalisé en collaboration entre le LRBA et l’Ecole des Mines de Paris.

Organisation du manuscrit. — Le manuscrit est organisé en trois parties. La première partie est consacrée aux véhicules terrestres. On présente le contexte dans lequel on souhaite les utiliser et certaines difficultés répertoriées dans la littérature qui nous ont parues essentielles au Chapitre 1. On présente les méthodes de contrôle que nous avons utilisées ou développées pour l’optimisation, le suivi de trajectoires et l’évitement d’obstacles au Chapitre 2.

La seconde partie est consacrée aux véhicules aériens. En tout premier lieu, au Chapitre 3, nous présentons le système embarqué temps-réel à deux processeurs que nous avons conçu et mis à bord de notre hélicoptère. Au Chapitre 4, nous donnons tous les détails du modèle de la dynamique du vol que nous avons utilisé dans la fusion de données multi-capteurs implémentée à bord de l’hélicoptère. Nous détaillons aussi les techniques de contrôle utilisées pour le vol stationnaire. Il s’agit ici de compenser la faible précision de mesure des capteurs bas-coûts par un modèle de connaissance de l’engin à contrôler.

La troisième partie est consacrée au système de positionnement par usage de capteurs magnétométriques distribués. Nous expliquons les principes de cette méthode innovante au Chapitre 5 et détaillons la mise en oeuvre expérimentale au Chapitre 6.

PART I

CONTROL OF UNMANNED GROUND VEHICLES

CHAPTER 1

ISSUES IN UNMANNED MOBILE SYSTEMS

Ce chapitre présente certains travaux menés dans le domaine du contrôle des véhicules autonomes que nous avons considérés (Pioneers et hélicoptères). Cette introduction vise à mettre en lumière les problèmes liés aux systèmes non holonomes, à l'asservissement de trajectoires et de chemins.

1.1. Non-holonomic systems and underactuated systems

The Pioneer vehicles under consideration in the first part of this thesis belong to a class of non-holonomic systems in which a large number of mobile robots can be found (e.g. [47, 48, 79]). This class of systems contains unicycle-type systems. Essentially, all these systems are controllable, in the sense that it is possible to steer them from one point in their state space to another. However, this controllability does not

hold to first order: it cannot be established from their approximate linearized models. Indeed, linear approximations do not allow (transverse) motions at the sides of the vehicle. These vehicles are not small-time controllable, because some maneuvers require displacements that are not asymptotically small for the same reason.

Stabilization of these systems can be difficult because of the Brockett obstruction, which states that the origin of the state space is not asymptotically stabilizable by continuous feedback. See [63, 61, 64, 65] for more details.

All of the experiments and studies described in this part of the thesis used Pioneer vehicles. These are in fact unicycle systems. Interestingly, numerous other vehicles (e.g. carangiform systems [81, 62]) could have been considered because they belong to the same class of systems.

Examples of underactuated systems can be encountered for various actuation structures. A prime example is the helicopter, which we study in the second part of this thesis.

1.2. Trajectory tracking and path tracking

To complete a mission (in particular, one of military interest), a basic control requirement is that the vehicle under consideration follows a certain path on the ground. If the timing along the path is important, then the problem is a trajectory-tracking problem. If not, it is only a path-tracking problem.

There exists a vast literature on both subjects. In numerous cases, it is assumed that the whole state vector of the system can be measured. Unfortunately, the robustness analysis problem has very few known solutions. In particular, the following issues are very rarely treated: model uncertainty, neglected dynamics (of the actuators), and ground-slipping effects. It seems important in this context to perform some representative experiments in order to validate any proposed control laws.

For trajectory tracking, two cases are usually treated separately: steady states and (non-stationary) trajectories. In the latter case, it proves very challenging to prove controllability along any trajectory. In the dual

problem of observability along a trajectory, the observability of the time-varying linear model obtained from a first-order approximation of the dynamics along a given trajectory can usually be studied by approximately evaluating the observability Gramian or, at least, estimates can be obtained for this Gramian. Under relaxed persistency conditions (see [72]), which are often difficult to guarantee in practice, it can be shown that this Gramian has full rank, which, in turn, proves observability (and, correspondingly, controllability). It may be necessary to generate large amounts of rotation of the vehicle to obtain this condition of sufficient controllability. See [44, 5, 4] for more details.

1.3. Some known issues

There is general consensus today on a list of several key issues in the practical control of non-holonomic or underactuated systems:

- a lack of robustness with respect to model uncertainties;
- frequent unnecessary maneuvers derived from approximate linear models;
- the relatively poor quality of the state information that can be obtained from specific sensors.

Indeed, we soon experienced these issues with our Pioneer vehicles and had to develop solutions for them. We now briefly sketch these solutions.

- We quickly realized that the slipping laws for the Pioneer vehicles depended greatly on the ground under consideration. We performed some indoor and outdoor identification experiments to evaluate how much authority for feedback control actuation would be necessary.
- To avoid the artifacts stemming from linearized models mentioned above, we decided to treat directly the nonlinearity of the unicycle model through its flatness property.
- To compensate for the relatively poor quality of the on-board sensors, we installed some extra sensors (including a GPS receiver) and used a data fusion algorithm. The resulting information was ultimately used in the dynamic linearizing feedback derived from the nonlinear model.

Despite the encouraging results we obtained, there were also some weaknesses in our system. In particular, we did not use any vision system, which would certainly have helped in determining position information. A vision system would certainly be very effective for simultaneous localization and mapping (SLAM) or tracking a given target as is shown in [31, 80, 38, 37, 49].

1.4. Dynamic inversion

The feed-forward terms in the control laws are of paramount importance for the systems under consideration here. These terms can be computed by inverting the model of the dynamics. For fully actuated systems, inverting the differential dynamics is straightforward. Indeed, given a set of histories of the configuration variables, the corresponding generalized forces (inputs) can be directly computed by use of the Euler–Lagrange equations. For underactuated and non-holonomic systems, this is a much more complex problem. The zero dynamics plays a key role. Given some desired histories for the outputs of the system, what can be said about the other states? A good example is provided by the PVTOL (Planar Vertical Take Off and Landing) system [53]. In its simplest form, it has three configuration variables (six states) and only two controls. A natural solution might seem to be to focus on positions only, by neglecting the rotational dynamics. Unfortunately, these dynamics are unstable, which compromises the proposed control strategy. A different approach must be considered.

Nevertheless, instability of the zero dynamics is not the most frequent case. Very often, it is possible to neglect it to simplify the control problem. By inverting the rest of the dynamics (the fully actuated part), approximate open-loop control histories can easily be determined. A closed-loop stabilizing control remains to be designed. For minimum-phase systems, a high-gain controller is a possible choice. For non-minimum-phase systems, an LQR controller can be used. See [7, 6] for more details.

More generally, we propose the following methodology. For a given system, we look for linearizing outputs (in the sense of [30, 40]) or, at least, maximum-relative-degree outputs. In this way, we reduce the

dimension of the zero dynamics as much as possible. This is the approach that we use for trajectory generation. It permits us to substantially reduce the dimensionality of the numerical schemes that may be used to solve trajectory optimization problems [74, 22]. This approach was used to determine open-loop time-optimal trajectories for the Pioneer vehicles. It could be extended to the helicopters studied in the second part of this thesis.

1.5. Multivehicle cooperative control

It is helpful, from a military viewpoint, to use several vehicles simultaneously to achieve a mission objective. Lately, cooperative control has been extensively studied by the control community. Typical two-vehicle scenarios are presented in [12, 13, 11, 46, 75].

For example, two marine vehicles may be used to obtain a map of the ocean floor. The reason for this cooperation is that marine data transmission can only be performed at a very low bandwidth. While the first vehicle moves under the sea to obtain mapping information, the second remains at the sea surface level. The relatively close range between the two vehicles allows efficient data transmission. In turn, the surface-level vehicle can send data by wireless transmission using an efficient aerial technology (i.e. with a high bandwidth).

The key problem in this scenario is that the two vehicles must remain close enough together to avoid becoming separated. It seems quite evident that a leader–follower strategy must be considered here. This is also the case in the “carrier supply” problem. In this scenario, a carrier ship is supplied by a smaller ship. The smaller ship tracks the larger one.

The respective roles of the numerous vehicles that might be under consideration in a cooperative mission might be less simple to determine than in the introductory problems discussed above. Let us consider the following scenario. A platoon of vehicles is asked to occupy an area close to the entrance to a bridge. The platoon is composed of a “leader”, who constantly keeps an eye on the entry to the bridge and can ask for firepower (bombing) in the zone if necessary to prevent an overwhelming number of enemy units from crossing the bridge; a “gunner”, who has

to remain in front of the entrance to the bridge to shoot any enemy forces who might try to cross the bridge; and a “supplier”, who goes back and forth between an ammunition storage facility and the gunner. The gunner must not move too much; he must remain in a position suitable for shooting. The leader can move to remain hidden in a safe position. At times, he must get close to the gunner to give him shooting orders and information about incoming enemy forces. Finally, the supplier must move frequently. In particular, he must always be able to reach the gunner. Once more, the mission defines the respective roles of the platoon members and who tracks whom.⁽¹⁾ In this context, all of the tools we have developed are necessary: trajectory generation, obstacle avoidance, and tracking. These are presented in the next chapter.

⁽¹⁾More details of scenarios of military interest can be found in [87, 88, 89].

CHAPTER 2

GUIDANCE, NAVIGATION, CONTROL, AND OBSTACLE AVOIDANCE FOR A UGV

Dans ce chapitre nous détaillons les méthodes développées et implémentées expérimentalement sur un robot mobile dont le modèle est celui d'un unicycle. En utilisant une technique d'inversion dynamique (flatitude ici), on calcule une trajectoire optimale en boucle ouverte dont le suivi est assuré au moyen d'un retour d'état dynamique. En présence d'obstacles imprévus le contrôle découle de l'utilisation de forces gyroscopiques. Des résultats expérimentaux sont présentés ainsi qu'une preuve théorique d'évitement d'obstacle.

In this chapter, we report results of investigations conducted on a mobile robot. The vehicles under consideration were in fact similar to unicycles. We investigated a flatness-based approach (combining open-loop optimization and closed-loop tracking) and gyroscopic-force control laws. Experimental results are presented. A theoretical proof of obstacle avoidance for a gyroscopic scheme is also presented.



FIGURE 2.1. A typical coordinated airborne and ground platoon as envisioned in the BOA projet. ©BD MEDIAS for Délégation Générale pour l'Armement (DGA).

2.1. Introduction

We focus on a simple military-type scenario. This consists of a problem of reaching a single target, possibly by following a prescribed path. One or several obstacles may be encountered. These obstacles are unknown, but their size has an upper bound. The control laws that we propose have to deal with the constraints on the input to the vehicles and the mission objectives, and have no information from outside once the mission is started. Onboard sensors are the sole source of information available for avoiding unknown obstacles. In this chapter, we focus on two different control techniques, which we would like to combine in future work. The first is an offline optimal trajectory generation technique complemented by a real-time closed-loop controller. The second is a local obstacle avoidance technique using gyroscopic forces, as presented in [17].

Combining the two approaches could be done in the following way. Before an obstacle is encountered, the vehicles should track in a closed-loop manner (using onboard sensors) the optimal trajectory computed during the mission preparation phase. When an obstacle is detected, the control should switch to the obstacle avoidance phase, where the vehicle slows down and passes by the obstacle. Once a point on the initial trajectory is approximately reached again, the controller should switch back to the first control phase. Certainly, designing appropriate switching strategies will not be an easy task and will require further investigation.

The chapter is organized as follows. In Section 2.1, we briefly describe the envisioned scenario. Section 2.2 presents the vehicle under consideration (a Pioneer IV from MobileRobotsTM) and the onboard systems (including the CPU and sensors). The dynamics of the vehicle, given in Section 2.3, is the same as that of the unicycle. In Section 2.4, we consider gyroscopic-force controllers. We give details of experimental results obtained using second-order schemes (from the literature [17]). A known problem is the possibility of zero-velocity collisions (pointed out at early on in [17]). For that reason, we propose a first-order controller and actually prove a new result concerning convergence under assumptions on the size of the obstacle. This constructive proof could serve as a guideline for tuning. A generalization to second order systems could be considered by a dynamic extension. In Section 2.5, we use the flatness property of this controller to parameterize and optimize its trajectories. Constrained minimum-time problems are considered. Then, as presented in Section 2.6, we use dynamic linearizing feedback for tracking purposes. Experimental results are presented. The presented methodology was also tested outdoors; Section 2.7 describes the observer implemented on board, and experimental results are detailed.

2.2. Experimental testbed

Our experimental testbed includes three MobileRobotsTM Pioneer IV-AT vehicles similar to the one depicted in Figure 2.2. These vehicles have 4 electrically powered independent wheels and are capable of running outdoor. The onboard system consists of a Pentium III 800 MHz

based PC104 system running under Linux, 16 sonars (8 forward and 8 rear) located on the sides of the main frame (above the wheels), a one-axis gyroscope, and a wireless network adapter. It is possible to derive positioning information from odometers. Each vehicle is equipped with in-wheels 100 tick encoders with inertial correction to compensate for skid steering. By default, the vehicle does not possess any GPS. We decided to install a uBloxTM TIM-LR with added antenna. As will be detailed next, we designed our own filter for GPS/odometer/gyroscope hybridation.

2.3. Vehicle dynamic model

Assuming wheels on the same side of the vehicle have the same velocity (i.e. the vehicle behaves like a tank) it is possible to model the dynamics under the nonholonomic unicycle form studied in [36, 77]

$$(1) \quad \begin{cases} \dot{x} = \frac{(v_1 + v_2)}{2} \cos \theta, & \dot{y} = \frac{(v_1 + v_2)}{2} \sin \theta, \\ \dot{\theta} = \frac{(v_2 - v_1)}{2l} \end{cases}$$

where x , and y denote the position of the vehicle, θ denotes its orientation angle, and v_1 , and v_2 are the speeds of the left side and right side wheels, respectively. This model can be experimentally validated with fitted coefficient $l = 294$ mm. Indoor maneuvers are consistent with motions calculated through numerical integration of (1). Typical errors indoor are of 10 cm for a 4 m wide curves and straight lines trajectory over 60 s.

2.4. Decentralized obstacle avoidance algorithm

We first take into account obstacles that are not known in advance. Though it is possible to update the optimal path along the way (e.g. in a receding horizon fashion), once an obstacle is discovered, we prefer to use a control law dedicated to deal with these obstacles found at close range. An ideal candidate is the so-called “gyroscopic forces” law [17, 18]. As will appear next, while being very effective and simple to implement, they

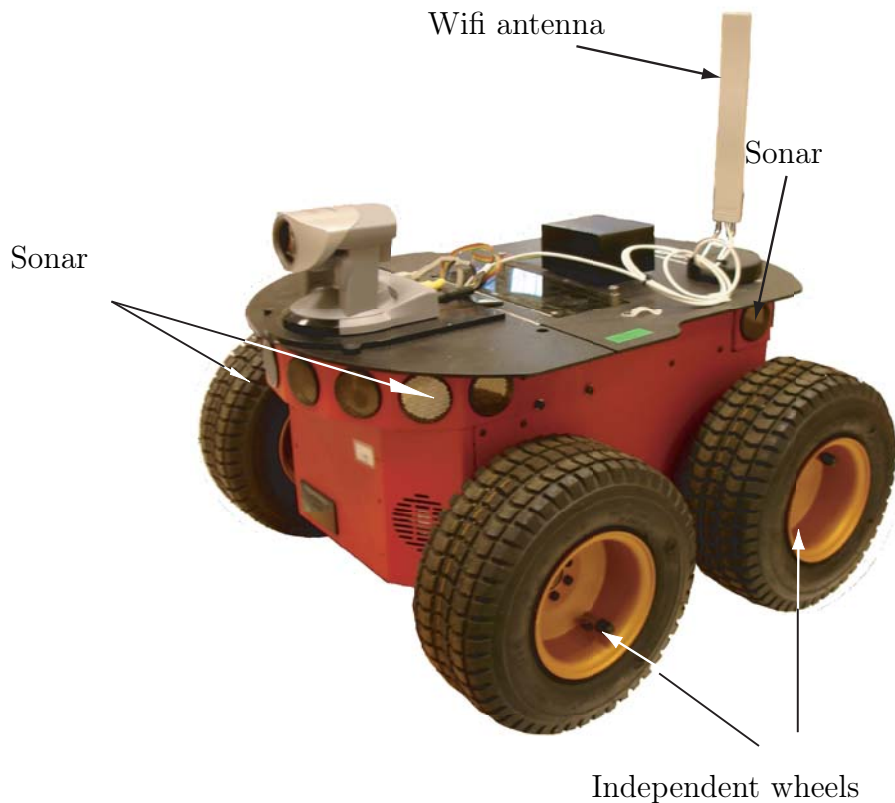


FIGURE 2.2. Pioneer IV vehicle (side view and front view). Four independent wheels, with 16 sonars, one axis gyroscope, odometers, wireless datalink, and onboard CPU.

do not guarantee collision avoidance. In the following, after recalling the fundamentals of this technique, we propose an alternate formulation (first order) for which we prove convergence and obstacle avoidance.

2.4.1. Notations. — We consider a vehicle, a target and a single circular obstacle that must be avoided. In the following, we note R the

obstacle radius, r the detection radius, A the center of the obstacle, B the most distant point from the origin in the disc $C(A, r)$, $q = (x, y)^T$ the position of the center of gravity of the vehicle, q_T the target point. Further, dq denotes the vector difference between q and its orthogonal projection onto the obstacle.

$$dq \triangleq (A - q) \frac{\|A - q\| - R}{\|A - q\|} \in \mathbb{R}^2$$

ε is a scalar valued function defined by

$$q \mapsto \varepsilon(q) = \begin{cases} -\text{sign } \det(q_T - q, dq) \\ \quad \text{if } \|dq\| \leq (r - R) \\ \quad \text{and } |\arg(q - q_T)| \leq \arcsin(R/OA) \\ 0 \quad \text{otherwise} \end{cases}$$

We use V_{\max} a (positive) avoidance constant. Two geometric points play a particular role in the convergence analysis. These are noted T_1 , and T_2 (see Figure 2.4). They are located at the intersections of the circle $C(A, R)$ and the two tangent lines originating in 0. Finally, we note $H = (OA) \cap C(A, R)$.

2.4.1.1. Proposed gyroscopic scheme. — The second order scheme usually reported in the literature is given in (2) (where \wedge stands for the logical AND)

$$\ddot{q} = \begin{pmatrix} -2 & -w(q, \dot{q}) \\ w(q, \dot{q}) & -2 \end{pmatrix} \dot{q} - (q - q_T)$$

with w given in (2).

(2)

$$w(q, \dot{q}) = \begin{cases} \frac{\pi V_{\max}}{d(q)} & \text{if } \{d(q) \leq r\} \wedge \{d(q) \cdot \dot{q} > 0\} \wedge \{\det(d(q), \dot{q}) \geq 0\} \\ -\frac{\pi V_{\max}}{d(q)} & \text{if } \{d(q) \leq r\} \wedge \{d(q) \cdot \dot{q} > 0\} \wedge \{\det(d(q), \dot{q}) < 0\} \\ 0 & \text{otherwise} \end{cases}$$

We tested this method in practical experiments with good success. Typical obtained (closed-loop) trajectories are reported in Figure 2.3. The method appears to be quite sensitive to sensor noises. There can be

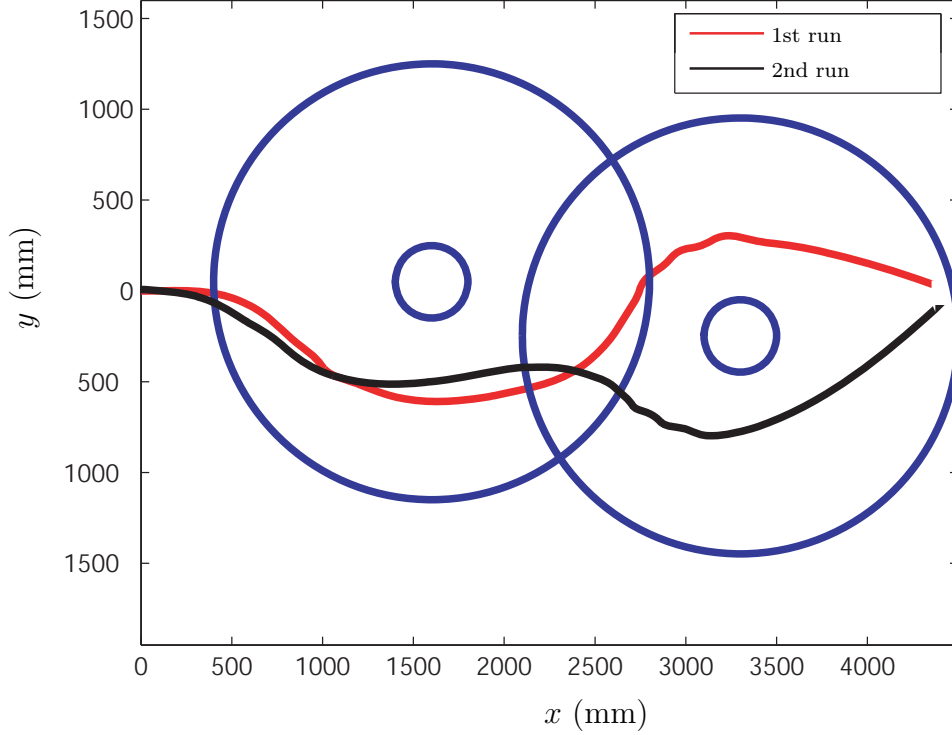


FIGURE 2.3. Indoor experimental results using gyroscopic forces. Circular obstacles are represented with their detection shells. Trajectories can bifurcate due to measurement noises.

some bifurcations as observed in this same figure, depending which side of the vehicle the obstacle is first detected on. Simulation results proposed in [17, 18] are also very interesting and show the versatility of the approach. But, there are possibilities of zero velocity collisions (one can refer to [17] for a discussion on this). These are unacceptable in practice because they would result in a complete stop of the vehicle. To address this problem, we propose a first order scheme and actually prove its convergence. It should be soon tested on the experiment.

2.4.2. Obstacle avoidance result. — Our goal is to prove that under a condition on V_{\max} , irrespective of initial conditions, the following differential equation has a unique solution that exponentially converges

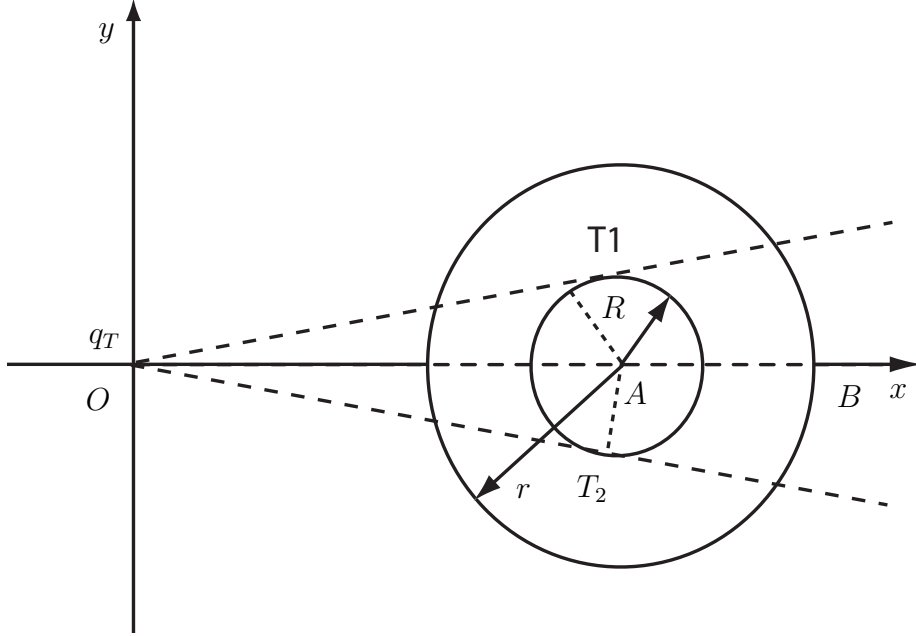


FIGURE 2.4. Notations for gyroscopic forces control law.

toward the target without intersecting the obstacle

$$\dot{q} = (q_T - q) + \varepsilon(q)V_{\max} \begin{pmatrix} 0 & -1 \\ 1 & 0 \end{pmatrix} (q_T - q)$$

For sake of analysis, the target is set to 0 and the obstacle center position is set to $(1, 0)$. Other configurations can be easily obtained by appropriate homothetic transformation, translation and/or rotation. Under this simplifying assumption, we are left with the following equation

$$(3) \quad \dot{q} = \begin{pmatrix} -1 & \varepsilon(q)V_{\max} \\ -\varepsilon(q)V_{\max} & -1 \end{pmatrix} q$$

The proof is organized as follows. As can be easily seen, the system is globally exponentially stable in the absence of the obstacle. First, we analyse the convergence to zero of (3). This results in Proposition 1. Then, we construct a positively invariant set Δ (see Definition 1) which excludes the obstacle. In a first move, we focus on a particular trajectory that serves as a boundary for Δ . We prove that, under an explicit

tuning condition, this trajectory does not intersect with the obstacle in Proposition 2. Finally, we prove in Theorem 1 that Δ is positively invariant by Equation (3), and that, eventually, every trajectory starting in Δ converges to the target.

Proposition 1. — *Every trajectory of (3) asymptotically converges to 0.*

Proof. — Note $V(q) = \frac{1}{2}\|q\|^2$. It follows that

$$(4) \quad \begin{aligned} \dot{V}(q) &= \langle q, -q - \varepsilon(q)V_{\max} \begin{pmatrix} 0 & -1 \\ 1 & 0 \end{pmatrix} q \rangle \\ &= -2V(q) \end{aligned}$$

and, then,

$$(5) \quad \|q(t)\| = \|q(0)\| \exp(-t)$$

which proves the result. \square

A more difficult task is to guarantee that trajectories do not collide with the obstacle. We now construct a set being positively invariant by (3). Its boundaries are a particular trajectory on one side, and its symmetric curve on the other side. To prove that it does not contain trajectories intersecting the obstacle, we compute lower bounds on angles of rotation and conclude by contradiction. This constructive proof yields a sufficient lower bound on V_{\max} .

2.4.2.1. A particular trajectory \mathcal{T} . — We consider \mathcal{T} the trajectory originating in B (see Figure 2.4), i.e. the set of points $q(t)$, $t \in [0, +\infty[$ solution of (3), with $q(0) = B$. Equation (3) can be analytically solved under the form

$$(6) \quad q(t) = (1 + r) \exp(-t) \exp(-\iota(t\varepsilon(q)V_{\max}))$$

This trajectory does not intersect the tangent line (OT_1) . It can not cross the bisecting line (OA) either. To do so, the argument of q need to decrease. Yet, in this zone of the plane, the argument is strictly increasing as can be seen in Equation (6) with $\varepsilon = 1$. In summary, \mathcal{T} entirely lies in the inner sector $((OT_1), (OA))$. This allows us to introduce the following definition.

Definition 1. — We denote by Δ the complementary set of the interior of the closed curve constructed with \mathcal{T} and the curve symmetrical to it with respect to the bisecting line (OA) . Δ is a closed subset of \mathbb{R}^2 .

As we will prove it, Δ is positively invariant by Equation (3). Provided that the initial condition is chosen inside Δ , the trajectory avoids the obstacle. To prove this point, we need to show that the obstacle has an empty intersection with Δ .

2.4.2.2. A property of \mathcal{T} . —

Proposition 2. — Trajectory \mathcal{T} does not intersect the obstacle provided the following inequality holds

$$(7) \quad V_{\max} \geq \sqrt{\frac{-1}{2} + \sqrt{\frac{1}{2} + \frac{\pi^2 R^2}{\log^2\left(\frac{1+r}{1+R}\right)}}$$

Proof. — We proceed by contradiction. Assume that the trajectory intersects the circle $C(A,R)$. Then, there exists a unique first-time intersection $(t_2, q_2) \in \mathbb{R}^+ \setminus 0 \times \mathbb{R}^2$ such that $q_2 = q(t_2)$ solution of (3) is on $C(A, R)$. Also, there exists a unique $(t_1, q_1 = q(t_1)) \in \mathbb{R}^+ \setminus 0 \times \mathbb{R}^2$ defined as follows. Consider $[0, t_2] \ni t \mapsto Q(t) = \|q(t) - A\| \in \mathbb{R}$. This mapping is continuous over the compact set $[0, t_2]$. Thus, the set $Q^{-1}(r) \triangleq \{t \text{ s.t. } Q(t) = r\}$ is compact and non-empty (it contains 0 by construction). Therefore, it has a maximum element t_1 . By construction, the set $\{q(t), t \in [t_1, t_2]\}$ lies in between the two circles $C(A, R)$ and $C(A, r)$ (we call this zone the “detection shell”). We now look for a lower bound on $t_2 - t_1$ to compute a lower bound on the time spent inside the detection shell. Over $[t_1, t_2]$, the argument of $q(t)$ is increasing, as implied by (3) with $\varepsilon = -1$. Let us compute a lower bound for $\frac{\|q_1\|}{\|q_2\|}$. Consider $[0, \arcsin(R)] \ni \alpha \mapsto z(\alpha) \in \mathbb{R}$ as the module of the point of the circle $C(A, R)$ with α argument and largest module. This point is represented in Figure 2.5. Simple calculations yields

$$(8) \quad z(\alpha) = \cos(\alpha) + \sqrt{\cos^2(\alpha) + R^2 - 1}$$

Let us define \tilde{q}_2 as the intersection of the line $(0q_1)$ with $C(A, R)$. Recalling the mapping $\alpha \mapsto z(\alpha)$ is decreasing, one can derive $\frac{\|q_1\|}{\|q_2\|} \geq \frac{\|q_1\|}{\|\tilde{q}_2\|}$,

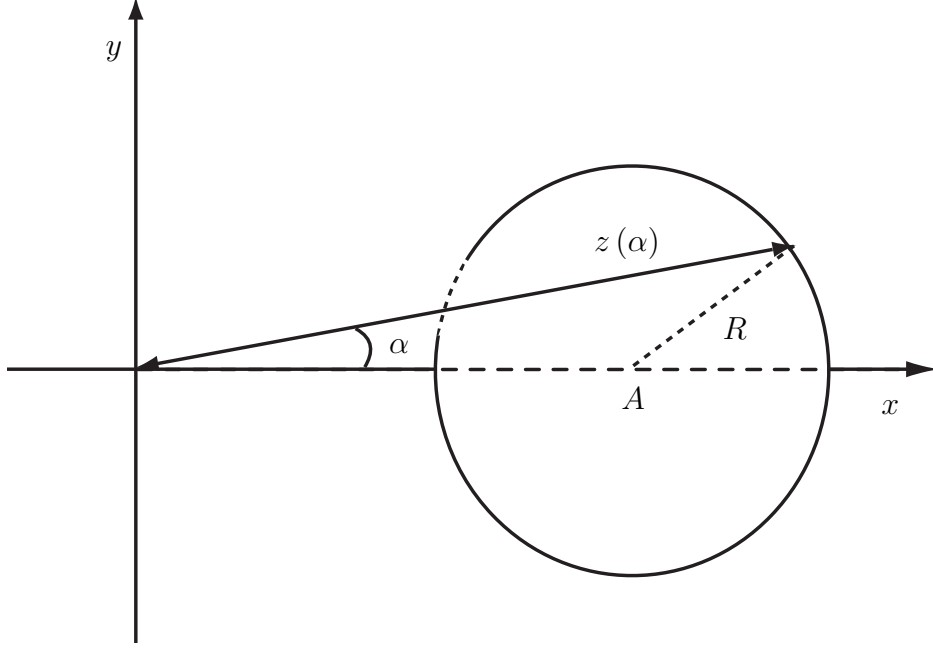


FIGURE 2.5. Notations for the gyroscopic forces control scheme.

since $0 \leq \arg(q_1) = \arg(\tilde{q}_2) \leq \arg(q_2) \leq \arcsin(R/OA)$. Further, after several lines, one can derive

$$\frac{\|q_1\|}{\|q_2\|} \geq \frac{\|\tilde{q}_2\|}{\|q_2\|} = \frac{\cos(\alpha) + \sqrt{\cos^2(\alpha) + r^2 - 1}}{\cos(\alpha) + \sqrt{\cos^2(\alpha) + R^2 - 1}} \geq \frac{1+r}{1+R}$$

Using Equation (5), we get $\frac{e^{-t_1}}{e^{-t_2}} = \frac{\|q_1\|}{\|q_2\|} \geq \frac{1+r}{1+R}$. Therefore,

$$(9) \quad t_2 - t_1 \geq \log\left(\frac{1+r}{1+R}\right)$$

Using this lower bound for the time spent in the detection shell, we now look for a lower-bound on the distance $\|q(t) - A\|$ when t varies over $[0, t_2]$. We will prove that this bound is larger than R which contradicts the intersection assumption.

Let us consider $T_{out} = t_1 + \frac{1}{V_{max}} \arcsin(R) \leq t_1 + \frac{1}{V_{max}} \frac{\pi}{2}$. When t varies from t_1 to T_{out} , the minimum distance $\min_{t \in [t_1, T_{out}]} \|q(t) - A\|^2$ from $q(t)$

to the obstacle can be lower bounded by

$$1 + \min_{t \in [t_1, T_{out}]} f(t)$$

where $f(t) = (1+r)^2 e^{-2t} - (1+r) \frac{2e^{-t}}{1+r} \cos((t-t_1)V_{\max})$. By construction, T_{out} provides a rotation which guarantees that $q(T_{out})$ reaches (OT_1) . Then, one must have $f(T_{out}) \geq f(t_2)$. Therefore, f reaches its minimum in the open interval $]t_1, T_{out}[$. The unique minimum t_{min} satisfies $\dot{f}(t_{min}) = 0$, i.e.

$$(1+r)e^{-t_{min}} = \cos((t_{min} - t_1)V_{\max}) + \sin((t_{min} - t_1)V_{\max})V_{\max}$$

After several lines, one finally derives

$$\min_{t \in [t_1, T_{out}]} f(t) = (1 + V_{\max}^2) \sin^2((t_{min} - t_1)V_{\max})$$

Now, one can choose to set

$$V_{\max} \geq \sqrt{\frac{-1}{2} + \sqrt{\frac{1}{2} + \frac{\pi^2 R^2}{2 \log^2(\frac{1+r}{1+R})}}}$$

By definition, $r > R$, and thus, $0 < \log(\frac{1+r}{1+R})V_{\max}$. From here, we can consider two exclusive situations. Either $\log(\frac{1+r}{1+R})V_{\max} > \pi/2$ (case 1), or $\log(\frac{1+r}{1+R})V_{\max} \leq \pi/2$ (case 2). In the first case, the total rotation over the time interval $[t_1, t_2]$ guarantees that the trajectory reaches (OT_1) . The trajectory does not enter the circle. In the second case, we proceed as follows. By construction of t_1 and t_2 , $t_{min} \geq t_2$. By Equation (9), $t_{min} - t_1 \geq \log(\frac{1+r}{1+R})$. A lower bound for $f(t)$ is thus given by

$$\min_{t \in [t_1, T_{out}]} f(t) \geq 2(V_{\max}^2 + 1) \sin^2(\log(\frac{1+r}{1+R})V_{\max})$$

Using that $x \geq \sin(x) \geq \frac{2}{\pi}x$ for $x \in [0, \frac{\pi}{2}]$, we derive the following lower bound for $f(t)$ on $[t_1, t_2]$

$$\min_{t \in [t_1, T_{out}]} f(t) \geq R^2$$

This contradicts the existence of an intersecting point q_2 . Both cases are inconsistent with the original intersection assumption. This concludes the proof. The proposed condition (7) guarantees obstacle avoidance. \square

We are now interested in the trajectories originating in the line sector (OA, OT_2) . We remark from (6) that the argument is always decreasing along these, and that the norm is also always decreasing. Let us consider

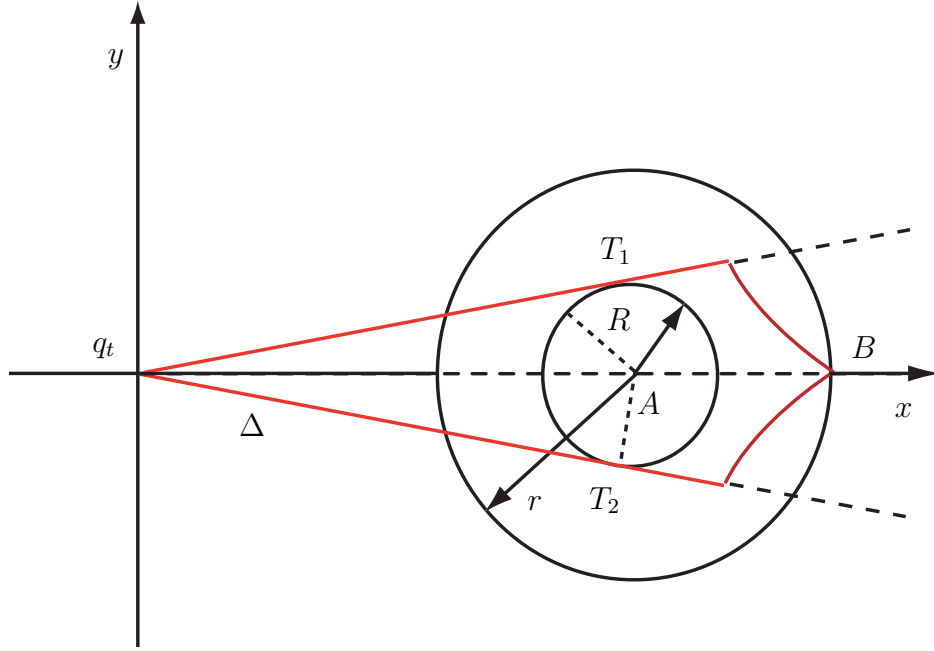


FIGURE 2.6. Invariant set and limit trajectories.

a given point in the line sector (OA, OT_2) , outside Δ and look for the trajectory originating at this point.

Definition 2. — We note \mathcal{S} the symmetry with respect to the horizontal axis (Ox) .

Proposition 3. — Consider a point M strictly below the x axis and outside Δ . Consider $\mathcal{S}(M)$. The trajectory $\mathcal{T}(M)$ originating in M is symmetrical to the trajectory originating in $\mathcal{S}(M)$. We have

$$\mathcal{S}(\mathcal{T}(M)) = \mathcal{T}(\mathcal{S}(M))$$

Proof. — The symmetry \mathcal{S} has an analytical expression:

$$\mathcal{S} \begin{pmatrix} x \\ y \end{pmatrix} = \begin{pmatrix} x \\ -y \end{pmatrix}$$

The differential Equation (3) shows a difference in ε when one crosses the x axis. For all $t \geq 0$, we note $\mathcal{T}_t(M)$ the point of the trajectory initiated in M after time t . For all $t \geq 0$, we have

$$\begin{aligned} & \mathcal{S}(\mathcal{T}_t(\mathcal{S}(M))) \\ = & \mathcal{S} \left(\int_0^t \begin{pmatrix} -1 & \varepsilon_M(t)V_{\max} \\ -\varepsilon_M(t)V_{\max} & -1 \end{pmatrix} \begin{pmatrix} x_M \\ -y_M \end{pmatrix} \right) \\ = & \mathcal{T}_t(M) \end{aligned}$$

Let us now consider a trajectory starting from a point below the x axis. Using the result above and (2), we can deduce that the trajectory does not intersect the boundary of Δ . The obstacle is thus avoided. \square

Theorem 1. — *Consider Equation (3). Provided that V_{\max} satisfies (7), and that the initial condition is chosen inside Δ , the trajectory avoids the obstacle and exponentially reaches the target 0.*

Remark 1. — *The 3-D case is covered by this obstacle avoidance method. In the 2-D plane defined by the target point on the 3-D trajectory and the velocity at the first time the vehicle detects an obstacle, the obstacle avoidance problem has as solution the one presented above.*

2.5. Trajectory generation

2.5.1. Open-loop design. — The two inputs system is flat [30], i.e. its trajectories can be summarized by those of two flat outputs x and y .

$$(10) \quad \begin{cases} \dot{x} = \frac{(v_1 + v_2)}{2} \cos \theta, & \dot{y} = \frac{(v_1 + v_2)}{2} \sin \theta, \\ \dot{\theta} = \frac{(v_2 - v_1)}{2l} \end{cases}$$

Considering x and y , one can recover the other variables, i.e. the remaining state θ and the two controls, from x , y and their derivatives.

Explicitly,

$$(11) \quad \theta = \arctan\left(\frac{\dot{y}}{\dot{x}}\right)$$

$$(12) \quad v_1 = \sqrt{\dot{x}^2 + \dot{y}^2} - l \frac{\ddot{y}\dot{x} - \dot{y}\ddot{x}}{\sqrt{\dot{x}^2 + \dot{y}^2}}$$

$$(13) \quad v_2 = \sqrt{\dot{x}^2 + \dot{y}^2} + l \frac{\ddot{y}\dot{x} - \dot{y}\ddot{x}}{\sqrt{\dot{x}^2 + \dot{y}^2}}$$

Thanks to this property, constrained trajectory optimization can be performed using the approach proposed in [73, 59, 68]. The flat outputs histories are then parameterized using B-splines functions, and, in considered cost functionals and constraints variables, are substituted with their expressions (11), (12), and (13). Here, we consider two different constrained minimum time problems.

2.5.1.1. Optimal trajectory along a prescribed path. — The first problem we consider corresponds to the case of a well described path (e.g. a road) the vehicle has to follow as fast as possible, under its dynamic constraints. Given a path $s \in [0, 1] \mapsto (x^{\text{ref}}(s), y^{\text{ref}}(s)) \in \mathbb{R}^2$, it is desired to determine T and $[0, T] \ni t \mapsto \sigma(t) \in [0, 1]$ solution of the following optimal control problem

$$\min_{\sigma, T} T$$

subject to the following constraints (where ϵ is a strictly positive constant)

$$(14) \quad \begin{cases} T > 0, & \sigma \in \mathcal{C}^2[0, T], & \sigma(0) = 0, & \sigma(T) = 1, \\ \forall t \in [0, T], & \dot{\sigma}(t) > 0, \\ |v_i(t)| \leq v_{\max} & i \in \{1, 2\}, \\ |\dot{v}_i(t)| \leq A_{\max} & i \in \{1, 2\} \end{cases}$$

The last inequality can be omitted because (v_1, v_2) does not need to be differentiable (it is convenient to include this last constraint to obtain smooth control histories). If obstacles locations are known, they can be included as state constraints.

2.5.1.2. Free trajectory planning. — In a second setup, we optimize over the possible trajectories originating in a given point A , reaching a desired

target point B , and avoiding known obstacles. It is desired to find the solution of the following optimal control problem

$$\min_{x,y,T} T$$

subject to the constraints (where ϵ is a strictly positive constant)

$$\left\{ \begin{array}{l} T > 0, \quad (x, y) \in (\mathcal{C}^2[0, T])^2, \\ (x(0), y(0))^T = A, \quad (x(T), y(T))^T = B, \\ \forall t \in [0, T], (x(\sigma(t)), y(\sigma(t))) \notin \text{obstacles}, \\ |v_i(t)| \leq v_{\max} \quad i \in \{1, 2\}, \\ |\dot{v}_i(t)| \leq A_{\max} \quad i \in \{1, 2\}, \\ \dot{x}^2 + \dot{y}^2 \geq \epsilon \end{array} \right.$$

The last constraint is added to avoid the singularity of our dynamic feedback controller around zero velocity.

2.5.1.3. Numerical treatment. — Those two problems can be rewritten using only the parameter T and the flat outputs x and y or σ (in the first problem) by substituting v_1 and v_2 in the constraints by their expressions in terms of first and second derivatives of the flat outputs (12) and (13). In the case of constraints given by (14), v_1 and v_2 are computed through the time derivatives of $t \mapsto x^{ref}(\sigma(t))$ and $t \mapsto y^{ref}(\sigma(t))$. Then, the variables are represented by basis functions (typically B-splines). The induced nonlinear program (NLP) can be solved using standard packages (e.g. NPSOL or SNOPT). Compared to a standard collocation approach, in which every state and control variables is represented by distinct basis functions, the proposed substitution technique yields a reduction in the number of variables. This positively impacts the computational burden of solving a NLP (as noted in [60, 10]). Typically, using B-Splines and the Matlab Optimization toolbox, either problem can be solved with a reasonable accuracy in less than 5 sec on a 1 GHz PC (this time increases for complex trajectories where the number of B-splines coefficients can get large). Interestingly, this remark stresses the possibility of real-time trajectory updates as proposed in [68] (for receding horizon control techniques or on-demand mission reconfiguration). Finally, once the optimal

transient time T and flat outputs histories (x, y) are found, the open-loop control values are recovered from (12) and (13).

2.6. Dynamic feedback control law and indoor results

2.6.1. Tracking. — Although the unicycle model is experimentally quite accurate, as noted in Section 2.3, there is definitely a need for closed-loop control in our experimental setup. The main unmodelled disturbance is slipping (especially during outdoor maneuvers). The previous open-loop strategy can be complemented by the following closed-loop dynamic controller. Considering second derivatives of the flat outputs we get

$$\ddot{x} = \dot{u}_1 \cos \theta - u_1 u_2 \sin \theta, \quad \ddot{y} = \dot{u}_1 \sin \theta + u_1 u_2 \cos \theta$$

where we note $u_1 = \frac{v_1+v_2}{2}$ and $u_2 = \frac{v_1-v_2}{2l}$. There is a globally well-defined change of coordinates between the vector $(\ddot{x}, \ddot{y})^T$ and $(\dot{u}_1, u_1 u_2)^T$, through the θ angle rotation matrix. Imposing stable dynamics of the form

$$(15) \quad \ddot{x} = \ddot{x}^{\text{sp}} - k_1(x - x^{\text{sp}}) - k_2(\dot{x} - \dot{x}^{\text{sp}})$$

$$(16) \quad \ddot{y} = \ddot{y}^{\text{sp}} - k_1(y - y^{\text{sp}}) - k_2(\dot{y} - \dot{y}^{\text{sp}})$$

can be achieved through the following dynamic feedback

$$\dot{u}_1 = \cos \theta \ddot{x} + \sin \theta \ddot{y}, \quad u_2 = \frac{1}{u_1}(-\sin \theta \ddot{x} + \cos \theta \ddot{y})$$

where \ddot{x} and \ddot{y} are substituted with the following expressions derived from (15) and (16)

$$\ddot{x} = \ddot{x}^{\text{sp}} - k_1(x - x^{\text{sp}}) - k_2(u_1 \cos \theta - \dot{x}^{\text{sp}})$$

$$\ddot{y} = \ddot{y}^{\text{sp}} - k_1(y - y^{\text{sp}}) - k_2(u_1 \sin \theta - \dot{y}^{\text{sp}})$$

This dynamic feedback controller has a single singularity at $u_1 = 0$. This singularity is avoided, in the open-loop design, by the constraints specified in the optimal control problem.

2.6.2. Indoor results. — A complex manoeuvre can be accomplished indoor. In Figure 2.7, the vehicle has to avoid three obstacles, make a turn and eventually reach a prescribed target. Indoor, only odometers and the gyroscope can be used on-board to determine the position of the vehicle. As can be seen in Figure 2.7, the open-loop behavior shows a

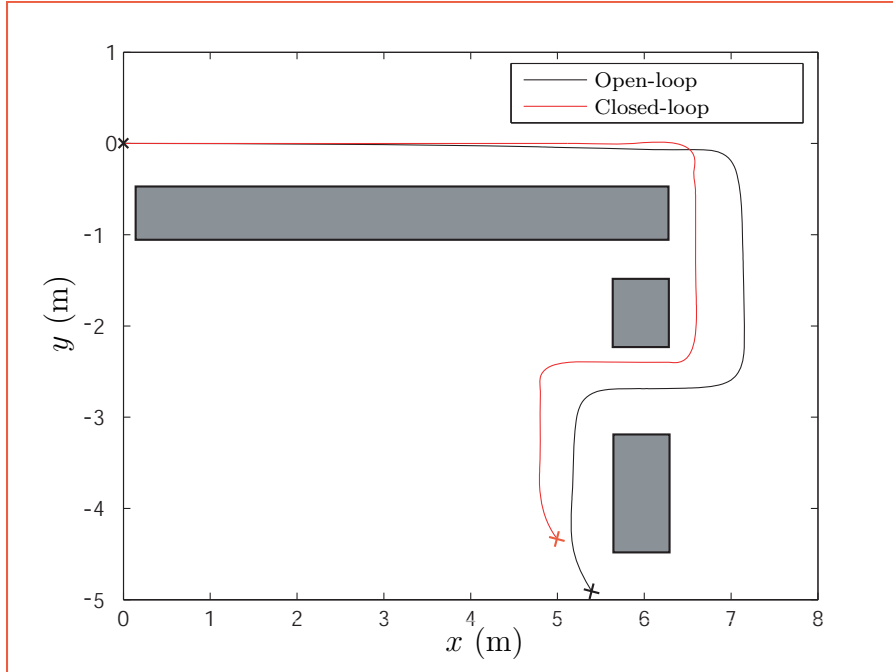


FIGURE 2.7. Indoor closed-loop tracking of an optimal trajectory. One can observe the open-loop drift of the vehicle.

significant drift, probably due to inaccuracies in the slipping laws during sharp turns (and also to unmodeled dynamics such as wheels inertia, and electric drive current saturations). It is overcome by the closed-loop feedback presented in Section 2.6.1. However, one should notice that the measurements do not guarantee that the actual position of the vehicle matches the reference trajectory. In fact, the odometers often provide misleading information, especially during large maneuvers. For long term outdoor experiments, they need to be complemented by absolute measurements such as those from a GPS. This issue is addressed in the following Section.

2.7. Trajectory and state reconstruction, outdoor results

2.7.1. Observer design and implementation. — In order to test the proposed methodology outdoor, the Pioneer vehicle was equipped

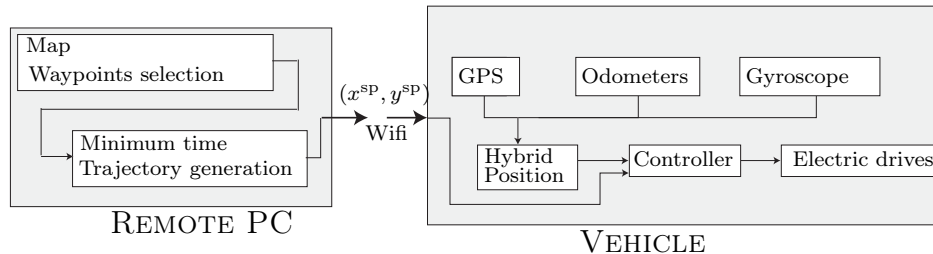


FIGURE 2.8. Human machine interface. Trajectory is designed on a remote PC according to user’s requests (waypoints selected on a map) and minimum time transients control objectives. On-board the vehicle, GPS sensors and odometers feed a hybrid positioning system used in closed-loop to actuate the electric drives.

with an onboard GPS (a uBloxTM TIM-LR). Its signals were fed into an observer along with signals from the odometers and the gyroscope to reconstruct the vehicle position. A Matlab-based human machine interface was designed following the structure presented in Figure 2.8. On a remote PC, several way-points are chosen on a map. Automatically, a smoothing procedure defines a reference path that is fed into the optimal trajectory generation software implemented in Matlab. Once the optimal trajectory is found, it is sent to the remote vehicle through the Wifi datalink under the form of a collection of sampled data. Then, the vehicle starts tracking this trajectory.

2.7.2. Outdoor results. — Typically obtained results are depicted in Figure 2.9 and in Figure 2.10. In these figures, several plots indicate the quality of tracking. Noticeably, neither the GPS nor the odometer can be used as sole positioning system for sake of closed-loop control. The GPS suffers from low pass drift, noises, and jumps, while the odometer signal is altered by a long term drift. Both provide misleading information in a closed-loop context. Yet, it is possible to reconcile the data as we did and obtain an estimate that is suitable for tracking the reference trajectory. These observations clearly appear when inspecting results presented in both Figure 2.9 and 2.10.

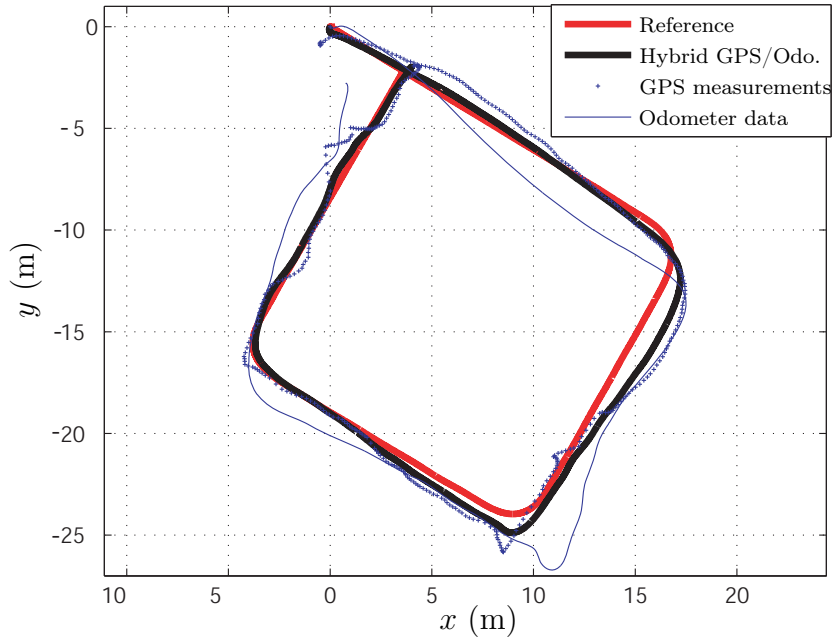


FIGURE 2.9. Spinning around a tree. Y axis is pointing North. X axis is pointing East.

2.8. Future directions

In conclusion, we would like to stress once again the importance of combining the two presented control strategies *in practical experiments*. We believe that with short-range detection devices, the modified gyroscopic-force approach will adequately complement the trajectory optimization strategy. The mathematical study of this combination (in terms of performance and convergence analysis) and the actual implementation of it are interesting subjects for possible future work.

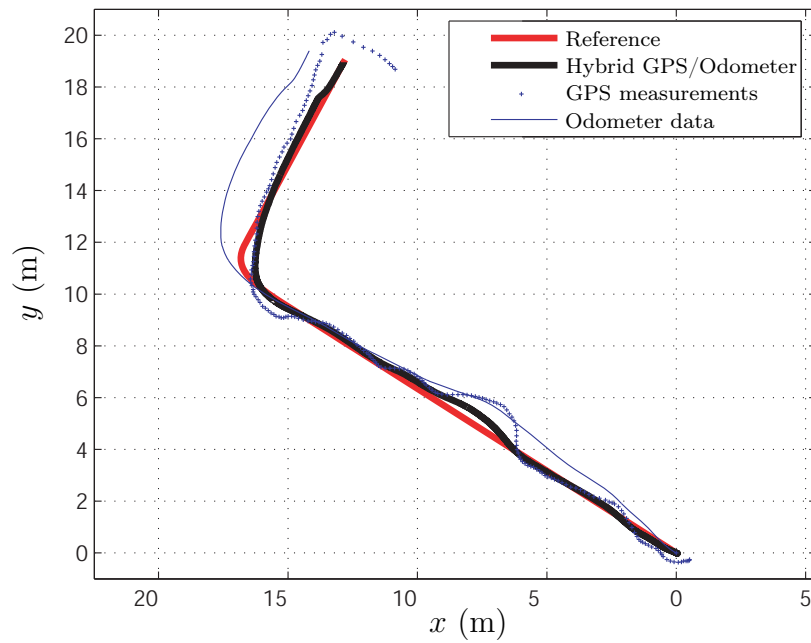


FIGURE 2.10. Turning around a corner. Y axis is pointing North. X axis is pointing East.

PART II

NAVIGATION AND CONTROL SOLUTIONS FOR AN EXPERIMENTAL VTOL UAV

CHAPTER 3

AN EMBEDDED REAL-TIME NAVIGATION SYSTEM

Dans ce chapitre, nous détaillons l'architecture du système embarqué temps-réel que nous avons conçu et mis au point pour assurer la navigation et le pilotage embarqué d'engins autonomes, en particulier des hélicoptères comme celui traité au chapitre suivant. Les performances de ce système et sa modularité sont des points essentiels en vue de l'application expérimentale sur l'hélicoptère sujet du Chapitre 4.

3.1. Introduction

In this chapter, we present a versatile, real-time embedded system, which can easily be used as a real-time guidance and navigation system on various platforms. As will be apparent in Chapter 5, our work in the field of unmanned air vehicles (UAVs) has focused on small-scale (typically less than 2 m wide) vertical take-off and landing (VTOL) aerial vehicles (as described in [16]).

Compared with fixed-wing aircraft and with ground vehicles with tank-like dynamics (as described in [66] and in Chapter 2), these aerial vehicles represent more challenging applications in terms of navigation and guidance. The main reason for this is that these vehicles cannot easily go into any safe mode, unlike ground vehicles, which are, in comparison,

slower and simpler. While it has been proven that, with lowered performance expectations, it is possible to stabilize a fixed-wing UAV by directly closing the loop with signals from well-chosen sensors (e.g., the authors of [50] proposed a solution to the problem of automatically controlling a fixed-wing UAV using only a single-antenna GPS receiver), it is considered by the vast majority of the UAV community that navigation systems require data fusion [23]. In fact, each sensor technology has its own flaws (among which are drift, noise, and possibly low resolution or a low update frequency). However, increases in accuracy by large factors can be gained by reconciling the data from various sensor technologies.

Example of onboard data fusion applications are ubiquitous among autonomous-vehicle-control experiments. Reconciling GPS and inertial-measurement-unit (IMU) measurements provides a classic case study. In [91], results of data fusion from a BeeLine GPS receiver from NovatelTM and a miniaturized IMU were presented. In [25], the development of high-speed data fusion systems in response to the DARPA Grand Challenge was described. In that publication, several technological breakthroughs achieved using a high-end, powerful computer architecture are presented. The software components communicate in a machine-independent fashion through a module management system.

Our experiments could not use such a high-end setup, because the typical payload of our aerial vehicle did not exceed 5 kg. Much smaller, lower-weight systems can be considered, though. In [43], an embedded system was proposed which did not incorporate any powerful calculation board. Instead, a simple Rabbit Semiconductor RCM-3400TM microcontroller was used to perform complementary-filtering data fusion using limited computational power. In the same spirit, in [42], a low-cost test bed for UAVs was presented. It has been reported that the main advantage of designing such an autopilot from scratch is that, in contrast to commercially available products [24, 58], such a system provides full access to the internal control structures. We totally agree with this point of view.

In this chapter, we present a solution that lies midway between the two categories mentioned above. Our system uses two processors. One processor is used to gather data from the sensors and to control the

actuators, and the other processor is used to perform the data fusion calculations (and possibly the control algorithms). The advantages of this structure are as follows: (i) task scheduling is easily programmed, because only one of the two processors is in charge of handling the numerous devices and the I/O; (ii) the computations are performed as one single thread on a dedicated board (of PC type); (iii) depending on the computational requirements, the computation board can be easily upgraded without requiring any software changes or raising any concern about task scheduling; and (iv) finally, the overall system is quite low-cost, since it relies on off-the-shelf components and can be easily maintained.

The chapter is organized as follows. In Section 3.2, we present the architecture of our system. The sensor protocols and the main specifications are briefly described in Section 3.3. We detail our computational hardware and our acquisition boards and comment on the choices made here in Sections 3.4 and 3.5. In Section 3.6, we present the specifications of successive versions of our embedded system. Numerous details of implementation are provided throughout the chapter.

3.2. Requirements

Our primary goal was to develop an embedded system to test algorithms of various complexity on-board various small-scale platforms. Early in the design process, one first constraint which appeared to us was the payload limitations of the considered flying machines. This led us to focus on designing a low-weight embedded system.

A second issue that was also raised early in the design stage was that the real-time requirements of a control system for such small UAVs are very strong. This is mostly due to the short time horizons instabilities. Yet, in the context of embedded systems, real-time scheduling of a number of sensing and computation tasks is known to be a difficult problem. More precisely, as exposed in [14], the problem of determining the feasibility of a periodic sequence of prioritized tasks is often (NP)-hard. Sufficient, but not necessary tests are pessimistic. Popular strategies such as the Rate-Monotonic policy (see again [14]), which consists of putting the highest priority on the shortest task can be proven to be



FIGURE 3.1. Cooperative autonomous vehicles in a future battlefield.

infeasible is the CPU load is too large⁽¹⁾. While being troublesome on ground vehicles, such infeasibilities (and the induced inconsistencies in the embedded calculations) would represent a cause of potential major failure for our aerial platforms.

Keeping these two considerations in mind, we decided to develop a robust two-processors embedded system, running two distinct softwares and communicating through a simple two-ways protocol. The system specifications are as follows.

1. It performs the sensing and calculation tasks separately.
2. It is fast enough to run a typical 15 to 30 dimensional states EKF algorithm with a low latency (to eventually produce satisfactory closed-loop results).
3. It is easy to upgrade.

⁽¹⁾the upper limit on admissible load is 69%, approximately.

4. It is versatile enough to handle various type of sensors and communication protocols.

As exposed in Figure 3.2 and Figure 3.3, this (modular) embedded system is composed of a micro-controller, which is in charge of gathering information from all the sensors, and a calculation board. These two elements are connected by a serial interface. The micro-controller also has a downlink to a ground station. We now present the details of the hardware components of our system.

3.3. Sensors performances and protocols

3.3.1. Sensors. — Considering both ground and aerial vehicles control applications, we listed a series of useful sensors that needed to be incorporated into our embedded system. Among these are: an IMU, a GPS receiver, a pressure sensor, an anemometer, magnetometers, and various switches (to detect take-off and landing instants). Other possibilities include odometers, LADARs (as used in [25]), and sonars (as used in [83]), or cameras (as used in [39]). In the context of our study, we only considered low-cost sensors. We now detail these. In each case, we specify the weight (in g), the cost (in USD), the dimensions (in mm), the update rate (f in Hz), and the protocol of communication (Comm.).

- **Inertial Measurement Unit (IMU):** Our IMU is a 3DM-GX1 from MicrostrainTM. It contains three angular rate gyroscopes, three orthogonal single-axis magnetometers, and three single-axis accelerometers, along with 16 bits A/D converters and a micro-controller. This IMU can deliver different messages, ranging from raw-data, to reconciliated measurements. In our setup, we ask the IMU to deliver only calibrated sensors data at a 75 Hz rate.

Weight	Cost	Size	f	Comm.
30	1450	39,54,18	75	RS232

- **Global Positioning System (GPS):** Our GPS is a TIM-LS from μ bloxTM. Through a proprietary binary protocol, it provides position and velocity information at a 4 Hz rate. Position error is 2.5 m (Circular Error Probability CEP) and velocity error is 2 m

CEP. The GPS receiver is not very tolerant against power supply voltage ripples. These can be kept below the 50 mV requirements thanks to a dedicated power supply regulator from TRACO™.

Weight	Cost	Size	f	Comm.
23	100	32,47,9.5	4	RS232

- **Barometer:** Our barometer is the MS-5534 from Intersema™. Using a SPI-type protocol, it gives calibrated digital pressure and temperature information. This device requires a 3 V power supply which is obtained through a fast response diode from the main 5 V power supply of the micro-controller.

Weight	Cost	Size	f	Comm.
2	14	5,4,2	20	SPI

- **Anemometer :** A PXL A sensor from ASensTec™ delivers a differential pressure analog signal, which can be read through a 10 bit A/D converter.

Weight	Cost	Size	f	Comm.
10	25	11,8,12	75	Analog

- **Magnetometer :** We use a HMR2300 three axis magnetometer from Honeywell™. Its range is ± 2 gauss and it has a 70 μ gauss resolution.

Weight	Cost	Size	f	Comm.
28	230	75,30,20	154	RS232

- **On off Switches, take off and landing detector:** Being able to detect take-off and landing instants is necessary to properly initialize data fusion algorithms. In details, detection of the corresponding switches in the dynamics defines when the controls actually have an effect on the system. This is not the case when an UAV is on the ground. This detection is performed with on-off switches which can be located, e.g., on the landing gear. They deliver a logic signal which can be readily interpreted. To prevent electric arcs which

might cause trouble to the connected micro-controller, we added a specific interfacing circuit. This switches can also be replaced by active switches which can be used to activate various devices such as digital cameras, or parachutes.

Weight	Cost	Size	f	Comm.
10	6	25,10,5	75	Boolean

- **Data Link:** Our data link is a MaxStream™ module operating at 2.4 GHz. It provides a RS232 serial data link at 9600 baud sending the information from the embedded system to the ground station.

Weight	Cost	Size	f	Comm.
250	230	40,68,9	30	RS232

Our system is data-driven by the IMU. The main reason behind this choice is that the IMU is considered as a critical sensor.

3.4. MPC555 micro-controller : sensors and actuators interface

The micro-controller which is used as an interface for the sensors and actuators is a MPC555 Power PC from Motorola™. It runs a specific software we developed using the Phytex™ development kit. The reason for choosing this micro-controller are as follows. This device provides a double precision floating-point unit (64 bit) which is convenient for potential embedded algorithms (even if we do not use this possibility here since all computations are performed on the calculation board), it has a relatively fast 40 MHz clock, it has 32 bit architecture and 448Kbyte of Flash memory and 4 MBytes of RAM. Most importantly, among the family of 32 bits kits, the MPC555 has substantial computational capabilities and a large number of versatile and programmable Input/Output ports. In particular, we make an extensive use of its TPUs (Time Process Units), UARTs, A/D converters, SPIs, MPIOs (Modular I/O system) (see [67]). Finally, it is small (credit card format) and has a low weight.

Weight	Cost	Size	f	Comm.
25	450	72,57,8	all	all

No operating system is used on the micro-controller. Rather, the MPC 555 runs a specific interrupts-driven software written in C. Information from each sensors is transferred using a dedicated interrupt handler routine. Each external source or group of sources has its own interrupt level which avoids potential conflicts. Each data link is associated with a checksum to validate reception.

The data acquisition software running on the micro-controller is event-driven by the IMU messages which periodically sends 31 bytes of data. Once the message of the IMU is received and validated by the micro-controller, others sensors information are either directly read or picked in data buffers which are constantly fed with serial messages from the sensors through hardware interrupts. Information is gathered in a 116 bytes message containing all the onboard measurements. This message is sent to the calculation board through a high-speed serial port. Once the message is received and validated, the calculation board carries out one navigation loop consisting of a prediction equation and an estimation equation of a discrete extended Kalman filter.

3.5. Embedded PC : computation board

The computing board is a PC running the Knoppix 3.8.1 Linux distribution. The PC board was selected among numerous models (mostly mini-ITX, and PC104) based on computational power, energy consumption, toughness, and price. A fan-less board was considered as the most relevant choice, due to the often observed failures of fans in mechanically disturbed environments.

The chosen fan-less calculation board has a standard mini-ITX PC architecture. Its processor is a 1.2 GHz C7-M from VIATM designed for embedded applications. It can perform 1500 MIPS and has classic PC Input/Output ports such as a UART serial port (used as main data link with the micro-controller), an ethernet board (not used here), a VGA screen output (which can be used to monitor the system during debugging phases of the software and hardware development), a keyboard, and 4 USB ports (which can be considered for plugging future devices such as controllable cameras).

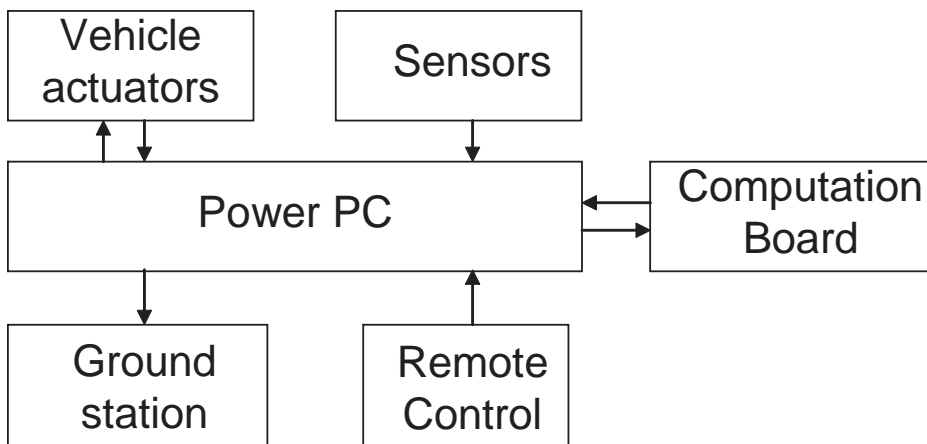


FIGURE 3.2. Sensors and computation board connections to the central micro-controller.

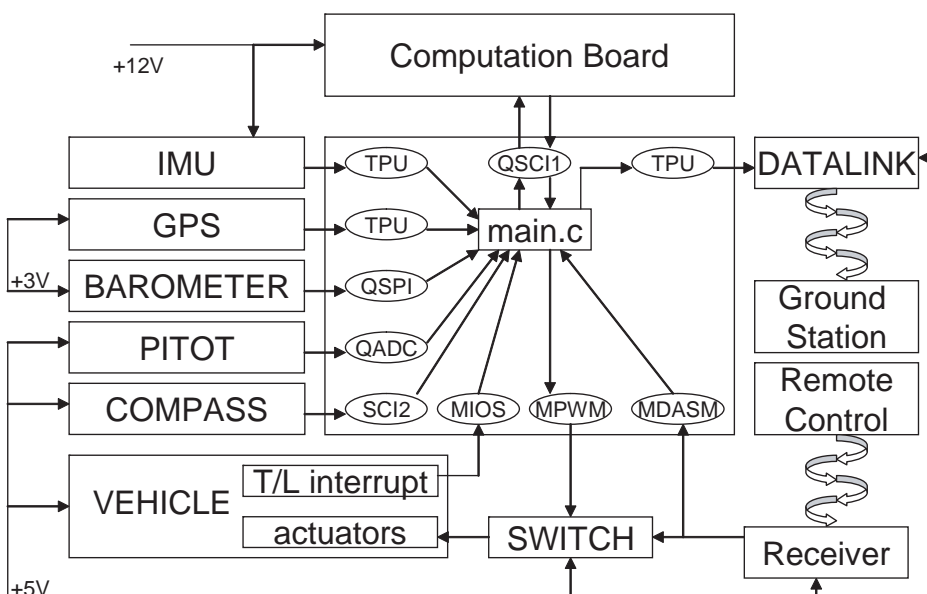


FIGURE 3.3. Embedded system internal connections.

Experimental preliminary tests have shown us that multi-threading (one thread for message decoding and one thread for the main algorithm) presents two major drawbacks: some data can be lost, and the calculation cycle may end unexpectedly (slightly) late. For this reason, we decided

to write our own UART driver using an interrupt handler in the kernel space. Further, we de-activated all hardware interruptions associated to unnecessary devices. As a result, only interrupts from the UART are enabled. Finally, we used a single computation thread.

The operating system is installed on a bootable 1 Gbyte Disk-On-Chip system which prevents all possible mechanical failure associated to hard-drives. This flash memory device is directly connected to the IDE port of the mother-board. The board is powered by a pico-PSUTM power supply which provides various voltages ranging from 5V to 18V. The computation software are written in C and can be either be updated directly on the board via a `ssh` connection, or transferred, in a compiled form, from a remote PC. Custom scripts for compiling and distributing our executable code and configuration files are an efficient way to upgrade the software during development and testing.

Weight	Cost	Size	f	Comm.
800	350	170,180,40	1.5e6	RS232

3.6. Successive iterations and issues raised

Over the last three years, we have designed three complete versions of our embedded system. In 2005, we decided that it was more convenient to gather the main processor, all the sensors, and the necessary power supplies together on a single (wooden) board. Numerous long connecting cables were necessary. This first board, pictured in Figure 3.4, was designed to simplify the laboratory experiments. It was not meant to be embedded on board the helicopter. Occasionally, it could be mounted on the Pioneer vehicle described in Chapter 2. This was a first step toward reducing the time needed to perform identification experiments and writing easily testable real-time software. It also improved the reliability of the whole system.

During application of the system, it soon became apparent that it was necessary to reduce the size of this large board (especially in order to embed it into the helicopter). Several improvements led to the second version, pictured in Figure 3.5. Still, the inconvenient Phytex development kit had to be used. The reason for this was that, at that time, wiring

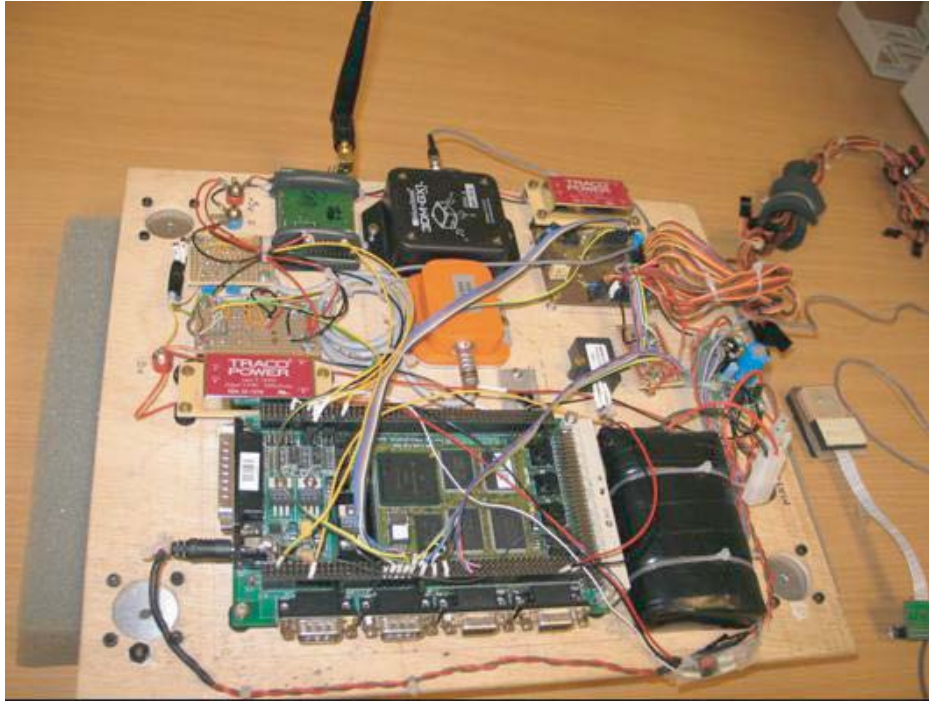


FIGURE 3.4. The first embedded system we developed in 2005.

the MolexTM connectors of the MPC555 was a serious issue. Among the very important problems to be solved was the choice of efficient shock absorbers. Several suspension designs were considered, built, and tested. Eventually, the structure represented in Figure 3.5 was chosen, and has remained unchanged up to now.

Finally, in 2007, we decided to connect the MPC555 microcontroller to a computational board. Getting rid of the heavy and inconvenient development kit left us with some room and payload capacity. We connected the fanless PC board discussed in Section 3.5 and installed it beside the smaller-sized wooden box where the rest of our system fitted. The connecting cables were reduced in size and the weight was optimized. The batteries are now located in a very convenient zone. Smaller connectors replace the former large ones.



FIGURE 3.5. The second version of the embedded system we developed in 2006.

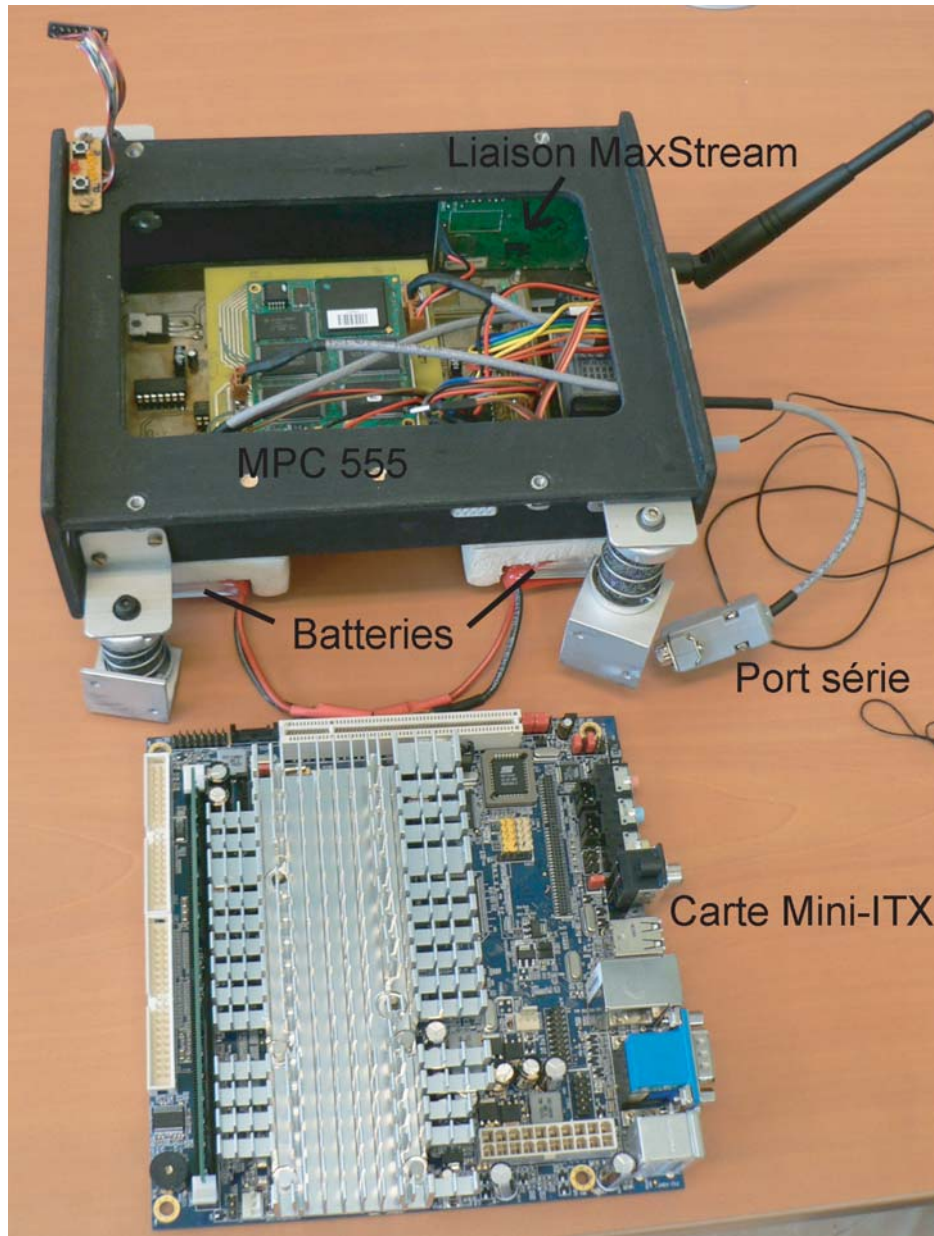


FIGURE 3.6. The latest version of the embedded system developed in mid-2007.

CHAPTER 4

AUTONOMOUS FLIGHT OF A SMALL-SCALE HELICOPTER USING A MODEL-BASED OBSERVER

Dans ce chapitre, nous détaillons notre travail de conception d'un drone à voilure tournante sur base d'hélicoptère de modélisme. Il s'agit d'un engin de 1.8 m de rotor que nous avons équipé d'un système de navigation du type exposé au Chapitre 3. Pour compenser les défauts des capteurs de ce système bas-coût (moins de 3000 dollars de capteurs et de calculateurs), nous utilisons un modèle de connaissance de la dynamique du vol d'un tel hélicoptère.

In this chapter, we address the problem of the guidance and control of a small-scale helicopter (Benzin Acrobatic from VarioTM, with a 1.8 m diameter rotor) equipped with the low-cost embedded system presented in Chapter 3. This system used various sensors, namely an IMU, a GPS receiver, and a barometer, which represented a total cost of USD 3000 (including one PC board and one microcontroller). In contrast to other experiments reported in the literature, we did not rely on accurate IMU or GPS systems, the costs of which alone would be very much above the

mentioned amount of USD 3000. To compensate for the weaknesses of this low-cost equipment, we put our efforts into obtaining an accurate flight dynamics model. This improved the prediction capabilities of our embedded Kalman filter, which served for data fusion. The main contribution of this chapter here is a detailed description, in the light of a successful reported autonomous hovering flight, of the derivation of the model. We give numerous details of the implementation and discuss the relevance of some modeling hypotheses based on our experience.

4.1. Introduction

The ever-increasing performance of IMUs based on microelectromechanical systems (MEMS), and the availability of low-cost GPS receivers have given these devices the roles of enabling technologies for new autonomous vehicle applications. Yet the challenges are numerous. In particular, downscaling of helicopters appears to be very difficult. In this field, several teams have given answers to certain technological questions related to autonomous flight. Among these are the outstanding experiments conducted by [54, 57, 56, 55, 1, 69]. An R-max helicopter (with a 3.5 m rotor) from Yamaha was used at Carnegie Mellon University [54] and at ONERA [27, 26]. An X-cell helicopter was used at Massachusetts Institute of Technology (this model had a 1.7 m rotor) by [34].

While accurate dynamical models for such helicopters have been known since the work of [56] and [32] (see also [45, 8] and references therein), a classical filtering methodology was used in all these reported experiments. In detail, a very general rigid-body model with six degrees of freedom (DOF) was considered and was reported to be sufficient in coordination with good-quality sensors. The reason for this is that the sensors considered in these studies provided accurate enough information for navigation and control. An accurate model was used only for control purposes, which included design, tuning, and simulation.

Here, we focus on really low-cost sensors. These sensors belong to the same technology group as those found in the successful experiments discussed above, but they are really in the low-end category. It is believed that cost reduction will yield a substantial speed-up in the spread of

UAVs among both the military and the civilian communities. As can be seen from various reported experiments, sensors represent an important part of the total cost of small-sized UAVs. This raises some feasibility questions. What are the minimum quality requirements that one must impose on sensors to obtain a navigation system capable of providing real-time information sufficient to feed a stabilizing feedback controller? What categories of sensors can be used for each type of UAV? Which sensor is critical?

We believe that the answer is not contained solely in the specifications of the sensors. We wish to demonstrate that much improvement can be obtained from considering the model of the UAV. Rather than considering data fusion algorithms based on a 6-DOF representation of the vehicle under consideration, we think that much attention should be paid to incorporating an accurate flight dynamics model into the data fusion algorithm.

Consider the particular case of small-scale helicopters. It is certainly not possible to include all of the equations found in the literature on helicopters. A complexity–accuracy trade-off must be made. Also, identification of the parameters appearing in the equations can be difficult. In the light of these points, we can reformulate some of the above questions. What gain can be expected from including a dynamical model of the system in the data fusion algorithm? Which physical phenomena need to be taken into account, and which ones can be neglected? These questions (among others in the same spirit) have been partially experimentally answered in the case of fixed-wing aircraft. We will address them for small-scale helicopters.

This chapter is organized as follows. In Section 4.2, we present our experimental small-scale helicopter. We give details of the helicopter, and briefly describe the sensors under consideration and their accuracy. In Section 4.3, we stress some experimental constraints that we encountered using this experimental test bed. In Sections 4.4, 4.5, and 4.6, we set out a model for the helicopter. We stress some weaknesses of this approach. In Section 4.7, we propose improvements to the modeling and incorporate them into a data fusion algorithm (a Kalman filter). Coupling and ground effects are studied. In Section 4.8, by successively turning off each sensor,



FIGURE 4.1. “Goliath”, our helicopter equipped with low-cost sensors in hover flight.

we test the robustness of the data fusion algorithm and determine the beneficial effect of including the model in the prediction phases of the Kalman filter. In Section 4.9, we give details of the control feedback law and give closed-loop results obtained during autonomous hovering, before we conclude with Section 4.10.

4.2. Experimental small-scale helicopter

The embedded system, presented in Chapter 3, is used onboard the helicopter.

4.2.1. Aerial vehicle. — The aerial vehicle we use is a Vario Benzin Acrobatic helicopter. It is powered by a 23 cm³ Zenoah engine connected through a reductor to the 1.8 m diameter main rotor. Its nominal weight is 6.5 kg. High-end C4421 Graupner servodrives are used as actuators (their torque can reach 8.5 Nm). This improves the system mechanical reliability. The helicopter is pictured in Figures 4.1 and 4.2. The landing gear has been replaced by a specially designed (and machine tooled) one which carries our embedded system. Very importantly, specifically

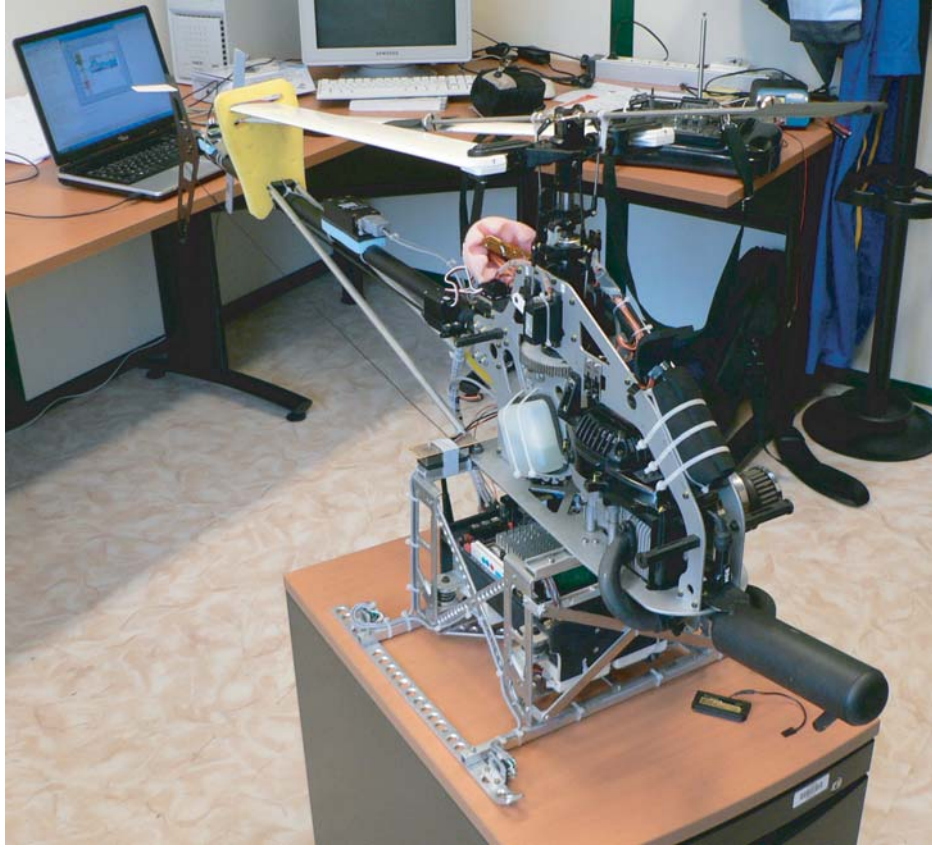


FIGURE 4.2. Helicopter in its unmanned version

tuned dampers are used to cut-off undesired oscillations generated by the main rotor and to prevent them from propagating down to the inertial measurement unit (IMU). The 25 Hz resonant peak generated by the 1700 rpm rotor speed is substantially attenuated. More details are reported in § 4.3.3. Fully equipped with the embedded system, a large amount of fuel and extra batteries, the helicopter weight 10.1 kg.

A human pilot can control the helicopter using servodrives remotely actuated through the RC system (see Figure 4.3). These act upon the main rotor, the tail rotor and the main engine. Servodrives 1, 2, 3 and 5 are used to control the cyclic pitch angle of the main rotor: servodrives 1 and 2 symmetrically play on the swashplate lateral axis, while servos 3 and 5 generate a longitudinal motion of the swashplate. An equally

valued control action on these four servo has a zero total contribution to the collective swashplate angles. Servo 6 controls the engine throttle, which directly impact on the generated torque, while servo 4 (which is usually gyro-stabilized by a low-level controller included with the hobby tail gyro, see § 4.3.3) controls the tail rotor pitch angle.

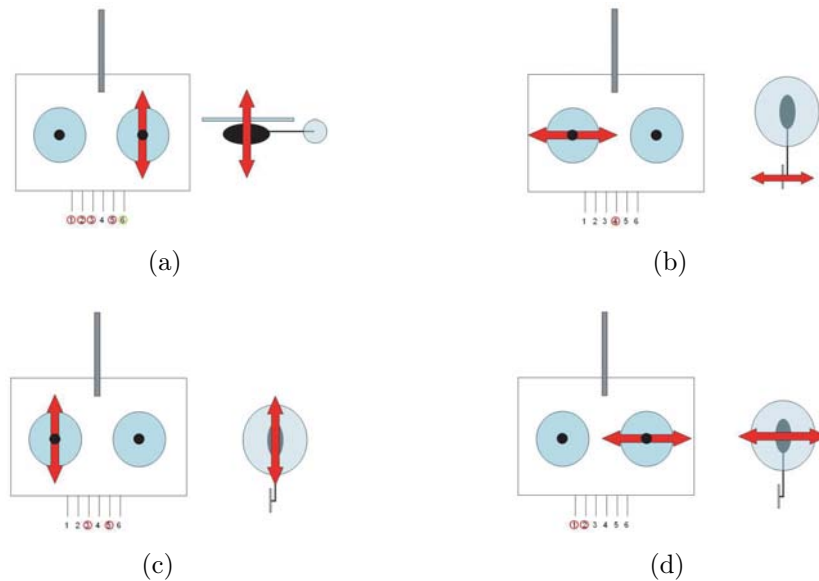


FIGURE 4.3. (a): Collective pitch orders are used to control vertical motions. (b): Yaw orders control heading. (c): Longitudinal cyclic pitch orders generate front-rear swinging motions. (d): Lateral cyclic pitch orders generate left-right swinging motions.

The Benzin Acrobatic by VarioTM was chosen because of its reliability (we never encountered any mechanical failure over more than 100 flights), its payload capacity (above 5 kg), and its simplicity of servicing. Approximately 20 cl of petrol provide 20 min of flight.

4.2.2. Onboard sensors. — The sensors are mostly located on a board which is linked to the helicopter frame through the mentioned dampers. The systems magnetometers are, roughly speaking, unusable due to the large amount of non-stationary magnetic disturbances created by the engine (mostly the inertial wheel and the spark ignition



FIGURE 4.4. Three dimensional view of the CATIA® model (©Dassault Systèmes) of our helicopter. 680 different parts are modeled and kinematically linked together. Payload, landing-gear, sensors, electronic devices, Li-Po batteries, and numerous add-ons are modeled to obtain accurate estimates of inertia matrix and position of the center of gravity.

system) which is nearby. Therefore, we installed an additional tri-axis magnetometer (Honeywell™ HMR 2300) on the tail. It is used to derive heading information. The μ blox™ GPS and its antenna are located at the end of the tail (see Figure 4.4). Its update rate is 4 Hz. While its accuracy is 2.5 m CEP (CEP: Circular Error Probability at 50%) for the position and $2 \text{ m}\cdot\text{s}^{-1}$ CEP for the velocity. To compensate the poor altitude accuracy of the GPS receiver, we installed a barometric sensor (Intersema MS5534) inside the “sensor box”. The four on-off switches of our embedded system are fitted on the landing gear to detect take-off and landing.

Take off and Landing detector: Being able to detect take off and landing instants is necessary to properly initialize data fusion algorithms. In details, detection of the corresponding switches in the dynamics defines when the controls actually have an effect on the system. This is



FIGURE 4.5. Sensors in use.

not the case when the helicopter is on the ground. This detection is performed with four on-off switches located at each corner of the landing gear. They deliver a logic signal which can be readily interpreted.

Weight	Cost	Size	f	Comm.
10	6	25,10,5	75	Boolean

4.2.3. Manual switch. — An important safety device is the remotely controlled switch board which can be used, at any time, to disconnect the outputs of our embedded system from the actuators and substitute them with the RC receiver outputs. This independent device, named “manual switch”, does not rely on any information from onboard CPUs. It is electrically controlled by a dedicated channel of the RC receiver.

4.3. Experimental setup, vibrations and electrical issues

We now report some field experiments using our embedded system. Numerous details about solutions to specific interfacing and vibrational issues are given.

4.3.1. Experimental setup. — We conducted all the experiments with the help of a human pilot which could, *at any time* remotely connect the inputs of the actuators of the helicopter to the outputs of our

embedded system or directly to the outputs of the radio receiver (and thus take direct control of the helicopter) through the manual switch board (see§ 4.2.3).

During all flights, the pilot could see images from an on-board camera and read measurements from the embedded system received through the down datalink. A convenient dual-screen Head-Up display system on the ground station was designed for that purpose (see Figure 4.6).

4.3.2. Interfacing and vibrational issues. — Wiring the embedded system to the existing helicopter circuitry was achieved using some specific additional boards and connectors. To measure the pilot’s commands in real-time, we used a 6 channels voltage follower circuit. Numerous LEDs were added to check the status of our system.

As already discussed, a central problem observed on-board helicopters is the 25 Hz vibrations induced by the main rotor blades. These vibrations generate a large amount of noise on the inertial sensors. In practice, these noises totally overwhelm the useful signals. Fortunately, it is possible to solve this issue by using well-chosen vibration dampers. On our helicopter, we decided that the micro-controller and the sensors would all be located on a board which would be physically connected to the frame of the helicopter through four spring-damper systems (see Figure 4.7). Experiments conducted on a vibrating table have shown that it was advantageous to keep the embedded system as compact and as rigid as possible. The total weight of the subsystem is about 600 g. We decided to attach some of the batteries to it to bring the weight close to 1.8 kg. This enabled us to use off-the-shelf dampers yielding appropriate cut-off frequencies. MV801-5CC dampers from PaulstraTM were chosen for their ability to work with low masses vibrating at low frequencies. With these, we obtained a satisfactory vibration damping, with a cut-off frequency around 9 Hz. This is represented in Figure 4.8. Further, resonant frequencies due to the engine frequency (around 160 Hz), the tail rotor frequency (around 115 Hz), and the tail boom were removed using a digital notch filter. The presented solution attenuates high frequency vibration inputs down to negligible levels.



FIGURE 4.6. The latest version of our ground station fits inside a single suitcase loaded with batteries for outdoor experiments.

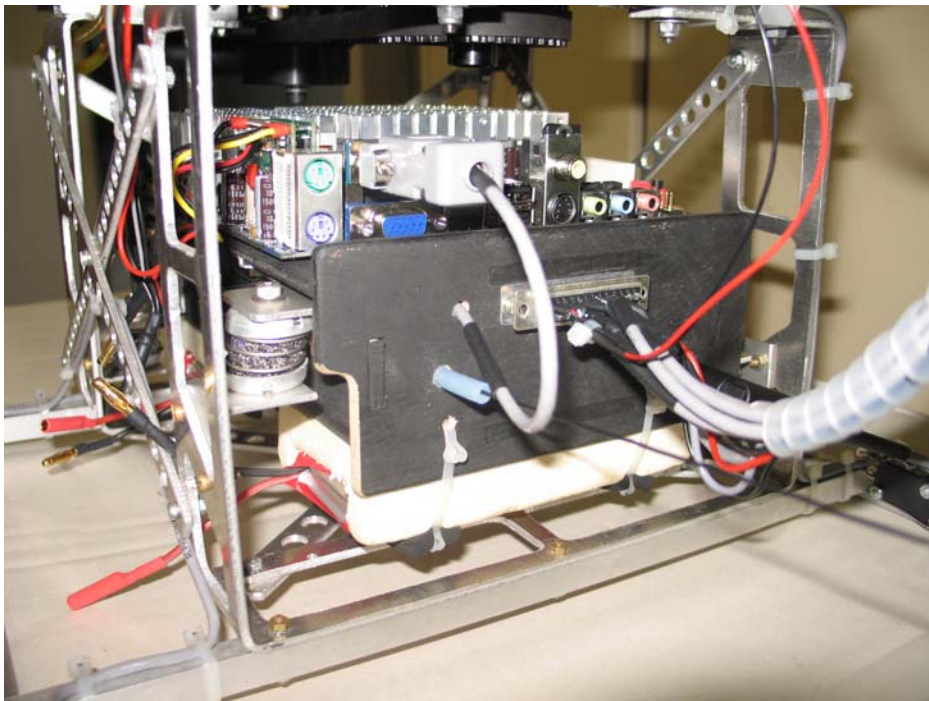


FIGURE 4.7. Our embedded system fitted into the (custom-built) landing gear of a small-scale Vario Benzin helicopter. Springs and dampers are used to filter out vibrations from the main rotor blades.

4.3.3. Preliminary identification. — Preliminary model identification experiments need to be conducted before state estimation can be performed.

In particular, using our embedded system, we studied the actuators transfer functions and the yaw rate gyroscope.

In some works (see [54] or [56]), actuators (servomotors) are considered as first order systems with dead band. We identified such transfer functions for various GraupnerTM and FutabaTM servomotors. Results of various tip-in and tip-out in reference signals were recorded to compute the time constant of the first order model.

On-board our helicopter, a hobby gyroscope from GraupnerTM is used to help the human pilot keeping the yaw rate as small as possible. Pilot commands are transferred from the R/C receiver to the tail actuator

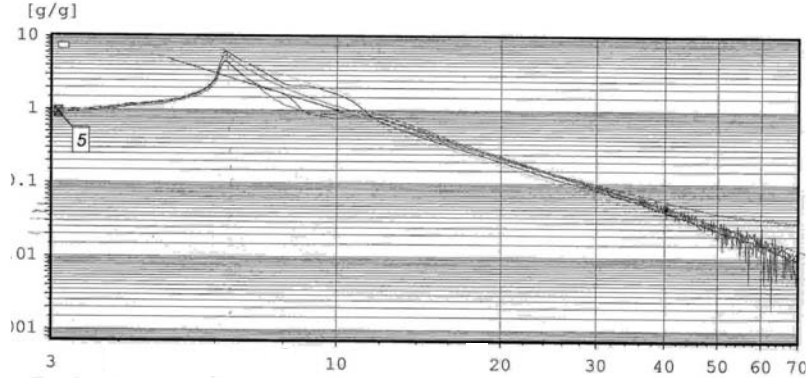


FIGURE 4.8. Bode diagram showing the resonance peak and the cut-off frequency of the mechanical structure equipped with the sensors, the micro-controller, and the spring-dampers suspension. The various plots are obtained on varying locations on the vibrating structure and show a good spatial uniformity of the vibration damping.

through this gyroscope. To validate simple models of this transfer, we located our IMU under this gyroscope to measure the angular velocity. Simultaneously, we connected the gyroscope and recorded the gyroscope signals sent to the tail actuator. Surprisingly, it was discovered that the gyroscope feedback behaves as a 2 Hz low-pass filter on the pilot commands, and directly transmits the opposite of the received angular rate, without filtering it. This can be summarized under the form:

$$\delta_{gyro} = N_r r_m + \frac{\delta_{pilot}}{1 + \tau_{gyro} s}$$

Where δ_{gyro} is the order sent to the tail servo, δ_{pilot} is the pilot command, τ_{gyro} is a response time such that the transfer function corresponds to a 2 Hz low pass filter, r_m is the measured rate of turn, N_r is a linear constant consistent with the actuator and command scale factors.

4.4. Small-scale helicopter: rigid-body model

4.4.1. Frame in use. — A body reference fixed frame with origin at the center of gravity of the helicopter is considered. The x , y and z axis coincide with the helicopter axis. These axis also coincide with the IMU inner sensors axis. In the following, subscript b refers to this body frame. As inertial reference frame, we consider the North-East-Down (NED). The x axis is tangent to the geoid and is pointing to the north, the z axis is pointing to the center of the earth, and the y axis is tangent to the geoid and is pointing to the East. Subscript i refers to this inertial frame.

The origin of the inertial frame is noted O . It is located on the earth surface. The origin of the body frame is G the center of gravity of the helicopter. The axis of the body frame are determined by three successive

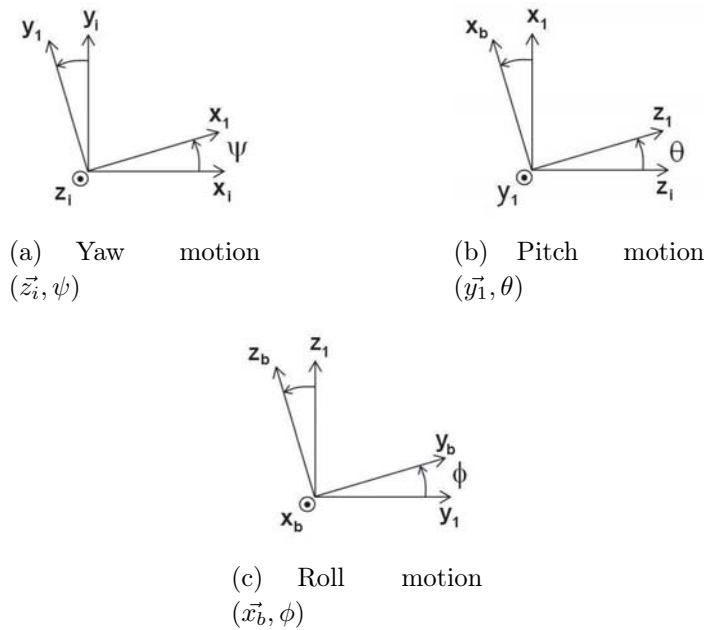


FIGURE 4.9. Cardan angles.

rotations defined by the Cardan angles (see Figure 4.9): the yaw angle ψ which is defined around the vertical axis z_i the pitch angle θ which is

defined about the intermediate axis y_1 , and the roll angle ϕ which is defined around the x_b axis.

Using this frame R_b , we can now define the translation velocity $V = (u, v, w)^T$ and the rate of turn $\Omega = (p, q, r)^T$ corresponding to the positions (x_b, y_b, z_b) and the angles (ψ, θ, ϕ) , respectively. These are the twelve states usually considered to represent a rigid body dynamics with six degrees of freedom.

Unless specially mentioned, vectors are now considered in the body frame. The rotation vector ω is defined from the cardan angles as follows

$$\boldsymbol{\omega} = \begin{bmatrix} p \\ q \\ r \end{bmatrix} = \begin{bmatrix} \dot{\phi} - \dot{\psi} s_{\theta} \\ \dot{\theta} c_{\phi} + \dot{\psi} s_{\phi} c_{\theta} \\ \dot{\psi} c_{\phi} c_{\theta} - \dot{\theta} s_{\phi} \end{bmatrix}$$

where, s_x and c_x stands for $\sin(x)$ and $\cos(x)$ for sake of conciseness. The cardan angles time derivatives can be computed from the time derivatives (p, q, r) . Yet, to avoid the singularities about $\theta = \pm \frac{\pi}{2}$, quaternions are preferred.

Classically, the quaternions q_0, q_1, q_2, q_3 are defined as

$$\begin{cases} q_0 = \cos \frac{\phi}{2} \cos \frac{\theta}{2} \cos \frac{\psi}{2} + \sin \frac{\phi}{2} \sin \frac{\theta}{2} \sin \frac{\psi}{2} \\ q_1 = \sin \frac{\phi}{2} \cos \frac{\theta}{2} \cos \frac{\psi}{2} - \cos \frac{\phi}{2} \sin \frac{\theta}{2} \sin \frac{\psi}{2} \\ q_2 = \cos \frac{\phi}{2} \sin \frac{\theta}{2} \cos \frac{\psi}{2} + \sin \frac{\phi}{2} \cos \frac{\theta}{2} \sin \frac{\psi}{2} \\ q_3 = -\cos \frac{\phi}{2} \cos \frac{\theta}{2} \sin \frac{\psi}{2} + \sin \frac{\phi}{2} \sin \frac{\theta}{2} \cos \frac{\psi}{2} \end{cases}$$

Inversely, one has

$$\begin{cases} \phi = \arctan \left(\frac{2(q_2 q_3 + q_0 q_1)}{q_0^2 - q_1^2 - q_2^2 + q_3^2} \right) \\ \theta = \arcsin (-2(q_1 q_3 - q_0 q_2)) \\ \psi = \arctan \left(\frac{2(q_1 q_2 + q_0 q_3)}{q_0^2 + q_1^2 - q_2^2 - q_3^2} \right) \end{cases}$$

The time derivatives of the quaternions are

$$\begin{bmatrix} \dot{q}_0 \\ \dot{q}_1 \\ \dot{q}_2 \\ \dot{q}_3 \end{bmatrix} = \frac{1}{2} \begin{pmatrix} 0 & -p & -q & -r \\ p & 0 & r & -q \\ q & -r & 0 & p \\ r & q & -p & 0 \end{pmatrix} \begin{bmatrix} q_0 \\ q_1 \\ q_2 \\ q_3 \end{bmatrix}$$

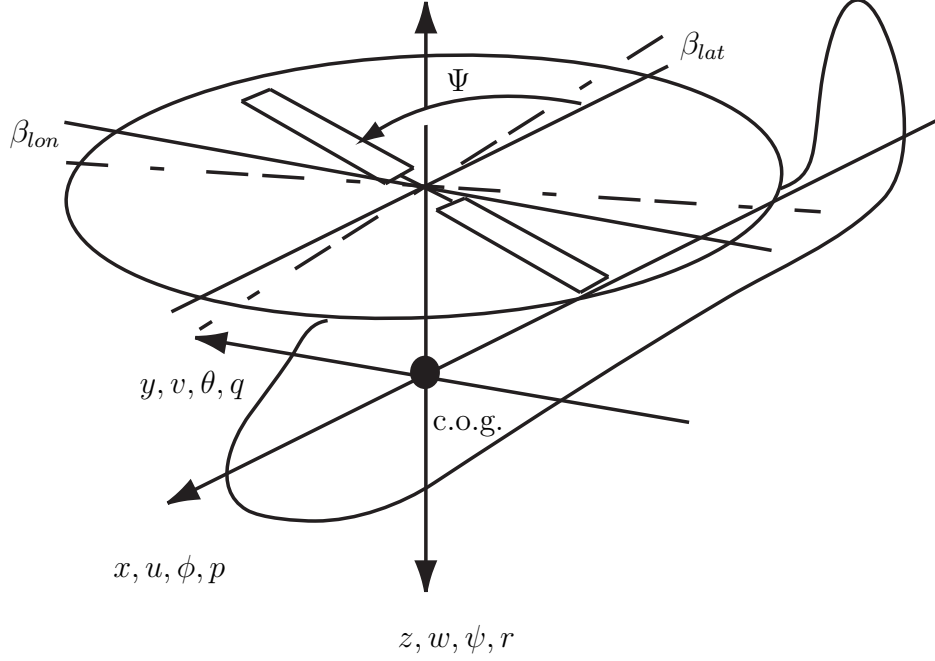


FIGURE 4.10. Notations in the body frame [54].

The linear mapping from the body frame to the inertial frame is

$$\begin{aligned}
 P_{R_b \rightarrow R_i} &= \begin{pmatrix} c_\theta c_\psi & c_\theta s_\psi & -s_\theta \\ s_\phi s_\theta c_\psi - c_\phi s_\psi & s_\phi s_\theta s_\psi + c_\phi c_\psi & s_\phi c_\theta \\ c_\phi s_\theta c_\psi + s_\phi s_\psi & c_\phi s_\theta s_\psi - s_\phi c_\psi & c_\phi c_\theta \end{pmatrix} \\
 &= \begin{pmatrix} q_0^2 + q_1^2 - q_2^2 - q_3^2 & 2(q_1 q_2 + q_0 q_3) & 2(q_1 q_3 - q_0 q_2) \\ 2(q_1 q_2 - q_0 q_3) & q_0^2 + q_2^2 - q_1^2 - q_3^2 & 2(q_2 q_3 + q_0 q_1) \\ 2(q_1 q_3 + q_0 q_2) & 2(q_2 q_3 - q_0 q_1) & q_0^2 + q_3^2 - q_1^2 - q_2^2 \end{pmatrix}
 \end{aligned}$$

In particular, the gravity vector coordinate are

$$(17) \quad \begin{bmatrix} 0 \\ 0 \\ g \end{bmatrix}_{R_i} = \begin{bmatrix} -gs\theta \\ gs\phi c\theta \\ gc\phi c\theta \end{bmatrix}_{R_b}$$

4.4.2. 6 DOF rigid body dynamics. — We consider the helicopter as a six DOF rigid body on which external forces and torques are applied

(these originates from the main rotor and the tail rotor). These forces and torques are depending on the commands and are impacted by the rotation of the rigid body. The translational motions are neglected here. We now derive these equations.

Consider the body frame R_b and apply Newton's law on the helicopter. Its mass is noted m , its tensor of inertia is $\underline{\underline{I}}$, we note F the external forces and M the external torques.

With these notations, the dynamics of the 6 DOF rigid body is

$$\begin{cases} m \frac{dV}{dt} / R_i = F \\ \underline{\underline{I}} \frac{d\Omega}{dt} / R_i = M \end{cases} \quad \begin{cases} m \frac{dV}{dt} / R_b + \Omega \times mV = F \\ \underline{\underline{I}} \frac{d\Omega}{dt} / R_b + \Omega \times \underline{\underline{I}} \Omega = M \end{cases}$$

The external forces incorporate the gravity, along with the aerodynamic forces R_{aero} of the main rotor, the aerodynamic forces of the tail rotor, and drag forces. The external torques M account for the rotors aerodynamic torques, and the drag torques. From a dynamical system point of view, the state of the rigid body is described by the following 12 independent variables (four additional states will be added to model the rotor dynamics)

- $X = [x \ y \ z]^T$ is the (vector) position of the center of gravity of the IMU in the inertial frame
- $V = [u \ v \ w]^T$ is the (vector) velocity of the center of gravity of the IMU in the body frame
- $Q = [\phi \ \theta \ \psi]^T$ are the Euler angles, i.e. the angles between the inertial frame and the body
- $\Omega = [p \ q \ r]^T$ are the angular rates of turn in the body frame.

With these notations, the dynamic of the 6 DOF rigid body can be rewritten under the form

$$(18) \quad \begin{cases} \dot{X} = R^T V \\ \dot{V} = -\Omega \times V + F/m \\ \dot{Q} = G(\Omega, Q) \\ \underline{\underline{I}} \dot{\Omega} = -\Omega \times \underline{\underline{I}} \Omega + M \end{cases}$$

with

$$G(\Omega, Q) = \begin{bmatrix} p + (q \sin(\phi) + r \cos(\phi)) \tan(\theta) \\ q \cos(\phi) - r \sin(\phi) \\ (q \sin(\phi) + r \cos(\phi)) \cos(\theta)^{-1} \end{bmatrix}$$

4.5. Small-scale helicopter: rotor dynamics

4.5.1. Main blades dynamics. —

4.5.1.1. Single blade modeling. — The rotor hub spin velocity along the z_b axis is noted Ω (for four blades full-scaled helicopters, each blade is independently articulated around the rotor hub). This defines three degrees of freedom: the vertical flapping angle β , the horizontal flapping angle ξ (lead-lagging) and the pitch angle θ (feathering). These notations are illustrated in Figure 4.11.

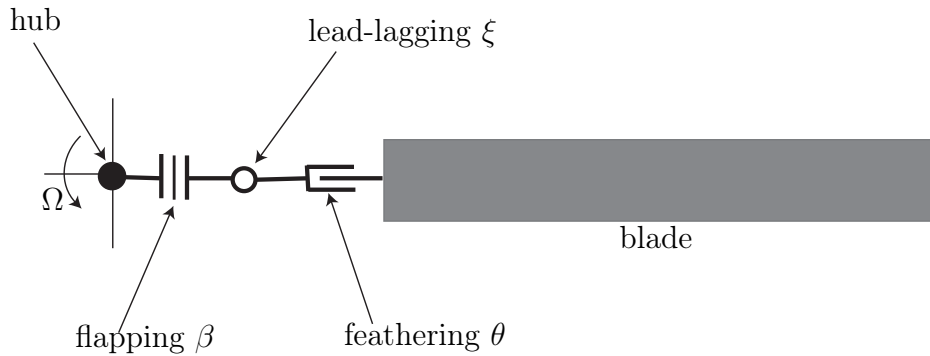


FIGURE 4.11. An articulated blade seen from above having three degrees of freedom [54].

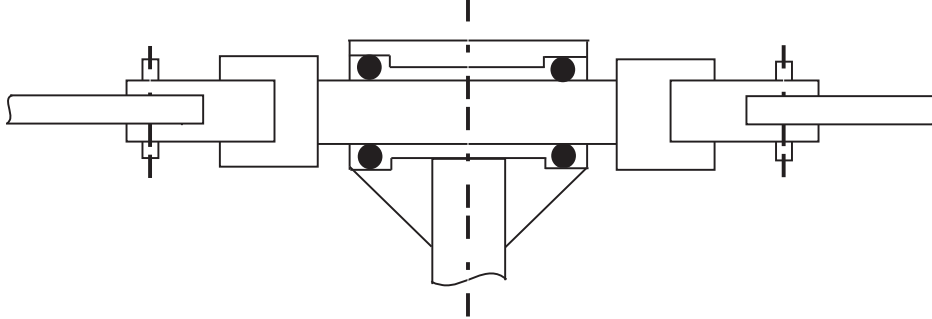


FIGURE 4.12. The particular mechanical structure of the rotor hub enables vertical flapping while reducing the “coning” phenomenon [54].

4.5.1.2. Out-of-plane flapping β . — We now consider the location of the blades during the rotor spinning. Classically, we note ψ the angle between the tail of the helicopter and the blade, and $\beta(\psi, t)$ the vertical flapping angle (see Figure 4.10). More precisely, the vertical flapping phenomenon is composed of two phenomena.

- First, there is a “coning effect” which originates in the location of the point of application of lift forces on the blade with respect to its center of gravity. One particularity of our helicopter is that a rigid rod connects the two blades of the main rotor (see Figure 4.12). This features rules out any possibility of “coning effect”. This effect, commonly found on full-sized helicopters [71, 76], has an important impact on the thrust generated by the rotor. Because of the relative rigidity of the mentioned rod, we decide to neglect this effect. Yet, the vertical flapping generate a torque M_β .
- Secondly, because of the above mentioned rigid rod, the rotor tilts while keeping the shape of a disc. Therefore, we have $\beta(\psi + \pi, t) = -\beta(\psi, t)$. The tilting is constrained by elastomer devices which act as spring-damper systems. This phenomena will be studied in details in this chapter.

4.5.1.3. Horizontal lead-lagging ξ (neglected phenomena). — Because of the vertical flapping, the center of gravity of each blade moves slightly in the direction of the center of rotor. Therefore, by the conservation of

moment of inertia, the blades accelerate.

On four blades rotor, this acceleration propagates between blades, yielding possibly strong mechanical constraints which can lead to blade break downs (see Figure 4.13). Yet, on two blades rotors this effect can be neglected because lagging blades are not coming into play.

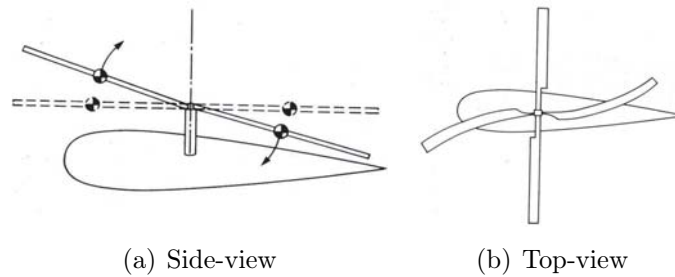


FIGURE 4.13. Strong mechanical constraints can appear on four-blades rotors due to the horizontal lead-lagging [76].

4.5.1.4. *Feathering* Θ . — The main controls on the helicopter are the pitch angles of the blades which are created by the swashplate mechanism. This mechanism is actuated by three commands, through four servodrives. This defines the pitch angle $\Theta(\Psi)$ from the cyclic and collective pitch angle control variables according to the following equation

$$(19) \quad \Theta(\Psi) = \Theta_0 - B_{lat}\delta_{lat} \cos \Psi + A_{lon}\delta_{lon} \sin \Psi.$$

In this expression, Θ_0 is changed by the collective pitch angle control variables δ_{col} while δ_{lat} and δ_{lon} (lateral and longitudinal cyclic pitch angle control variables, respectively) define the 2π periodic variation of Θ . Constant parameters B_{lat} and A_{lon} are gearing constants corresponding to lever arms of the connecting rods depicted in Figure 4.14.

4.5.1.5. *Differential equation for the vertical flapping β .* — The local relative wind speed is used to define the dynamics of β

$$\begin{aligned}
(20) \quad & \ddot{\beta} + \Omega^2\beta - 2\Omega(p \cos \Psi - q \sin \Psi) - (\dot{q} \cos \Psi + \dot{p} \sin \Psi) \\
& = \frac{1}{8}\gamma\Omega^2 \left(-B_{lat}\delta_{lat} \cos \Psi + A_{lon}\delta_{lon} \sin \Psi + \frac{1}{\Omega}(q \cos \Psi + p \sin \Psi) \right) \\
& \dots - \frac{1}{8}\gamma\Omega^2 \left(\frac{\dot{\beta}}{\Omega} \right) - \frac{k_\beta}{I_\beta}\beta
\end{aligned}$$

By expressing β over $\mathbb{R} \times \mathbb{R}$ as a 2π periodic function of ψ , it becomes possible to expand it as a Fourier series. In facts, it is verified that the first harmonic term dominates the higher orders. Therefore, we look for an approximate solution of Equation (20) in the form

$$(21) \quad \beta(\Psi, t) \approx -a(t) \cos \Psi - b(t) \sin \Psi.$$

As will appear later, the variables $a(t)$ and $b(t)$ are in facts angles of the vector aerodynamic forces R_{aero} . Assuming Equation (21), we easily compute $\dot{\beta}$ and $\ddot{\beta}$ as

$$(22) \quad \dot{\beta} = -(\dot{a} + \Omega b) \cos \Psi - (\dot{b} - \Omega a) \sin \Psi$$

$$(23) \quad \ddot{\beta} = -(\ddot{a} + 2\Omega\dot{b} - \Omega^2 a) \cos \Psi - (\ddot{b} - 2\Omega\dot{a} - \Omega^2 b) \sin \Psi$$

By matching the terms of Fourier expansion in Equations (20,21,22,23), we obtain the following second order differential equation for a and b

$$\begin{aligned}
(24) \quad & \begin{bmatrix} \ddot{a} \\ \ddot{b} \end{bmatrix} + M_A \begin{bmatrix} \dot{a} \\ \dot{b} \end{bmatrix} + M_R \begin{bmatrix} a \\ b \end{bmatrix} = M_F \\
& M_A = \Omega \begin{bmatrix} \frac{\gamma}{8} & 2 \\ -2 & \frac{\gamma}{8} \end{bmatrix}, \quad M_R = \Omega^2 \begin{bmatrix} \frac{k_\beta}{I_\beta\Omega^2} & \frac{\gamma}{8} \\ -\frac{\gamma}{8} & \frac{k_\beta}{I_\beta\Omega^2} \end{bmatrix} \\
& M_F = \Omega^2 \begin{bmatrix} \frac{\gamma}{8} & 0 \\ 0 & -\frac{\gamma}{8} \end{bmatrix} \begin{bmatrix} B_{lat}\delta_{lat} \\ A_{lon}\delta_{lon} \end{bmatrix} + \Omega \begin{bmatrix} -2 & -\frac{\gamma}{8} \\ -\frac{\gamma}{8} & 2 \end{bmatrix} \begin{bmatrix} p \\ q \end{bmatrix} \\
& \quad + \begin{bmatrix} 0 & -1 \\ -1 & 0 \end{bmatrix} \begin{bmatrix} \dot{p} \\ \dot{q} \end{bmatrix}
\end{aligned}$$

The matrix M_A is a ‘‘damping matrix’’, M_R is referred to as ‘‘stiffness matrix’’ while M_F is the ‘‘forcing matrix’’.

To simplify Equations (24) further, the following assumptions are made.

Assumptions:

- angular accelerations are much smaller than the angular rates multiplied by the rotation speed.
- the term $\frac{\gamma}{16}$ is “much smaller” than 1. This last assumption is considered because $\gamma = 4$.

With these simplifying assumptions, Equation (24) becomes, after a singular perturbation analysis,

$$\begin{cases} \frac{16}{\gamma\Omega} \left(\dot{a} - \frac{\gamma}{16} \dot{b} \right) + a = -\frac{16}{\gamma\Omega} \left(q - \frac{\gamma}{16} p \right) + \frac{8}{\gamma\Omega^2} \frac{k_\beta}{I_\beta} b + A_{lon} \delta_{lon} \\ \frac{16}{\gamma\Omega} \left(\dot{b} + \frac{\gamma}{16} \dot{a} \right) + b = -\frac{16}{\gamma\Omega} \left(p + \frac{\gamma}{16} q \right) - \frac{8}{\gamma\Omega^2} \frac{k_\beta}{I_\beta} a + B_{lat} \delta_{lat} \end{cases}$$

Noting $\tau_f = \frac{16}{\gamma\Omega} \approx 40$ ms, we finally obtain

$$(25) \quad \begin{cases} \tau_f \dot{a} + a = -\tau_f q + \frac{8}{\gamma\Omega^2} \frac{k_\beta}{I_\beta} b + A_{lon} \delta_{lon} \\ \tau_f \dot{b} + b = -\tau_f p - \frac{8}{\gamma\Omega^2} \frac{k_\beta}{I_\beta} a + B_{lat} \delta_{lat} \end{cases}$$

where γ is the Lock number, k_β is the flapping hinge restraint spring constant, I_β is the blade moment of inertia about the flapping hinge and $\tau_f > 0$. A_{lon} is the longitudinal stick to cyclic pitch gearings, B_{lat} is the lateral stick to cyclic pitch gearings for the main bar.

These two first order differential equations define, through Equation (21), the effects of the two control δ_{lon} et δ_{lat} on the motion of the helicopter and on the vertical flapping.

4.5.2. Bell-bar dynamics. —

4.5.2.1. Vertical flapping. — The Bell-bar is a relatively small bar, orthogonal to the true blades, which bears two winglets and two punctual masses. It has a rotation degree of freedom. Therefore, its vertical flapping is not subject to any mechanical torque, and is independent of the main rotor vertical flapping. The winglet’s profile is chosen such that they generate negligible lift and drag forces compared to the main rotor. Yet these generated forces, which are opposed to the centrifugal effect, determine the Bell rotor equilibrium which is parameterized by $\tilde{\beta}$. Noting

$$(26) \quad \begin{cases} c(t) = -\tilde{\beta}(\Psi = 0, t) \\ d(t) = -\tilde{\beta}(\Psi = \frac{\pi}{2}, t) \end{cases}$$

and following the same Fourier expansion methodology as for the main rotor, we obtain

$$(27) \quad \begin{cases} \tilde{\beta}(t) \approx -c(t) \cos \Psi - d(t) \sin \Psi, \\ \tilde{\Theta}(\Psi) = \Theta_0 - D_{lat} \delta_{lat} \cos \Psi + C_{lon} \delta_{lon} \sin \Psi, \\ \tau_s \dot{c} + c = -\tau_s q + C_{lon} \delta_{lon}, \\ \tau_s \dot{d} + d = -\tau_s p + D_{lat} \delta_{lat}. \end{cases}$$

The stiffness term has vanished, and the C_{lon} and D_{lat} are different from A_{lon} and B_{lat} because of mechanical constraints. The parameter $\tau_s \approx 220$ ms stands for the Bell-bar time constant. Using simplifying assumptions, we can neglect the aerodynamic forces (compared to the main blade, the loss of inertia due to the distribution of mass, close to the rotor axis, is compensated by the point masses and the aerodynamic force is weaker).

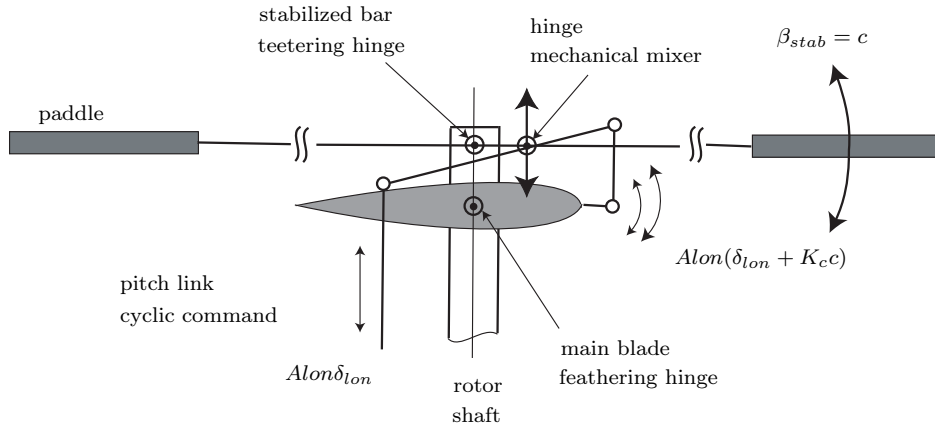


FIGURE 4.14. Bell mixer from [54].

4.5.2.2. Augmenting effect. — In spite of its discussed relative mechanical independence, the Bell bar has a significant impact on the main rotor blades, through the so-called “Bell mixer” depicted in Figure 4.14. This device has an augmenting effect on the actual lateral and longitudinal cyclic pitch angle controls.

$$(28) \quad \begin{cases} \delta_{lat}^{pale} = \delta_{lat}^{pilote} + K_d d \\ \delta_{lon}^{pale} = \delta_{lon}^{pilote} + K_c c \end{cases}$$

4.5.2.3. Stabilizing effect. — The term “stabilizing effect” can be misleading for anyone with a background in control and dynamical systems. In fact, the Bell bar does not stabilize the helicopter, but slows down the rotor dynamics by increasing its response time.

The punctual masses can be used to tune this “stabilizing effect”. Without the Bell bar, the main rotor response time would be close to 40 ms, and will be conflicting with the capabilities of a human pilot ⁽¹⁾.

4.5.2.4. Aerodynamic forces. — The following two vectors are contained in the plane of the main rotor.

$$(29) \quad \begin{cases} \mathbf{x}_r = -\cos a \mathbf{x}_b + \sin a \mathbf{z}_b \\ \mathbf{y}_r = \cos b \mathbf{y}_b + \sin b \mathbf{z}_b \end{cases}$$

Under simplifying assumptions, the drag generated by the blades is horizontal. Therefore, when the rotor is tilted, the drags of the Bell bar and of the main rotor do not cancel out. There exists a resulting drag force in the (x_b, y_b) plane and a counter-rotative torque.

This drag force must be added to the drag of the helicopter body, while the additional counter-rotative torque can be compensated by an offset in the main engine produced power, to keep the rotation speed Ω constant.

Remark 2. — *We do not try to compute the norm of the thrust generated by the rotor. Its value can be obtained experimentally, using its proportionality to the collective pitch angle δ_{col} .*

4.5.3. Summary. —

4.5.3.1. Model for the Bell-bar. — The two additional states, c and d , corresponding to the Bell-bar blades satisfy a set of two uncoupled linear first order dynamics driven by inputs corresponding to the control variables acting upon the rotor head

$$(30) \quad \begin{cases} \tau_s \dot{c} + c = -\tau_s q + C_{lon} \delta_{lon} \\ \tau_s \dot{d} + d = -\tau_s p + D_{lat} \delta_{lat} \end{cases}$$

⁽¹⁾in acrobatic helicopter contests, lightened Bell bars can be observed.

where C_{lon} is the longitudinal stick to cyclic pitch gearings, D_{lat} is the lateral stick to cyclic pitch gearings for the Bell-bar and $\tau_s > 0$. The Bell-bar has an effect on the main blades dynamics due to so-called ‘‘Bell mixer’’ mechanism. One can consider that the actual inputs in Equation (25) are ‘‘augmented’’ following Equation (28).

4.5.3.2. Model for the main blades. — The two state variables a and b correspond to a first harmonic expansion of the periodic motion of the blades. These two states satisfy coupled, linear, first order dynamics driven by inputs corresponding to the control variables acting upon the rotor head, see Equation (31). Accordingly, the vertical flapping dynamics is modified as

$$(31) \quad \begin{cases} \tau_f \dot{a} + a = -\tau_f q + \frac{8}{\gamma \Omega^2} \frac{k_\beta}{I_\beta} b + A_{lon}(\delta_{lon} + K_c c) \\ \tau_f \dot{b} + b = -\tau_f p - \frac{8}{\gamma \Omega^2} \frac{k_\beta}{I_\beta} a + B_{lat}(\delta_{lat} + K_d d) \end{cases}$$

4.5.3.3. Resulting forces and torques on the rigid body. — The aerodynamics states a , b , c , d presented above can be used to define the orientation of the rotor thrust \mathbf{R}_{aero} and the torque \mathbf{M}_{aero} acting upon the rigid body of the helicopter. \mathbf{M}_β represents the torque corresponding to the spring effect of the rotor hub. Around steady state, these are

$$(32) \quad \begin{aligned} \mathbf{R}_{aero} &= T \begin{bmatrix} -a \\ b \\ -1 \end{bmatrix} \\ \mathbf{M}_{aero} &= hT \begin{bmatrix} b \\ a \\ 0 \end{bmatrix} \\ \mathbf{M}_\beta &= k_\beta \begin{bmatrix} b \\ a \\ 0 \end{bmatrix} \end{aligned}$$

where T is the norm of the thrust generated by the main rotor, and h is the distance between the center of application of the thrust and the center of gravity of the helicopter. Around hovering, $T \approx mg$. As will be discussed later on, the thrust is depending on δ_{col} (and on z).

More generally, the magnitude of the thrust can not be easily computed. Rather, identification from flight data can be performed, and they appear to provide satisfactory results.

4.6. Small-scale helicopter: tail rotor

To compensate the torque generated by the main rotor, the tail rotor produces a force acting with a large lever arm (0.95 m in our case). This results in a torque M_{tail} which depends on the pilot's command δ_{ped} . This force also induces a lateral acceleration which is canceled out by a steady inclination of the main rotor. More complicated effects usually appear in

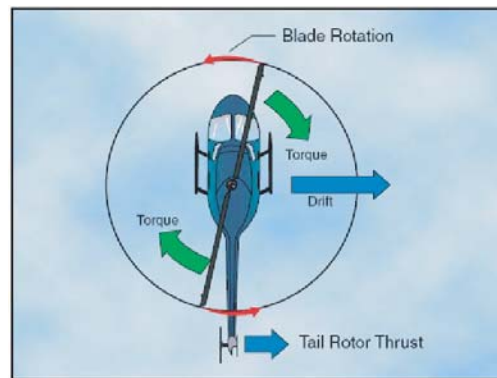


FIGURE 4.15. Tail rotor torque and drift induced by the main rotor, from [3].

practice. In particular, there exists some undesired interactions between the main rotor wake and the tail rotor.

These effects are easy to compensate by a low-level control system. We identified the response of this control system on our helicopter, results have been reported in 4.3.3. It is well represented by a 2 Hz low pass filter on the pilots orders with a feed-forward on the tail rate-gyroscope. Later, in filtering equations, we consider that the input command given to the system is δ_{ped} the output signal of the tail gyroscope.

4.6.1. Weaknesses of the model. — Before we proceed further and incorporate equations (18)-(25)-(30)-(28)-(32) into a data fusion algorithm, it is important that we comment on some of their apparent weaknesses.

4.6.1.1. Neglected phenomena. — The model (18)-(25)-(30)-(28)-(32) presented above where the forces and torques are \mathbf{R}_{aero} added to the gravity forces and the tail rotor thrust and $\mathbf{M}_{aero} + \mathbf{M}_{\beta} + \mathbf{M}_{tail}$, respectively, is sufficient for state feedback control purposes. This point was raised by [54], with extensive supportive experimental results. Yet, when the question is to estimate the attitude and position of the helicopter, it can be useful to account for further details. Among these are ground effect, actuators-induced lags and response time, and aerodynamics effect of the air flow from the main rotor passing by the body of the helicopter (rotor-induced body drag). These points will be developed in Section 4.7.2.

4.6.1.2. Parameter identification. — Another point worth mentioning is that several key parameters must be available to obtain accurate estimates from the model (18)-(25)-(30)-(28)-(32). In particular, the inertia matrix \underline{I} , and expression of the magnitude of the thrust T as a function of δ_{col} (see Equation (32)) and the tail rotor torque M_{tail} as a function of δ_{ped} , response times of both the main rotor and the Bell-bar (τ_f and τ_s in Equation (25) and (30)), as well as k_{β} , I_{β} , γ , A_{lon} , B_{lat} , C_{lon} , D_{lat} and the position of the center of gravity are needed. In Section 4.7.2, we explain how to identify these parameters.

4.7. Modeling improvements, Filter design

4.7.1. Filter design and implementation. — For state estimation, we use an Extended Kalman Filter which serves as a data fusion algorithm. The state of our filter has a total dimension of 23 in its current version. In details, we use 13 states to represent the 12 (independent) configuration states of our 6 DOF helicopter (quaternions are used to avoid well know singularities at $\theta = \frac{\pi}{2}$), we use 4 states to model the rotor dynamic (as discussed in Section 4.6), we use 6 states to model additional external (unknown) torques and forces. Theses forces and

torques represent un-modeled terms, and, most importantly, wind gusts. A first approach can be to assume that these additional unknowns satisfy some first order dynamics driven by white noises ν_F (referring to forces) and ν_Γ (referring to torques). The noise variance of the unmodeled dynamics must be taken large enough to capture the neglected dynamics, while the response time is tuned such that F and Γ are consistent with the dynamics while reducing the 25 Hz noise due to the main rotor rotation. More generally, performance certainly increases with the size of the state vector used for filtering, for example sensor drifts can be modeled this way. Limitations of the available computational power suggested us to use a smaller number of states for these unknowns.

The measurement vector sent by the micro-controller to the computation board is composed of multi-rate data. IMU data, barometer data are both updated at a 75 Hz rate, while and GPS data are updated at a 4 Hz rate. The filter equations are presented below. In implementation, the covariance matrices can be initialized with values being consistent with the ranges of dynamics under consideration of our system. In details, typical speeds and accelerations are used. The filter updates are synchronized with the 75 Hz IMU measurements. Classically, discrete-time update equations are considered.

Note P_p the 23×23 covariance matrix of the state used for prediction, P_e the 23×23 covariance matrix of the state used for estimation, Q the 23×23 covariance matrix used in the noise dynamics, R_{IMU} the 7×7 covariance matrix considered in the sensor noise definition for IMU and barometer, R_{GPS} the 6×6 covariance matrix considered in the sensor noise definition for GPS position and velocity, X_p the 23 dimensional predicted state, X_e the 23 dimensional estimated state, A the 23×23 matrix of the system obtained by linearizing dynamics (18)-(25)-(30)-(28)-(32), C_{IMU} the 7×23 matrix and C_{GPS} the 6×23 matrix obtained by linearizing the measurement equation, $\dot{X} = F(X, U)$, and T the sample time (between measurements updates).

First, we perform a prediction step from time k to $k + 1$, obtaining X_p and P_p . Then, we estimate the state through the measurements to obtain X_e and P_e . A special attention is paid to maintaining the covariance matrices positive. For that purpose a cubic term is used in

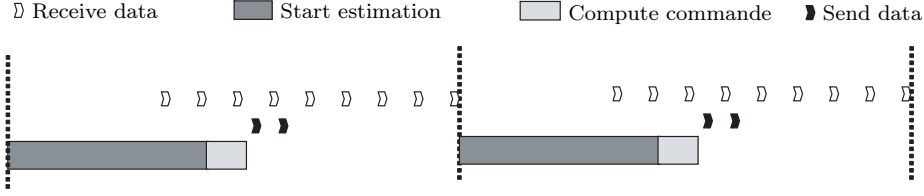


FIGURE 4.16. Succession of steps of data transfer and computation.

the discrete-time update of P_p . The updates are computed as follows

$$\begin{aligned}
 X_p &= X_e + F(X_e, U)T \\
 P_p &= (I + AT)P_e(I + AT)^T + QT + (AQ + QA^T)\frac{T^2}{2} + AQA^T\frac{T^3}{3} \\
 Y_p &= [F - \vec{g} + B_V; \Omega + B_\Omega; M]^T \\
 K &= P_p C^T (R + CP_p C^T)^{-1} \\
 X_e &= X_p + K(Y - Y_p) \\
 P_e &= (I - KC)P_p(I - KC)^T + KRK^T
 \end{aligned}$$

Where R and C correspond to GPS or IMU depending on the current measurement. According to this, the code embedded into the calculation board is structured as follows

1. **UART reading:** the UART driver gets the data sent by the micro-controller.
2. **Message decoding:** once received, the data are transmitted to the user space. These data are composed of 8-bytes words which must be decoded according to the sensor vendors proprietary protocols.
3. **Initialization:** all the values needed for state estimation are initialized. This also includes white dynamic and sensor noises, constants in use, and reference control values.
4. **Prediction:** in this step, we use the estimated state \hat{X}_{e_k} at time T_k to predict the state \hat{X}_{p_k+1} at time T_{k+1} accounting for the non-linear dynamics and the discrete sampling time T .
5. **Estimation:** in this step, we use the measurements and the predicted state \hat{X}_{p_k+1} at time T_k to update the estimated state \hat{X}_{e_k+1} at time T_{k+1} .

6. **Control:** new values of the control are computed with, e.g., a state feedback on the estimated state.
7. **Sending orders:** the UART driver is used (in interrupt mode) to transmit control values back to the micro-controller. In turn, the micro-controllers acts upon the servos.

These tasks are scheduled according to the chart given in Figure 4.16. The main loop detailed above is executed at a 75 Hz rate (approx. every 13.33 ms). Among the numerous tasks, the filter calculations take approximately 6 ms, while receiving the data takes about 10 ms (mostly waiting time), and computing and sending back the control values takes 1 ms. An interrupt driven approach must be used to run all these tasks within the allowed 13.33 ms.

4.7.2. Details of the prediction step. — In this subsection, we wish to expose the numerous details and phenomena we take into account in the model. In particular, we detail the identification of physical parameters, the effect of the collective pitch and the induced speed, the ground effect, the effect of the tail rotor pitch control, and the effect of the longitudinal and lateral cyclic pitch angles.

4.7.2.1. Identification of the inertia matrix and the center of gravity. — As mentioned in Section 4.6.1.2, we desire, for sake of state estimation accuracy, to have good estimates of the inertia matrix and the position of the center of gravity of our helicopter. For that purpose, we used the CAD CATIA® software (©Dassault Systèmes). Taking into account their various geometries and densities, 688 different parts were modeled and kinematically linked together, see Figure 4.4. In particular, the basic structure, the engine, the blades, the payload, the landing-gear, the GPS, the power supplies, the Li-Po batteries, and numerous add-ons (such as flat cables or reservoir) were modeled. The obtained information is directly used to compute lever-arms of forces and to correct the IMU and GPS information. It should be noted that, while originally located under the rotor axis, the center of gravity is now 1.9 cm behind it.

4.7.2.2. Effect of collective pitch angle in vertical climb. — The vertical motion of the helicopter is directly impacted by the value of Θ_0 which stands for the collective pitch angle. For small inflow angles, we can

model the magnitude of the generated thrust as a linear function of the mean value of the angle of attack. Linearization around hovering equilibrium values yields

$$(33) \quad T = -mg - Z_{col}(\delta_{col} - Col_s)$$

where Z_{col} can be experimentally obtained as the ratio between the vertical acceleration and the control values δ_{col} , Col_s is the mean value of the control generated by the pilot for a stationary hovering flight outside the ground effect. It can be noticed that $Z_{col}Col_s$ is greater than the gravity due to the compensation of Col_i which represents the reduction of pitch angle due to the rotor induced velocity. In practice, the control δ_{col} is directly measured by the micro-controller which captures the signal sent to the servos (the fit quality of the proposed affine law can be checked in Figure 4.18).

4.7.2.3. Ground effect. — Experimentally, substantial errors of the preceding model (33) are observed when the helicopter flies at low altitude. This phenomenon is a ground effect for which we propose to introduce corrective terms in (33). Generally, a helicopter flying close to the ground requires less power than when it is flying far from it. Numerous models have been proposed in the literature for this phenomenon seen on various aircrafts. For helicopters, [78] has proposed a ground effect theory appearing when the altitude is less than the main blade length. In this approach, an additional thrust inversely proportional to the distance to the ground is considered. Separately, [51] proposes another point of view, and model the induced speed as being inversely proportional to the square of the distance between the rotor hub and the ground, when the altitude is less than one length of blade. Here, we simply use an exponentially decaying model which fits the experimental results well. This model is

$$(34) \quad T = -mg - Z_{col} \left(\delta_{col} - Col_s + Col_{GE} \exp \left(\frac{z}{Z_{GE}} \right) \right)$$

where Col_s equals the value of the control signal sent to maintain a stationary flight when the ground effect is negligible. Parameters Col_{GE} and Z_{GE} are positive. Their values were experimentally obtained during some long time hovering flights at various altitude. In Figure 4.17, we

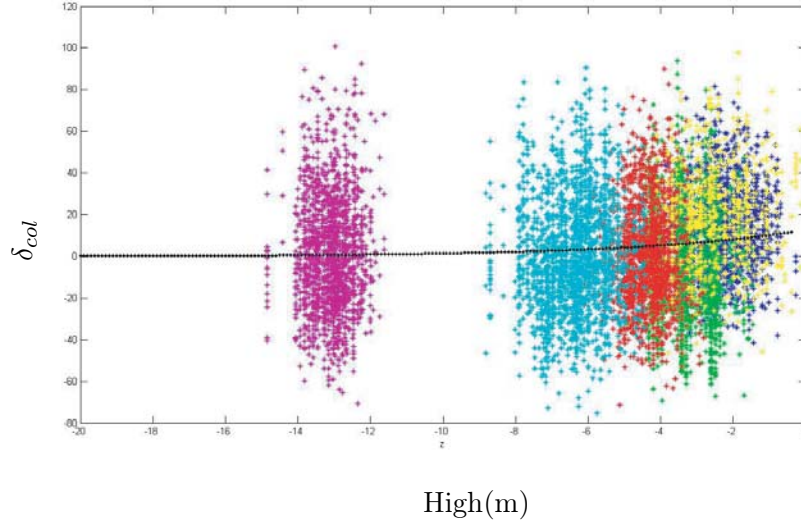


FIGURE 4.17. Ground effect impact on the vertical acceleration.

present un-filtered signals which permit to estimate these parameters. Accelerometers noises are the origin of the large variance of the data. The fitted exponential law is depicted in black. We obtain $Z_{GE} = 0.5m$ (which produces an important effect when the distance to the ground is less than two main blade length), and $Col_{GE} = 180$, $Col_S = 610$. The additional acceleration due to ground effect is around $\frac{g}{3}$ on the ground. Those value are consistent with the orders of magnitude of our helicopter.

4.7.2.4. Impact of the tail rotor pitch angle on the yaw motion. — The tail rotor pitch angle δ_{ped} is the control signal sent to the tail rotor servo. Due to the affine relation between the actual control (PWM signal) and the obtained pitch angle (see Figure 4.18), the resulting force is of the form $Y_{ped} \delta_{ped}$, where $Y_{ped} > 0$. Using the experimentally obtained values of the acceleration of the helicopter along the y -axis, we compute Y_{ped} . Then, we evaluate the resulting torque under the form $N_{ped} \delta_{ped}$ at the center of gravity by taking into account the mass and lever-arm L_{ped} . This yields

$$N_{ped} = -L_{ped} m Y_{ped}$$

In the absence of yaw variation, δ_{ped} is such that the torque due to the tail rotor thrust and the torque generated by the main rotor cancel each other. The mean value for δ_{ped} during a stationary flight, noted δ_{peds} , provides us with an estimate for the aerodynamic moment. The influence of the tail rotor on the helicopter dynamics is as follows. It generates a y -axis force F_{tail} and impacts on the rotational dynamics along the r -axis by a torque $M_{tail} = N_{ped}\delta_{ped}$. In details, one obtains

$$\begin{cases} F_{tail} = Y_{ped} \delta_{ped} \\ I_{ZZ}\dot{r} = N_{ped}(\delta_{ped} - \delta_{peds}) \end{cases}$$

where I_{ZZ} is the third diagonal term of the inertia matrix \underline{I} . Modeling improvements could include the impact of a variation of collective pitch angle δ_{col} onto the aerodynamic moment (when δ_{col} increases, the aerodynamic moment on main blade also increases, which explains why the engine throttle control is statically coupled to δ_{col} in order to keep a constant angular velocity for the rotor hub). This would imply that δ_{peds} is in fact a function of δ_{col} . Theoretically, this coupling could be identified on-line but it appears to be very difficult to estimate due to the high noise/signal ratio of the yaw gyroscope of our IMU. Therefore, we neglect this phenomenon.

4.7.2.5. Effects of the the longitudinal and lateral cyclic pitch angle onto the horizontal motion of the helicopter. —

Flapping dynamic. — According to Equations (25) and (30), the dynamics of the rotor hub are as follows

$$(35) \quad \begin{cases} \Theta(\Psi) = \Theta_0 - B_{lat}(\delta_{lat} + K_d d) \cos \Psi \\ \quad \quad \quad + A_{lon}(\delta_{lon} + K_c c) \sin \Psi \\ \tilde{\Theta}(\Psi) = \Theta_0 - D_{lat}\delta_{lat} \cos \Psi + C_{lon}\delta_{lon} \sin \Psi \end{cases}$$

where $\Theta(\Psi)$ (resp $\tilde{\Theta}(\Psi)$) is the blade pitch angle for the main bar (resp for the Bell-bar) which depends on Ψ the blade azimuth angle. Its formal harmonic decomposition, through the c and d variable in particular, can be used in identification experiments to derive K_c , K_d , A_{lon} , B_{lat} , C_{lon} , and D_{lat} . In Equation (35) collective pitch angle θ_0 depends on δ_{col} . Interestingly, these experiments can be carried out under rest conditions, and need not in-flight data (swashplate is a "kinematic" device).

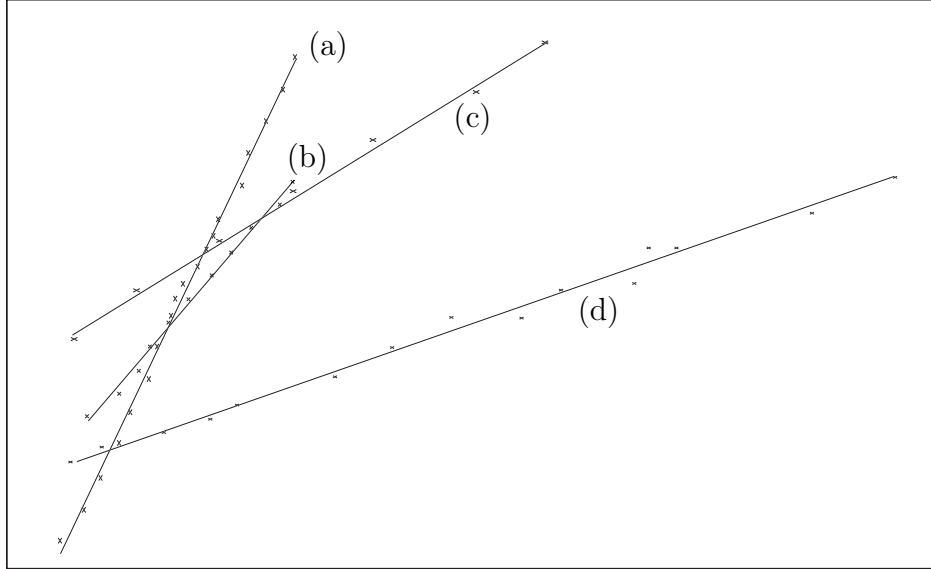


FIGURE 4.18. Affine relation between (a) δ_{lon} and $\tilde{\Theta}$, (b) δ_{lon} and Θ , (c) δ_{col} and Θ_0 , (d) δ_{ped} and pitch angle for tail rotor.

The static gains A_{lon} , B_{lat} , C_{lon} and D_{lat} play a role in the main rotor and the Bell-bar. The control variables δ_{lon} and δ_{lat} are such that their zero values correspond to a null pitch angle of the blade (without taking into account collective angle of attack). The static gain C_{lon} (resp D_{lat}) is the gain between cyclic controls and the pitch angle of Bell-bar. It is directly measured by aligning the Bell-bar with the lateral axis (resp longitudinal axis), see Figure 4.18(a). Similarly, A_{lon} (resp. B_{lat}) was experimentally obtained while keeping the Bell-bar horizontal, see Figure 4.18.

The amplifying effect of the Bell-bar on control variables is characterized by the two gains $AC = A_{lon}K_c$ and $BD = B_{lat}K_d$. Those two gains were measured as the ratio between the angle of attack of the Bell-bar and the main bar, for various values of c and d see Figure 4.18. The rotor hub spring constant k_β was obtained by attaching masses on main blade and measuring the return torque as a function of flapping of the main bar see Figure 4.19). The gain $AB = \frac{8}{\gamma\Omega^2} \frac{k_\beta}{I_\beta}$ may be computed via the value of I_β (obtained from CATIA ©Dassault Systèmes)

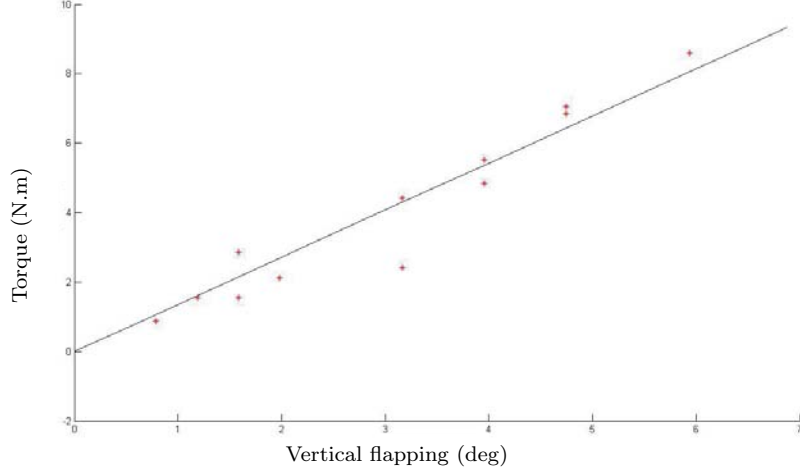


FIGURE 4.19. M_β as a function of the flapping.

Forces and torques balance. — Using the detailed expression of \mathbf{R}_{aero} given in Equation (34), Equation (32) yields

$$\mathbf{R}_{aero} = \left(g + Z_{col} \left(\delta_{col} - Col_s + Col_{GE} \exp \frac{z}{Z_{GE}} \right) \right) \begin{bmatrix} -a \\ b \\ -1 \end{bmatrix}$$

A lever arm is used to compute the aerodynamic moment

$$\mathbf{M}_{aero} = M \left(g + Z_{col} \left(\delta_{col} - Col_s + Col_{GE} \exp \frac{z}{Z_{GE}} \right) \right) \begin{bmatrix} -Z_{aero} b \\ X_{aero} - Z_{aero} a \\ X_{aero} b \end{bmatrix}$$

The torque due to the rotor hub spring effect is given by

$$(36) \quad \mathbf{M}_\beta = k_\beta \begin{bmatrix} b \\ a \\ 0 \end{bmatrix}$$

4.7.3. Details of the estimation step. —

4.7.3.1. IMU alignment angles, and scale factors. — The IMU angles do not coincide exactly with the helicopter body frame. It is possible to estimate the misalignment when the helicopter is on a perfectly horizontal

ground. In this setup, the gravity vector $-\mathbf{g}$ is clearly visible on the accelerometers. Then, Equation (17) yields estimates for the roll and pitch angles.

$$\begin{bmatrix} \Gamma_x \\ \Gamma_y \\ \Gamma_z \end{bmatrix} = \begin{bmatrix} g \sin \theta_m \\ -g \sin \phi_m \cos \theta_m \\ -g \cos \phi_m \cos \theta_m \end{bmatrix}$$

Accuracy can be gained by accounting for the accelerometers scale factors which can be estimated from the absolute value of the gravity g .

These obtained factors are used at a low-level in the measurement software to derive accurate acceleration and rate of turn information.

4.7.3.2. Sensor lever arms. — As already discussed in 4.7.3.1, the sensors are not located at the center of gravity of the helicopter. Therefore, great care must be taken when interpreting their measurements.

In particular, the sensed accelerations are different from those of the center of gravity. Consider $[x_{imu} y_{imu} z_{imu}]^T$ the position of the center of the IMU and note $XIMU$, $ZIMU$ the two distances between the IMU center and the center of gravity of the helicopter. We have

$$\begin{aligned} \begin{bmatrix} x \\ y \\ z \end{bmatrix}_{R_i} &= \begin{bmatrix} x_{imu} \\ y_{imu} \\ z_{imu} \end{bmatrix}_{R_i} - \begin{bmatrix} XIMU \\ 0 \\ ZIMU \end{bmatrix}_{R_b} \\ \mathbf{U}_{G/R_i} &= \mathbf{U}_{imu/R_i} - \Omega \times \begin{bmatrix} XIMU \\ 0 \\ ZIMU \end{bmatrix}_{R_b} \\ &= \mathbf{U}_{imu/R_i} - \begin{bmatrix} ZIMU q \\ XIMU r - ZIMU p \\ -XIMU q \end{bmatrix}_{R_b} \\ \mathbf{\Gamma}_{G/R_i} &= \mathbf{\Gamma}_{imu/R_i} - \begin{bmatrix} ZIMU \dot{q} \\ XIMU \dot{r} - ZIMU \dot{p} \\ -XIMU \dot{q} \end{bmatrix}_{R_b} \\ &\quad - \Omega \times \begin{bmatrix} ZIMU q \\ XIMU r - ZIMU p \\ -XIMU q \end{bmatrix}_{R_b} \end{aligned}$$

As appears in the equations above, the torques \dot{p} , \dot{q} , and \dot{r} play a role in the measured torques. Yet, these quantities are poorly known. Therefore, we neglect these terms in the rest of our modeling.

The GPS measures its position and its velocity in the inertial frame. To obtain the position and velocity of the helicopter, we need to account for the two lever arms $XGPS$ and $ZGPS$ as follows

$$\begin{aligned} \begin{bmatrix} x \\ y \\ z \end{bmatrix}_{R_i} &= \begin{bmatrix} x_{gps} \\ y_{gps} \\ z_{gps} \end{bmatrix}_{R_i} - \begin{bmatrix} XGPS \\ 0 \\ YGPS \end{bmatrix}_{R_b} \\ \mathbf{U}_{G/R_i} &= \mathbf{U}_{imu/R_i} - \Omega \times \begin{bmatrix} XIMU \\ 0 \\ ZIMU \end{bmatrix}_{R_b} \\ &= \mathbf{U}_{gps/R_i} - \begin{bmatrix} ZGPSq \\ XGPSr - ZGPSp \\ -XGPSq \end{bmatrix}_{R_b} \end{aligned}$$

In these expression, the rates of turn and the rotation matrix play a role. Fortunately, these are sufficiently well estimated, and it seems relevant to take them into consideration.

4.8. Experimental estimation results

In this Section, we present experimental state estimation results obtained onboard our helicopter.

To test robustness, accuracy of the model, and sensors failure, we successively turn off the GPS velocity and position information, and the gyrometer angular rate of turn signal.

4.8.1. Loss of GPS. — To simulate a GPS loss during a flight, and to evaluate the relevance of the linear dynamic model as an aid, we turn off the 4 Hz measurement and run the data fusion Kalman filter with only 0.5 Hz measurement, see Figure 4.20 and Figure 4.21. The flight under consideration is a typical forward flight at average speed. The value of Euler angle are slightly disturbed. Position and velocity are strongly updated when a new measurement occurs, but, interestingly, some parts

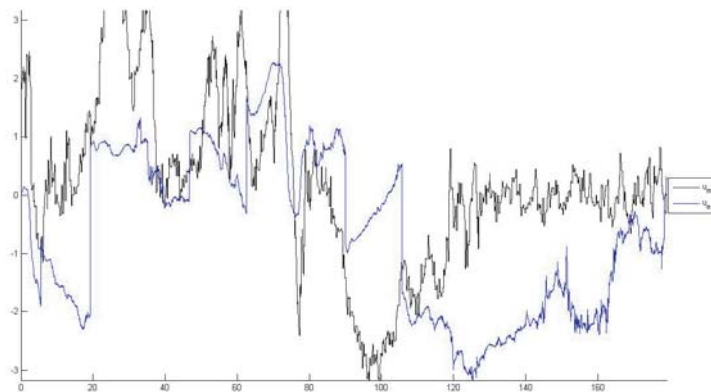
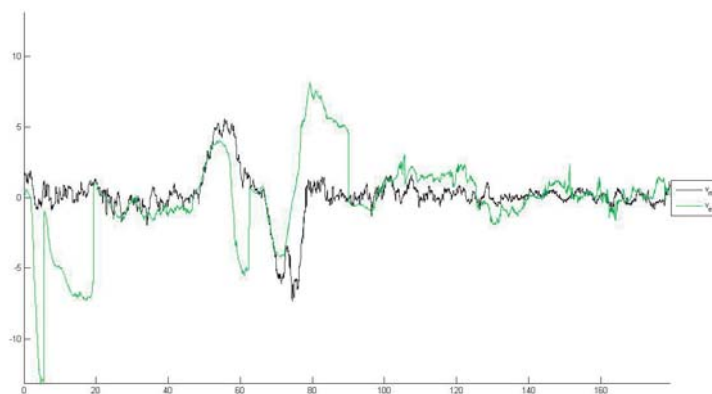
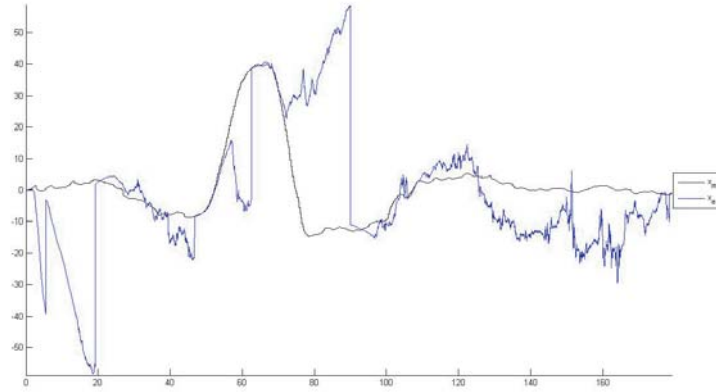
(a) Longitudinal velocity u (b) Lateral velocity v

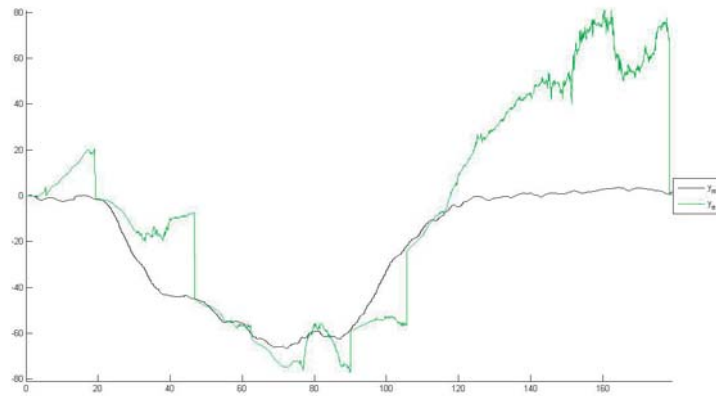
FIGURE 4.20. Longitudinal velocity $u(m/s)$ (blue) and lateral velocity $v(m/s)$ (green) estimated without GPS measurement and measured by GPS (black). Flight time (s) is reported on the x-axis.

of the flight are well predicted. In particular, the position estimates are relevant.

4.8.2. Gyrometer failure. — To test the relevance of the model with respect to the angular dynamics, we turn off the gyroscopes. Position



(a) Position x



(b) Position y

FIGURE 4.21. Position: estimated along x-axis (blue) and y-axis (green), and measured by GPS (black). Flight time (s) is on the x-axis.

and velocity errors remain large but do not grow unbounded, while angle estimates are debased.

Yet, the predicted angular rate are really close to their real values, as can be seen in Figure 4.22. In turn, the torques are well estimated. This point is consistent with the well predicted variations of the roll/pitch

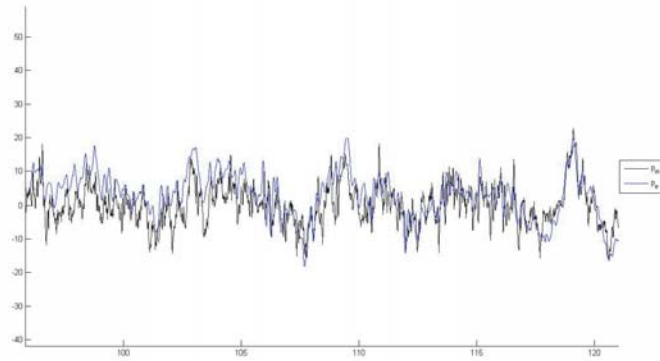
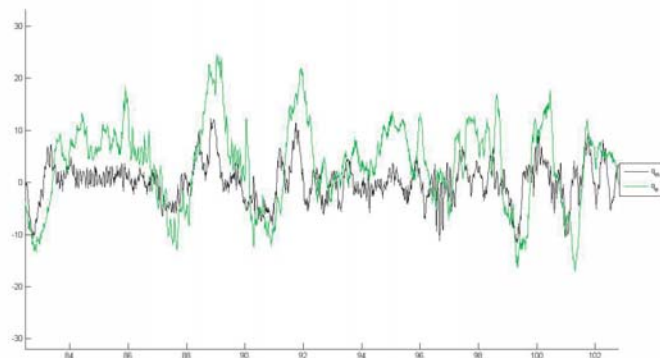
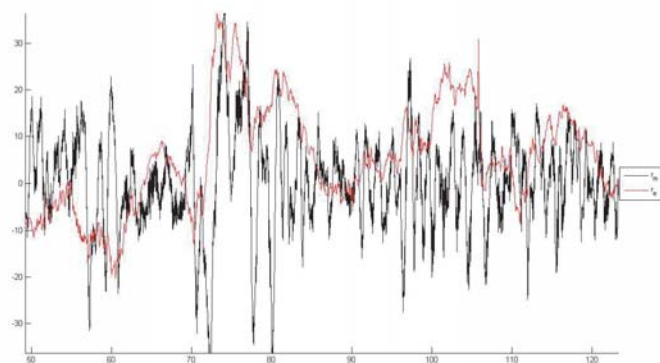
(a) Angular velocity p (b) Angular velocity q (c) Angular velocity r

FIGURE 4.22. Angular velocities p, q and r (deg/s) estimated (colored) and given from the IMU (black). Flight time (s) is reported on the x -axis.

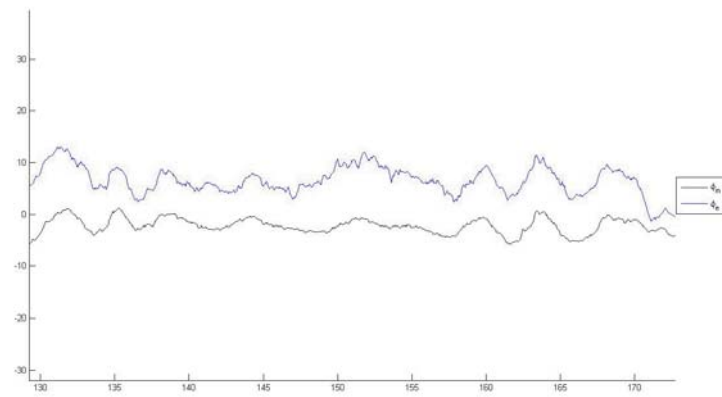
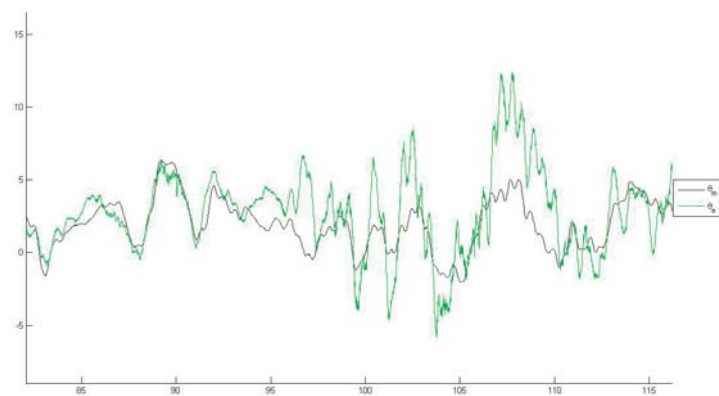
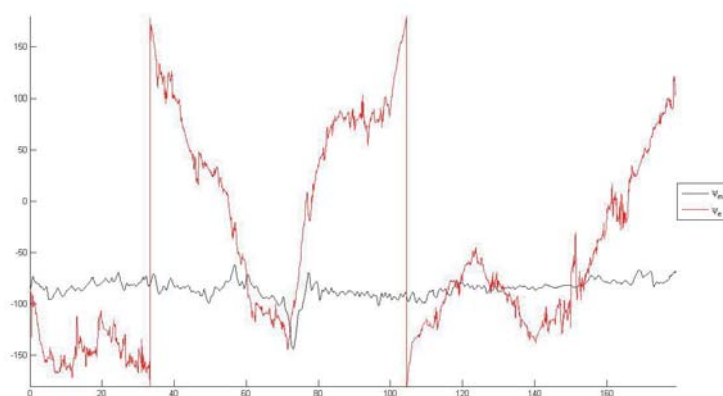
(a) Angle ϕ (b) Angle θ (c) Angle ψ

FIGURE 4.23. Angle ϕ , θ and ψ (deg): estimated (colored) and given by the IMU filter (black). Flight time (s) is reported on the x -axis.

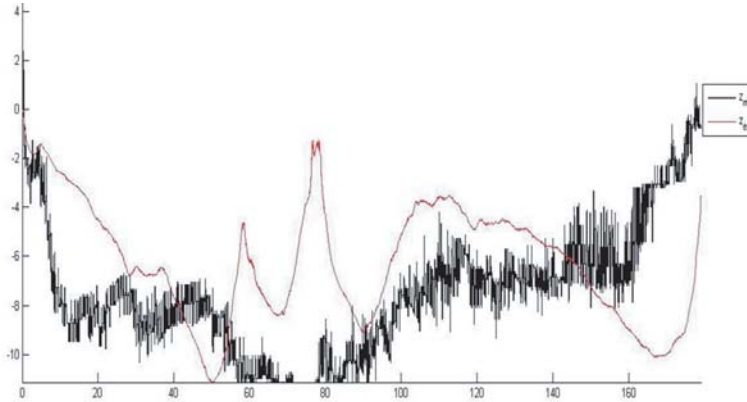


FIGURE 4.24. Altitude: estimated (blue) and measured by the barometer (black). Flight time (s) is reported on x -axis.

angles which can be seen in Figure 4.23. These track the reference values obtained from the internal 6 DOF rigid-body state estimation algorithm IMU (which we do not use otherwise).

4.8.3. Barometer failure. — To test the ground effect model, all sensors except the barometer were turned on. Results are presented in Figure 4.24).

The estimated altitude exclusively relies on the model (vertical accelerometer is too noisy to expect to yield reasonable estimates). The variance of altitude error is 3.5 m which is quite good. Altitude remains negative which is also good.

4.8.4. Data fusion with all available sensors. — Some experimental results are presented around hovering. In practice, they appear to be in great accordance with recorded videos.

4.8.5. Remaining weaknesses. — It appears that modeling of drag remains the source of non-negligible uncertainties. Also, masking effects between the two rotors seem a problem when the helicopter is moving. We hope to be able to get more insight on these points soon.

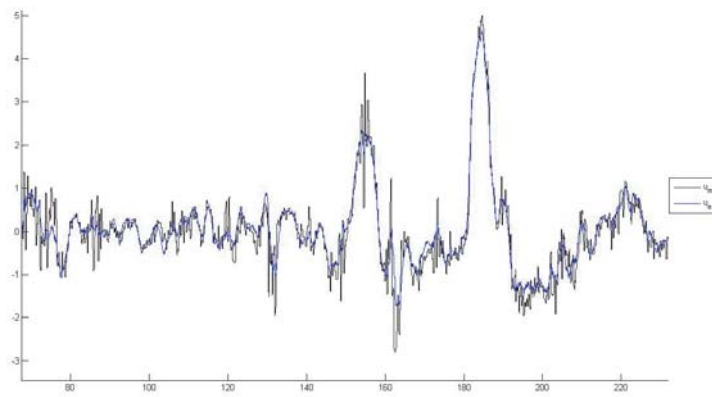
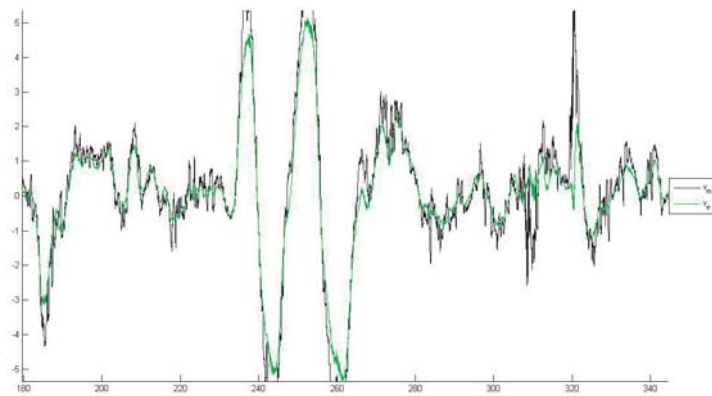
(a) Velocity u (b) Velocity v

FIGURE 4.25. Measured velocity (black) and their estimates (colored)(m.s^{-1}) over time (s)

4.9. Stabilization in hovering mode

We now briefly describe the simple control strategy we use to stabilize the helicopter in hovering flight. Rather than quaternions (which are not controllable), we consider Euler angles to describe the helicopter attitude.

The state variable are

$$[x_b, y_b, z_b, u, v, w, \phi, \theta, \psi, p, q, r, a, b, c, d]^T$$

Due to the important coupling effects of this multi-variable system, we follow [9], and consider an LQR controller. We consider that the position is expressed in the body frame instead of the reference frame. Implicitly, this approach neglects changes in the initial heading angle from one experiment to the other. Indeed, the correction due to x_b (resp y_b) only appears in δ_{lon} (resp δ_{lat}).

Stabilizing control gains of the LQR were obtained combining a simple decoupling of all axis and appropriate control variables. Weighting matrices were obtained such that closed-loop eigenvalues were consistent with our human pilot past experience.

The yaw controller is computed to mimic the damping of classic tail gyros controllers while preventing any overshoot during transients of the resulting second order system.

Other facts can be accounted for in the controller design, such as: slow/fast separation of open-loop eigenvalues, and the discussed couplings. Finally, several experiments were conducted to tune the weighting matrices. For collective pitch angle, tuning was chosen such that no oscillation could be observed in the controlled altitude

$$\begin{cases} \delta_{lon} = -K_q q - K_\theta \theta \\ \dot{q} \approx \frac{-MgZ_{aero} + k_\beta}{IYY} ALON \delta_{lon} - \frac{KQ}{IYY} q \end{cases}$$

This yields a second order equation involving the main bar response time τ_p and the inertia matrix \underline{I}

$$\frac{1}{K_\theta} \frac{IYY}{A_{lon}(k_{beta} - MgZ_{aero})} \ddot{\theta} + \frac{1}{K_\theta} \left(K_q + \frac{KQ}{A_{lon}(k_\beta - MgZ_{aero})} \right) \dot{\theta} + \theta = 0$$

$$(37) \quad \begin{cases} \omega_{lon0} = \frac{1}{\tau_f + IYY/KQ} \\ K_\theta = \omega_{lon0}^2 \frac{IYY}{ALON(-MgZ_{aero} + k_\beta)} \\ K_q = \frac{1}{ALON(-MgZ_{aero} + k_\beta)} (2 \xi \omega_{lon0} IYY - KQ) \end{cases}$$

Remark 3. — Due to our spring/damping system for filtering at 25 Hz we get a resonance at 3 – 4 Hz which prevents us from using high gain on roll and pitch gyro.

Following a similar procedure for the roll axis, we get

$$(38) \quad \begin{cases} \delta_{lat} = -K_p p - K_\phi \phi \\ \omega_{lat0} = \frac{1}{\tau_f + IXX/KP} \\ K_\phi = \omega_{lat0}^2 \frac{IXX}{BLAT(-MgZ_{aero} + k_\beta)} \\ K_p = \frac{1}{BLAT(-MgZ_{aero} + k_\beta)} (2 \xi \omega_{lat0} IXX - KP) \end{cases}$$

Once this first low-level controller is designed, one can now focus on acceleration by assuming that the control acts directly on the helicopter orientation angles. This yields

$$\begin{aligned} \delta_{lon} &= -K_q q - K_\theta \theta - K_u u - K_x (x_b - x_{b_{cons}}) \\ \theta &\approx \frac{-\delta_{lon} - K_u u - K_x x_b}{K_\theta} \\ \ddot{x}_b &\approx -g \theta - KU u \\ \frac{K_\theta}{g K_x} \ddot{x}_b + \left(\frac{K_u}{K_x} + \frac{KU K_\theta}{g K_x} \right) \dot{x}_b + x_b &= x_{b_{cons}} \end{aligned}$$

the gains appearing in the previous equations, following an approach similar to the collective pitch control, we analyze experimental runs and study the pilot's commands.

Eventually, we design a closed-loop control for the altitude and its time derivative. Some experimental results are presented in Figure 4.29. Position estimates around hovering are reported.

4.10. Future directions

In this chapter, we have focused on incorporating important details about the vehicle flight dynamics within an extended Kalman filter system. The results of estimations using an experimental small-scale helicopter demonstrate the relevance of an approach which relies solely on

low-cost sensors. Finally, we used the real-time estimated state vector in a feedback controller. Because of the substantial coupling terms in the multivariable dynamics (see [9]), an LQR design was used in an approach similar to [33]. Slow/fast decomposition of the dynamics and the knowledge of our pilot control performance were used to sketch the values of the weighting matrices. The controller successfully stabilized the helicopter in hovering flight. Typical results are presented in Figure 4.29. During this 5 min autonomous flight, the position error remained within a three-dimensional cylinder 1 m high and 3 m in radius. The flight was performed outdoors, in a wind of 20 km/h. The variance of the error in the ground position was approximately 1 m, which is close to the GPS error. In the vertical direction, the error variance was below 1 m, which is close to the absolute error of the barometer. For velocities, the variance of the error was around $0.75 \text{ m}\cdot\text{s}^{-1}$ horizontally, and $0.5 \text{ m}\cdot\text{s}^{-1}$ vertically. The angular error remained within 3 deg in roll and pitch and 15 deg in heading.

We feel that these results can be improved upon, especially by tuning the controller further. However, most importantly, they represent a first step toward future developments which will incorporate forward motions and trajectory-following techniques.

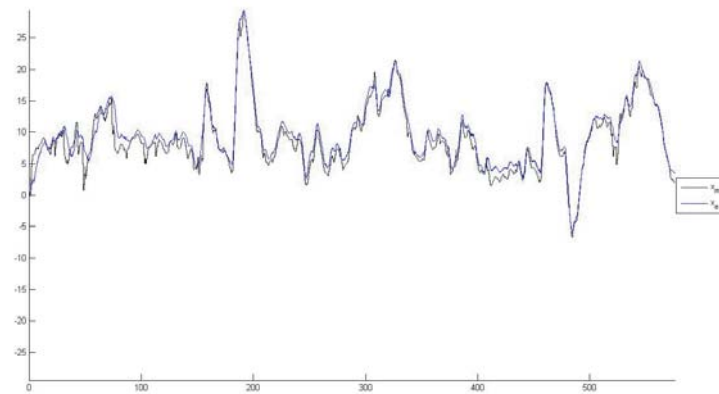
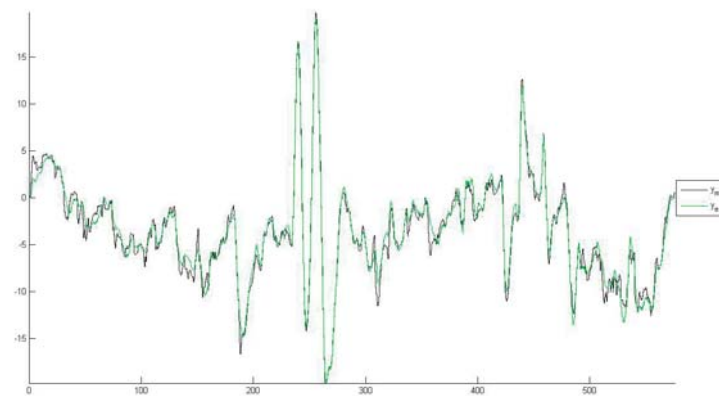
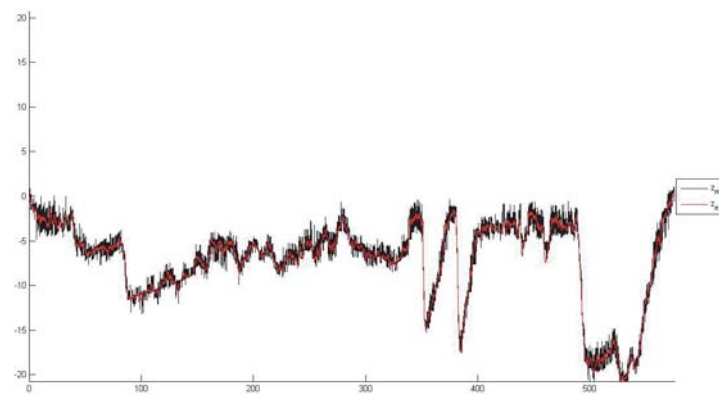
(a) Position x (b) Position y (c) Position z

FIGURE 4.26. Measured position (black) and their estimates (m) (colored) over time (s)

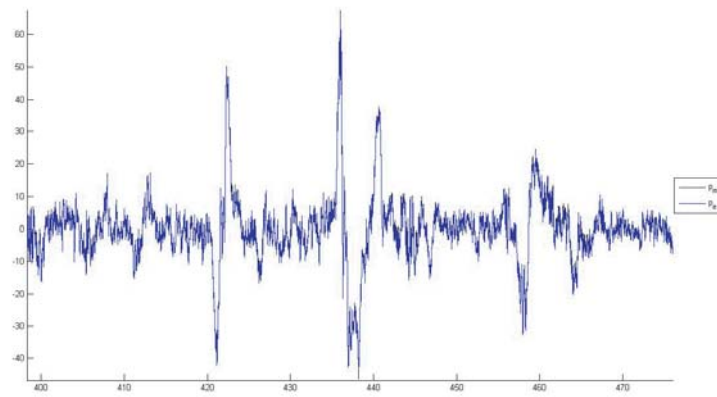
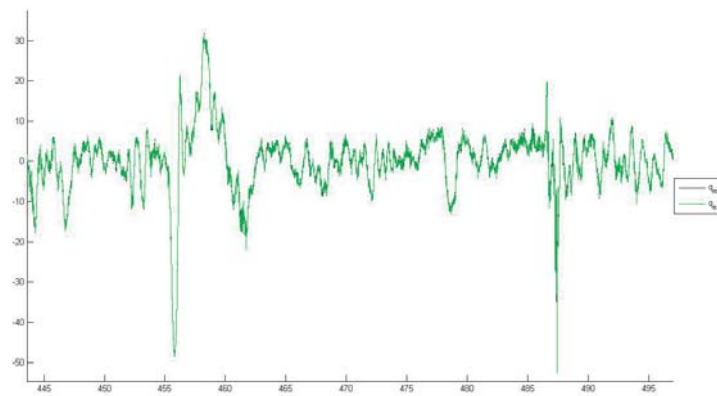
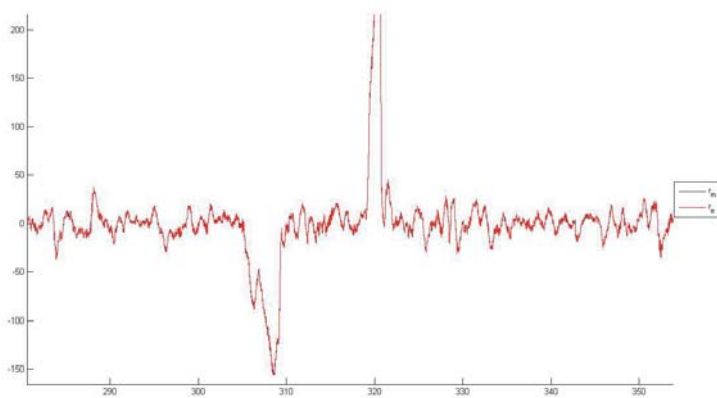
(a) Angular velocity p (b) Angular velocity q (c) Angular velocity r

FIGURE 4.27. Angular velocities measured (black) and their estimates (colored) ($\text{deg}\cdot\text{s}^{-1}$) over time (s).

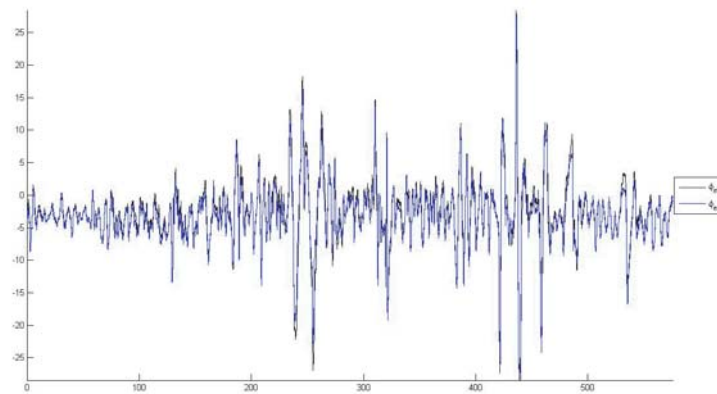
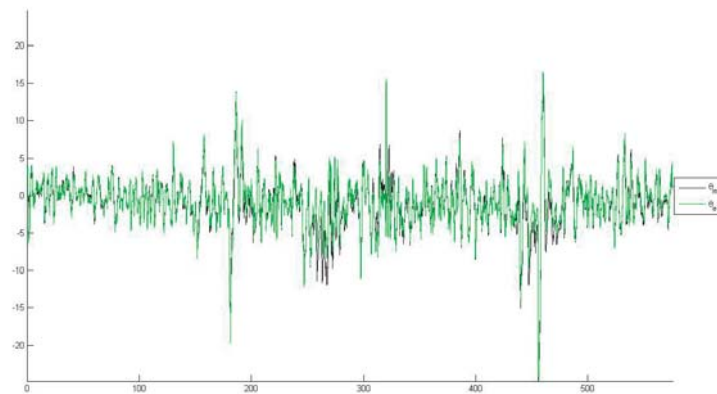
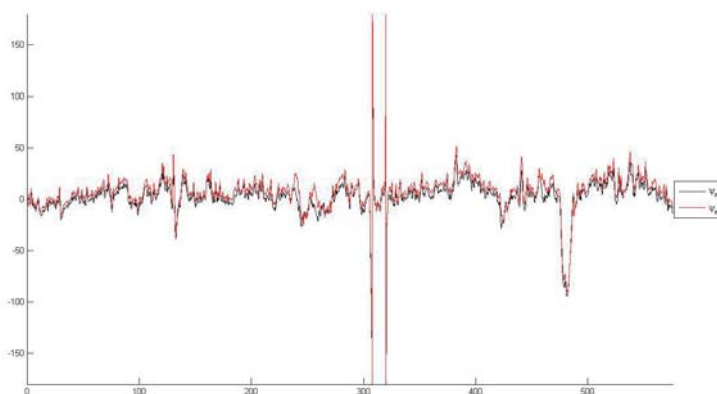
(a) Angle ϕ (b) Angle θ (c) Angle ψ

FIGURE 4.28. Attitude angles measured (black) and their estimates (colored) (deg), over time (s).

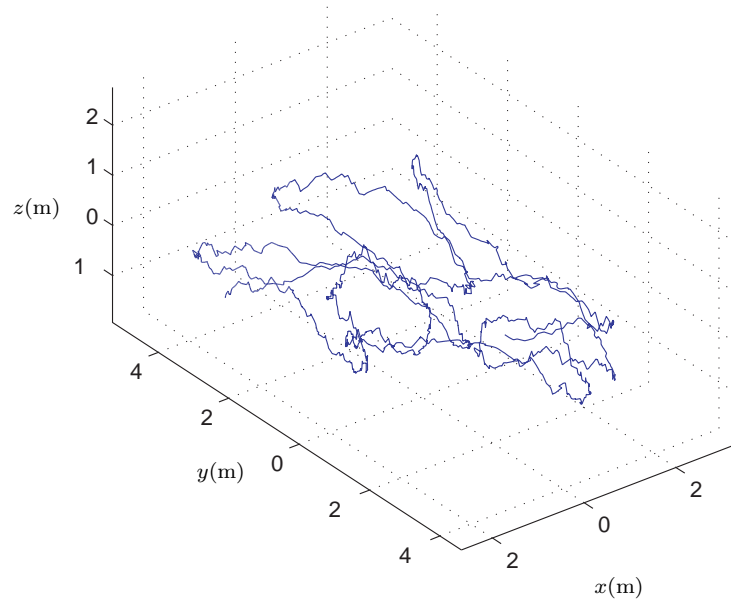


FIGURE 4.29. Position estimates during a hovering flight.

PART III

POSITIONING TECHNIQUES USING MAGNETIC FIELD DISTURBANCES

CHAPTER 5

TAKING ADVANTAGE OF MAGNETIC-FIELD DISTURBANCES IN NAVIGATION

Un problème crucial pour le contrôle-commande des engins aériens ou terrestres dont nous avons considéré des exemples aux Chapitres 2 et 4 est celui de l'estimation d'état à partir des capteurs embarqués. Nous avons montré, pour chacun des deux exemples considérés, comment développer et mettre en œuvre des techniques d'observateurs pour le filtrage et la fusion de données multi-capteurs.

Néanmoins d'importants problèmes demeurent. En particulier, il est communément admis que la technologie GPS est nécessaire pour l'estimation des positions. L'information absolue permet un recalage, à basse fréquence, relativement aisé. Il est connu que ce signal souffre de sérieux défauts: de nombreuses aberrations dues aux multi-trajets des signaux (en particulier dans les environnements urbains) peuvent apparaître subitement, de même que la disponibilité des différents satellites de la constellation peut être rapidement mise en cause du fait des obstacles. En outre, l'utilisation du GPS dans un contexte militaire est très problématique étant donnée la facilité avec laquelle il peut être brouillé. Enfin, pour les interventions à l'intérieur de bâtiments, le GPS est totalement inutilisable (sauf, de manière très dégradée, près des fenêtres et portes).

Conscients de tous ces problèmes, nous avons cherché à développer une technique d'estimation de position qui n'utilise pas le GPS. A l'intérieur de bâtiments, le champ magnétique est fortement perturbé. On pourrait en conclure que les signaux magnétométriques ne sont pas exploitables dans le cadre de la fusion de données avec des capteurs inertiels. Notre méthode vient en contradiction avec ce constat. Bien au contraire, en

utilisant les équations de Maxwell qui structurent ces perturbations, il est possible de déduire de précieuses informations sur le vecteur vitesse du porteur des capteurs.

We address here the problem of position estimation for a rigid body using an IMU. We present a Kalman filtering technique which takes advantage of the magnetic disturbances usually observed indoors. This is an important topic for military operations in urban areas, where a GPS signal is often unavailable. This approach yields significant improvements in estimation accuracy. We illustrate our technique with several experimental results obtained with a low-cost IMU.

5.1. Introduction

As exemplified in Chapters 2 and 4, numerous military and civilian control applications require high-accuracy estimations of the position, speed, and attitude of a solid body. A widely considered solution (see e.g. Chapter 3), is to use embedded IMUs. Signals from accelerometers and gyroscopes (and possibly magnetometers) can be used to derive position information through a double integration process [35, 28]. Because of sensor drift, this approach requires very high-precision IMUs (not belonging to the MEMS class that we are considering) such as those found in certain full-sized aircraft, military submarines, and missiles. When cost, space, and weight constraints become stringent, other solutions need to be used. Two prime examples are provided by the fusion of sensors in ground vehicles equipped with odometers and a GPS receiver (for outdoor and non-military-critical applications, as considered in Chapter 2), and computer vision using cameras for indoor robotics. It is interesting to get an idea of prices and the performance obtained. Typically, a ground navigator based on IMU measurements used for petroleum research costs more than USD 20,000, and its position estimate drifts by 3 nautical miles per hour (when the navigation system is used only during maneuvers and it is manually forced to perform a zero update around



FIGURE 5.1. A typical platoon of soldiers in action as envisioned in the BOA project. ©L.Chabane-BD Médias for Délégation Générale pour l'Armement (DGA). A team leader keeps track of his soldiers thanks to real-time position information reported on his arm portable display.

points where the vehicle is stationary, the drift in position can be reduced to 100 m for a trip of 3 nautical miles).

A recent trend has been to rely heavily on the well-known GPS technology. This technology is very appealing for low-weight, low-cost, and low-size applications (see e.g. [42]). However, it suffers from some major drawbacks. It has limited availability (especially in the context of military operations), its accuracy is roughly 10 m, and the GPS signal is quite weak. GPS is very poorly useable between buildings and in forests. Very importantly, it is not available indoors. Alternative solutions are under development, most of which rely on computer vision using cameras or lasers (see e.g. [93]), for example to match partial information obtained from maps or to progressively construct a map of the neighborhood.

However, the use of cameras and other optical devices often has to be excluded. In numerous missions (e.g. when soldiers or police are to take control of a building or firefighters are to rescue people from a smoky room), lighting conditions, smoke, or high temperatures totally prevent cameras from being used. The recent progress in very low-cost (less than USD 1,500), low-weight (less than 100 g), low-size (less than 3 cm²) IMUs has spurred a broad interest in the development of IMU-based positioning technologies. These MEMS-based IMUs appear to have rapidly increasing capabilities. Several manufacturers are announcing new models for under 5,000 USD capable of sensing less than 20 deg/hr.

So far, there have been no reported experiments on estimating positions using such a low-cost IMU. In the literature, these IMUs have been used only for attitude estimation (see e.g. [19, 52, 15] for an application to the closed-loop control of mini-UAVs). Some tentative work (using higher-end IMUs) has addressed the problem of velocity estimation. In these cases, the speed information was obtained from a GPS receiver using the Doppler effect (see [35] for details of the quality of the measurement information obtained) or from odometers (in the case of ground vehicles). For ground vehicles, position is usually primarily derived from GPS data complemented with higher-frequency measurements using an IMU and a magnetometer (see e.g. [92]). Our focus is on indoor missions involving humans. It is desired to remotely estimate their positions. During preliminary tests, it quickly became apparent to us that, given a poorly known model of the dynamics, it was impossible to obtain a position error below 50 m after a few minutes of experiments from a low-cost IMU (e.g. a 3DMGX1 from Microstrain[®]). High-end IMUs are usually much too heavy for human-oriented applications. Further, while the GPS signal is unavailable indoors, experimental measurements have shown that the magnetic field in a typical office building is strongly disturbed (by the building structure, electrical equipment, computers, and cell phones, among other things). Consequently, classic estimation algorithms based on heading measurements are very inefficient in such a context. For the sake of illustration, we report the variation of the magnetic field strength inside an office building in Figure 5.2.

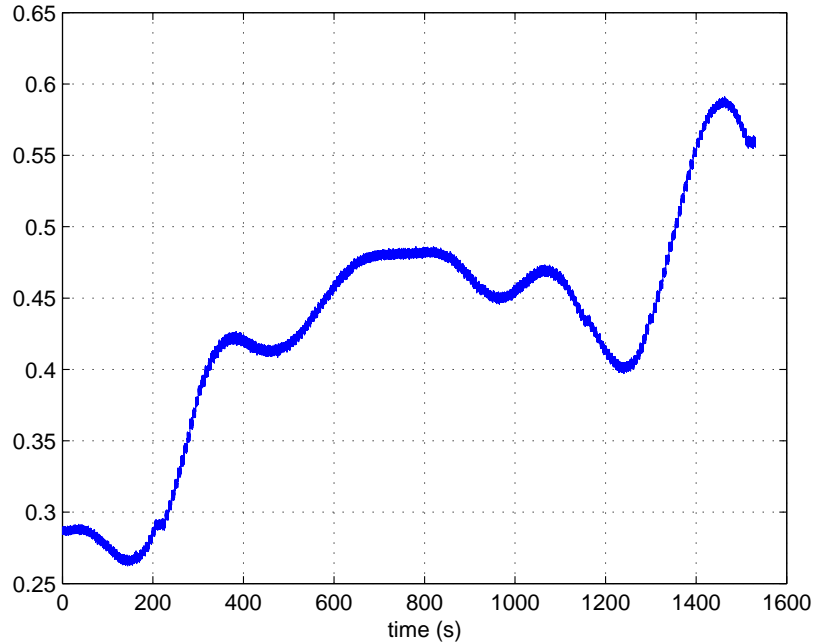


FIGURE 5.2. Variation of the magnetic field norm during a 2.4 m horizontal displacement inside a business building office.

Our claim is that these disturbances (which are assumed to be constant) can actually be used to improve the position estimation. Our work is related to the approach advocated in [41] for gravimetry-aided navigation. Very importantly, our approach does not rely on any a priori magnetic map. It simply uses Maxwell's equations. In words, we note that, in a disturbed magnetic field, it is possible to determine when a solid body equipped with a magnetometer is moving. If the body moves, then the sensed magnetic field must change according to Maxwell's equations. If the magnetic measurements do not change significantly, then the solid body is not moving. This permits us to rule out velocity drifts in our estimation. Ultimately, this improves the position information obtained by integrating the velocity estimate. Some experimental results that we present, obtained using a very low-cost inertial unit on a simple, preliminary test bed, lead us to believe that it is possible to estimate the position

of a man carrying a low-cost IMU who is taking part in the investing of a building. This objective fits into the context of *network-centric warfare* (as defined in [70]), and was studied in the project “Bulle Opérationnelle Aéroterrestre” (BOA), led by the Délégation Générale pour l’Armement (DGA) for the French Department of Defense. A typical mission in the BOA environment is depicted in Figure 5.1.

The chapter is organized as follows. In Section 5.2, we define the position estimation problem. The notation required is presented. In Section 5.3, we describe our use of magnetic disturbances. In particular, we focus on eliminating bias in velocity estimates. In Section 5.4, we present some experimental results and give implementation details. In Section 5.5, we conclude, and suggest several directions for improvement.

5.2. Problem statement

We do not describe in details the dynamics sensed by the IMU. Our primary goal is to stress the information from the magnetic sensor that can be exploited. When actually implementing the estimation filter, we often include numerous terms in the dynamics model for sake of accuracy, but very good estimates can be recovered from the basic equations we present here.

5.2.1. Coordinate frames, system of equations, notations. —

We consider the motion of an IMU (viewed as a material point) located at the center of gravity of a moving body we wish to estimate the position of. The system can simultaneously rotate and translate. It has six degrees of freedom. A body reference fixed frame with origin at the center of gravity of the IMU can be considered. In that case, the x , y and z axis are the IMU axis (i.e. are consistent with the inner sensors orientations). In the following, subscript $_b$ refers to this body frame.

As inertial reference frame, we consider the NED frame: North-East-Down, the x axis is tangent to the geoid and is pointing to the north, the z axis is pointing to the center of the earth, and the y axis is tangent to the geoid and is pointing to the East. Subscript $_i$ refers to this inertial frame.

The IMU delivers a 9 parameters vector $Y = [Y_V \ Y_\Omega \ Y_M]^T$ obtained from a 3-axis accelerometer, a 3-axis gyros and a 3-axis magnetometer. Measurements are noisy and biased. Classically, we consider that the accelerometer signal Y_V has a bias B_V (independently on each axis) and suffers from additive white noise μ_v , that both the magnetometer signal Y_M and the gyros signal Y_Ω have additive white noises μ_M and μ_Ω , respectively. Finally, there is a drift B_Ω on Y_Ω . It is possible to consider unknown scale factors to increase filtering accuracy, but these are not necessary in a first approach. We denote by B_V the drift off the accelerometer and by B_Ω the drift off the gyros. Noting F the external forces (other than gravitational) acting on the IMU, and R the rotation matrix from the inertial frame to the body frame, we can write the measurement equations

$$(39) \quad \begin{cases} Y_V = F - R\vec{g} + B_V + \mu_V \\ Y_\Omega = \Omega + B_\Omega + \mu_\Omega \\ Y_M = M + \mu_M \end{cases}$$

where \vec{g} stands for the gravity, and M is the magnetic field in the body frame. For the bias vector $B = [B_V \ B_\Omega]^T$, several models can be considered depending on accuracy requirements. A second order damped oscillator driven by a white noise is a good choice. Classically, in filter equations, bias will be added in an extended state.

From a dynamical system point of view, the state of the rigid body is described by the 12 following independent variables

- $X = [x \ y \ z]^T$ is the position of the center of gravity of the IMU in the inertial frame
- $V = [u \ v \ w]^T$ is the vector velocity of the center of gravity of the IMU in the body frame
- $Q = [\phi \ \theta \ \psi]^T$ The Euler angles, i.e. the angles between the inertial frame and the body
- $\Omega = [p \ q \ r]^T$ is the angular rate of turn in the body frame.

The input vector of the dynamics are the forces $F = [F_u \ F_v \ F_w]^T$ and torques $\Gamma = [\Gamma_u \ \Gamma_v \ \Gamma_w]^T$. We call R the rotation matrix between the inertial and the body reference.

Remark. — To avoid the well known singularities when angles cross $\frac{\pi}{2}$, quaternions can be used to represent the Euler angles. For sake of simplicity, we do not present quaternions equations but they certainly are handy in this situation.

$$(40) \quad R = \begin{bmatrix} c\psi c\theta & s\psi c\theta & -s\theta \\ -c\phi s\psi + s\phi s\theta c\psi & c\phi c\psi + s\phi s\psi s\theta & c\theta s\phi \\ s\phi s\psi + c\phi s\theta c\psi & -s\phi c\psi + c\phi s\psi s\theta & c\theta c\phi \end{bmatrix}$$

where, again, for conciseness, $c\psi$ and $s\psi$ stand for $\cos \psi$ and $\sin \psi$, respectively.

5.2.2. Equations of motion. — The matrix of inertia of the system is unknown. It is approximated by the identity matrix. Models for the unknown forces F and torques Γ may be chosen. A basic choice to model them as the output of a first order stable system driven by white noises. Indirectly, the variance of the white noise is used to specify the manoeuvring capabilities of our system

$$(41) \quad \begin{aligned} \dot{F} &= -\frac{F}{\tau_F} + \nu_F \\ \dot{\Gamma} &= -\frac{\Gamma}{\tau_\Gamma} + \nu_\Gamma \end{aligned}$$

where τ_F, τ_Γ are positive constants. In summary, using the matrix R defined in Equation (40), we get the following system dynamics

$$(42) \quad \begin{cases} \dot{X} = RV \\ \dot{V} = -\Omega \times V + F \\ \dot{Q} = G(\Omega, Q) \\ \dot{\Omega} = \Gamma \end{cases}$$

with

$$G(\Omega, Q) = \begin{bmatrix} p + (q \sin(\phi) + r \cos(\phi)) \tan(\theta) \\ q \cos(\phi) - r \sin(\phi) \\ (q \sin(\phi) + r \cos(\phi)) \cos(\theta)^{-1} \end{bmatrix}$$

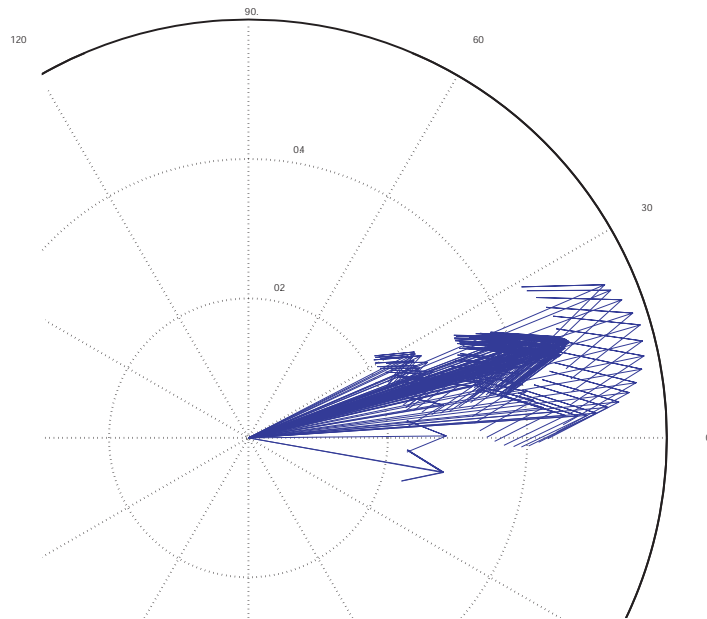


FIGURE 5.3. Variation of (projected) magnetic field during during a 2.4 m horizontal displacement inside a business building office. Heading information is strongly altered.

5.3. Using magnetic field gradients increase observability

The measurements obtained from the IMU are expressed in the body coordinates frame and are related to a vector in the inertial frame by the matrix R through the relation

$$(43) \quad M = RM_i$$

The usual way to take the magnetic measurements into account is to consider that it gives a direct reading on the attitude, namely a direct measure of magnetic heading vector. This is a quite valid assumption except when there are magnetic disturbances. This approach gives very good results, *provided magnetic disturbances are negligible*. Yet, as can be

seen in Figure 5.2 and Figure 5.3, these disturbances are not negligible indoor, e.g. in typical business offices or houses. One can notice the important variations of magnetic heading when making a simple (slow) 2.4 m horizontal displacement in such a environment, and also remark the large variations of the magnetic field norm during the same horizontal displacement.

Using the inertial frame, we use Maxwell's equations [2] to derive the following three properties

- *The magnetic field is stationary.* According to Faraday's law of induction in the absence of electrical sources $\frac{\partial M_i}{\partial t} = 0$. In other words, the magnetic field is a function of the position only. We note it $M_i(X)$.
- *The magnetic field is a potential field.* According to Ampère's law, in the absence of electric and magnetic sources, $\text{curl}(M_i) = 0$. Therefore, there exists a scalar function $h(X)$ such that $M_i = \nabla h$.
- *The divergence of the magnetic field is zero:* $\text{div}(M_i) = 0$. Thanks to the previous property, this implies $\Delta h = h_{xx} + h_{yy} + h_{zz} = 0$

In the body frame, one can differentiate (43) to get the following differential equation thanks to a chain rule

$$(44) \quad \dot{M} = -\Omega \times M + R\nabla^2 h R^T V$$

To estimate the gradient of M , we perform an estimation in the inertial frame. We extend the state by adding the magnetic field M and the independent gradients H . Due to the three properties presented above, there are only five independent gradients to look for. These are, in the inertial frame $H \triangleq [h_{xx} \ h_{xy} \ h_{xz} \ h_{yz} \ h_{zz}]^T \in \mathbb{R}^5$.

A first approach (given for its tutorial value) to this estimation problem can be to assume that the gradient of the magnetic field satisfy some first order dynamics driven by white noises ν_H . In other words, we can assume that

$$(45) \quad \dot{H} = -\frac{H}{\tau_H} + \nu_H$$

where τ_H is a positive constant. In practice, this model is not really sufficient to capture the richness of the magnetic field gradients dynamics. Typical (from experiment) variations of one such gradient is reported

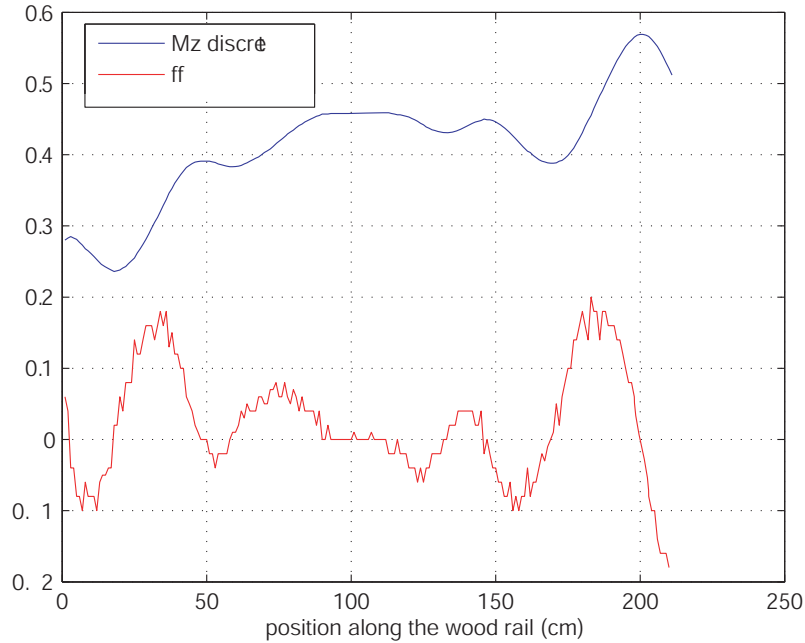


FIGURE 5.4. Histories of h_{zx} the partial derivative of the z component of the magnetic field in the x inertial direction during a 2.1 m move at constant speed along a wood (therefore non-magnetic) rail.

in Figure 5.4. Depicted slopes suggest second derivatives are not neglectable. For sake of performance, it is recommended to use sophisticated higher order dynamics instead of (45) (angles, and velocities estimate can actually be used in the definition of this dynamics). Finally, with this approach, the extended state we consider has 20 scalar variables. We will use an extended Kalman filter to estimate it. Equation (44) plays a key role in this observation problem. It is the only one giving absolute information on V .

5.4. A possible filter design

5.4.1. Filter design. — The state of our filter is composed of the 12 (independent) configuration states for our 6 DOF IMU, 6 states used to

model the torques and forces (with can be optionally complemented by 6 extra states to completely model the dynamic on F and Γ with second order dynamics for example), 6 states to model the sensor error (which can become 12 with a second order modeling approach), 3 to model the magnetic field M , 5 for its independent derivatives H (7 more can be considered using second order models). The state vector used to obtained the experimental results presented here is composed of 38 variables. The filter equations are presented below. In implementation, the covariance matrices can be initialized with values consistent with the ranges of dynamics under consideration (accelerations, speeds...) of our system. The filter updates are synchronized with the 75 Hz IMU measurements. Classically, discrete update equations are considered. A special attention is paid to maintain the covariance matrices positive. Note P_p the 38×38 covariance matrix of the state used for prediction, P_e the 38×38 covariance matrix of the state used for estimation, Q the 38×38 covariance matrix used in the noise dynamics, R the 9×9 covariance matrix considered in the sensor noise definition, X_p the 38 dimensional predicted state, X_e the 38 dimensional estimated state, A the 38×38 matrix of the system obtained by linearizing dynamics (42)-(44)-(45), C the 9×38 matrix obtained by linearizing the measurement Equation (39), $\dot{X} = F(X)$, and T the sample time (between measurements updates). We first do a prediction from time k to $k + 1$, obtaining X_p and P_p , and then estimate the state through the measurements to obtain X_e and P_e . The updates are computed as follows

$$\begin{aligned}
 X_p &= X_e + F(X, U)T \\
 P_p &= (I + AT)P_e(I + AT)^T + QT + (AQ + QA^T)\frac{T^2}{2} + AQA^T\frac{T^3}{3} \\
 Y_p &= [F - R\vec{g} + B_V; \Omega + B_\Omega; M]^T \\
 K &= P_p C^T (R + C P_p C^T)^{-1} \\
 X_e &= X_p + K(Y - Y_p) \\
 P_e &= (I - KC)P_p(I - KC)^T + KRK^T
 \end{aligned}$$

5.4.2. Experimental testbed. — Our experimental testbed is designed to illustrate the relevance of exploiting the potential field nature

of the magnetic field observed in usual buildings. So far, this (simple) testbed only permits one dimensional movements in a vertical plane. The magnetic field is unknown and has 3-dimensional variations. This enables us to precisely measure displacements.

An inertial measurement unit is fixed on a trolley which can roll along a 2.5 m wood rail. No a priori information about this motion was taken into account. We use equally valued parameters for the x and z axis in the covariance matrices P_e and Q . The (3DMGX1 from Microstrain®) IMU provides measurements at a 75 Hz rate. The experiment has been used in different rooms in our building. Observed results are very similar.

Tests are conducted as follows. We push (in no particular way) the trolley along the rail from one displacement mark to the next one. This way, we do 3 go-stop-back and then let the IMU to rest. First, we place our test bed outdoor in a non magnetic-perturbed area. It is easily verified that our filter gives similar results wether the gradient of the magnetic field was used or not (i.e. omitting equations (44) and (45) or not). Then, we move our test bed inside a building. For sake of illustration, we also try another experiment by using a 15 degrees inclination for the rail. There is no noticeable difference in the observation accuracy.

Finally, it is important to mention that when using our test bed, we restrict ourselves to a 2-D problem by zeroing the velocity along the y -axis by assuming $\dot{y} = v = 0$ and $p = r = 0$. A complete three-dimensional experiment is currently in development.

5.4.3. Experimental results. — For each conducted experiment, we present speed and position estimates histories. The z -axis of our sensor is pointing down, perpendicular to the rail, the x -axis is aligned with the rail. (blue plots refer to the z -axis, red ones refer to the x -axis). A unique set of tuning parameters is used throughout the tests. We give a position reference in black.

5.4.3.1. Outdoor experiment. — We choose a non magnetic perturbed area. Due to the lack of magnetic disturbances there is no significant improvement over a classic IMU Kalman filter. Figure 5.5 and Figure 5.6 present the obtained results. The position errors diverge over time. Without magnetic disturbances, the filter can not get rid of errors in velocities.

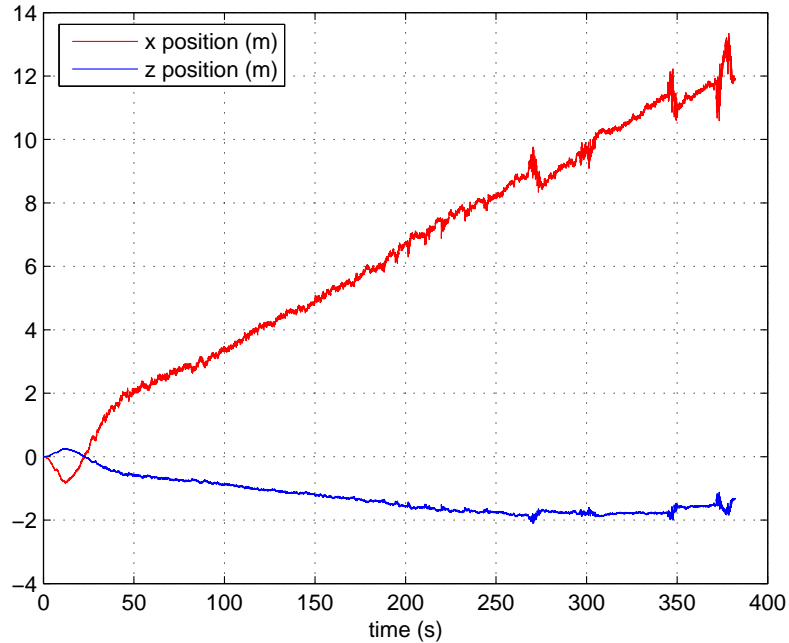


FIGURE 5.5. When no magnetic disturbances are present, the position estimates (slowly) diverge over time.

The situation is very different indoors, as will be demonstrated next. Interestingly, it can be noted that magnetic perturbations bring sufficient information when the experiment is located within a 5 m disc around a light-pole.

5.4.3.2. Indoor horizontal experiment. — First, a short distance displacement is performed. As can be seen in Figure 5.7, the (non overshooting) ramps transients are well estimated as long as they are reasonably fast. When the transients are too quick, position bias and overshoots appear. The actual accelerations are in fact way out of the range of expected values (which standard deviation was defined as $0.5 \text{ m}\cdot\text{s}^{-2}$). In both cases, the velocities are well estimated. Asymptotically, these estimates remain close to zero, which could not be achieved without taking advantage of the magnetic disturbances (one can compare Figure 5.8 and Figure 5.6). Precise measurements on our experiment reveal that

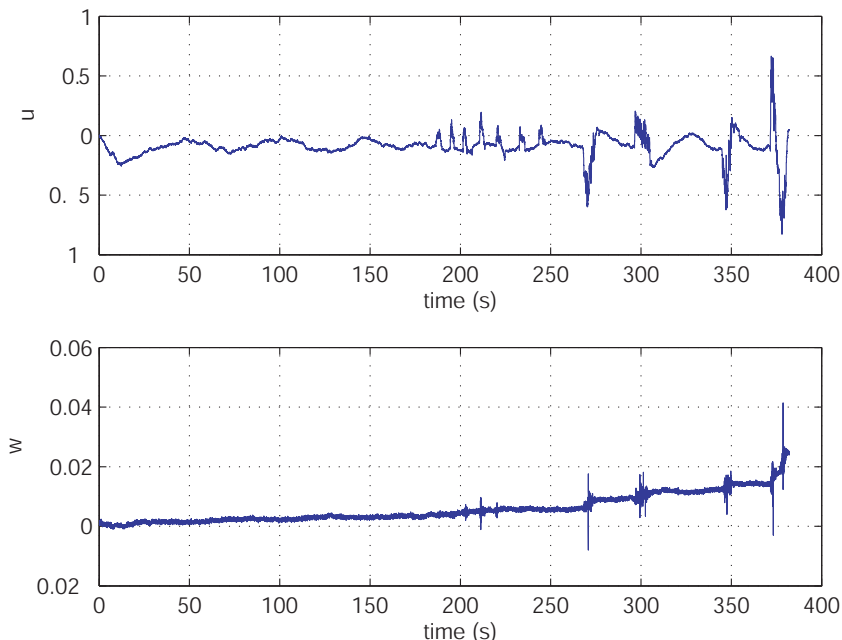


FIGURE 5.6. When no magnetic disturbances are present, the velocities estimates do not remain close to zero. This is a major problem for position estimation.

the position error is below 5 cm over 150 s of tests.

5.4.3.3. Indoor long time horizontal experiment. — A standard benchmark for IMU consists in measuring long-term errors during quasi-static transients. Such an experiment stresses the quality of low-frequency noises rejection. It is critical because of the already discussed integration process. We performed a 30 minutes experiment corresponding to a 2 m displacement. Results are summarized in Figure 5.9. Noticeably, the observed 90 cm position error is very low. This experiment was also used to derive the magnetic field gradient estimates presented in Figure 5.4. Velocities estimates reported in Figure 5.10 have a not surprisingly low mean value of $3e - 5\text{ms}^{-1}$.

5.4.3.4. Indoor 15 deg experiment. — The experimental test bed was oriented to be pointing down with an angle of 15 deg. Thanks to this, we

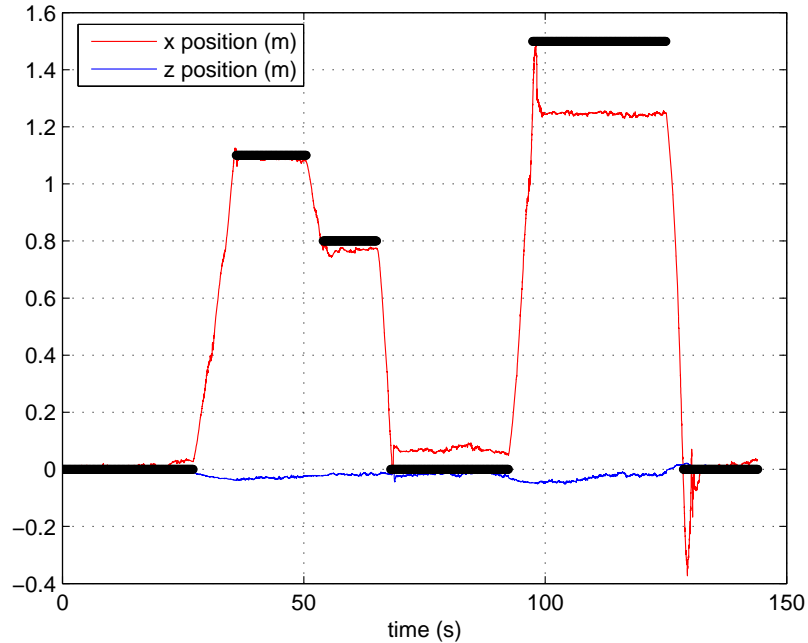


FIGURE 5.7. Short range displacements. Position along the horizontal rail estimate is reported. A bias appears when the transients become too fast.

could also get information from the gradient of the magnetic field with respect to the z -direction. Progressively, we moved the IMU forward by 1.8 m (two 30 cm steps followed by three 15 cm steps, a 30 cm step and eventually one 15 cm step and one 30 cm step). Then we moved it back at the starting point and performed two large steps (1.5 m forward and back). One can easily recognize this motion in Figure 5.11. Again velocities, reported in Figure 5.12, remain close to zero when the IMU is at rest.

5.5. Gain in observability

We wish to underline what information can be derived using Equation (44). Let us consider the system obtained by linearizing the dynamics (Equations (42), (44), and (45)), and evaluate Equation (39).

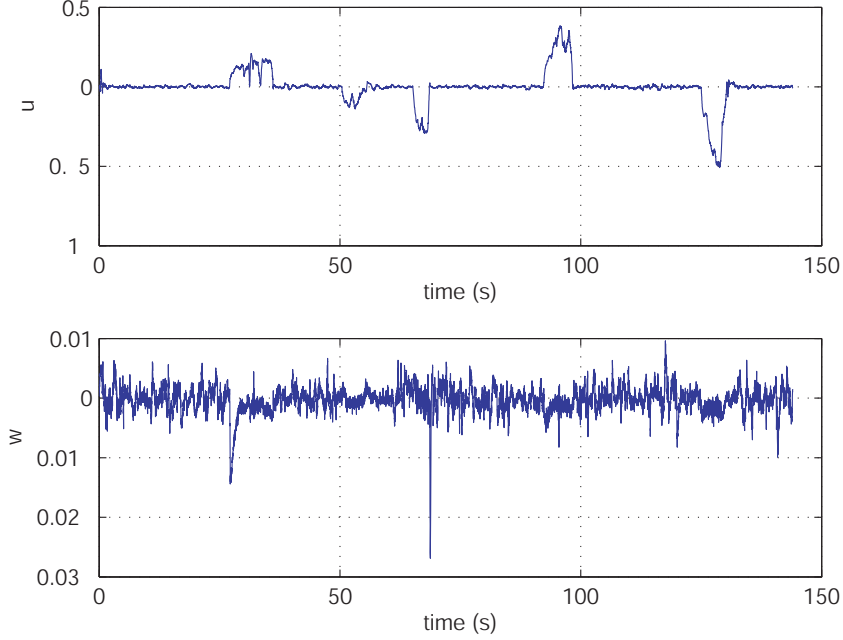


FIGURE 5.8. Short range displacements. Velocities estimates are reported. At rest, they remain close to zero.

To establish the proof of observability gain we consider the system obtained by linearizing the dynamics and measurement equations, in the case where no physical properties are accounted for. We denote by $\partial_X f$ the partial derivative of f with respect to X $\partial_X f = \frac{\partial f}{\partial x}$. According to the general equation of motion (42)

$$\left\{ \begin{array}{l} A_{XV} = \partial_V \dot{X} \quad A_{XQ} = \partial_Q \dot{X} \\ A_{VV} = \partial_V \dot{V} \quad A_{V\Omega} = \partial_\Omega \dot{V} \quad A_{VF} = \partial_F \dot{V} \\ A_{QQ} = \partial_Q \dot{Q} \quad A_{Q\Omega} = \partial_\Omega \dot{Q} \\ A_{\Gamma\Omega} = \partial_\Gamma \dot{\Omega} \\ A_{FF} = \partial_F \dot{F} \\ A_{\Gamma\Gamma} = \partial_\Gamma \dot{\Gamma} \\ A_{MV} = \partial_V \dot{M} \quad A_{MQ} = \partial_Q \dot{M} \quad A_{M\Omega} = \partial_\Omega \dot{M} \\ A_{MM} = \partial_M \dot{M} \quad A_{MH} = \partial_H \dot{M} \\ A_{HH} = \partial_H \dot{H} \end{array} \right.$$

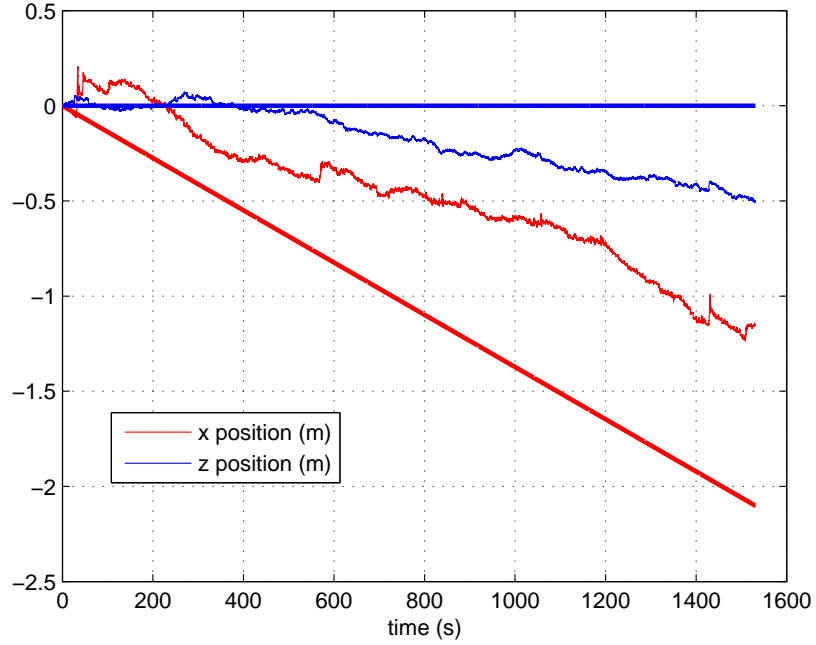


FIGURE 5.9. Long-term low distance displacement. Reference positions are straight lines. Position estimates feature a low long-term error.

with

$$A_{XV} = R$$

$$A_{MV} = R\nabla^2 h R^T$$

$$A_{VF} = A_{Q\Omega} = A_{\Gamma\Omega} = I_3$$

$$A_{VV} = A_{MM} = \begin{bmatrix} 0 & r & -q \\ -r & 0 & p \\ q & -p & 0 \end{bmatrix}$$

$$A_{V\Omega} = \begin{bmatrix} 0 & -w & v \\ w & 0 & -u \\ -v & u & 0 \end{bmatrix}$$

$$A_{M\Omega} = \begin{bmatrix} 0 & -M_z & M_y \\ M_z & 0 & -M_x \\ -M_y & M_x & 0 \end{bmatrix}$$

$$\text{rank}(A_{MV}) = \text{rank}(A_{QW}) = 3$$

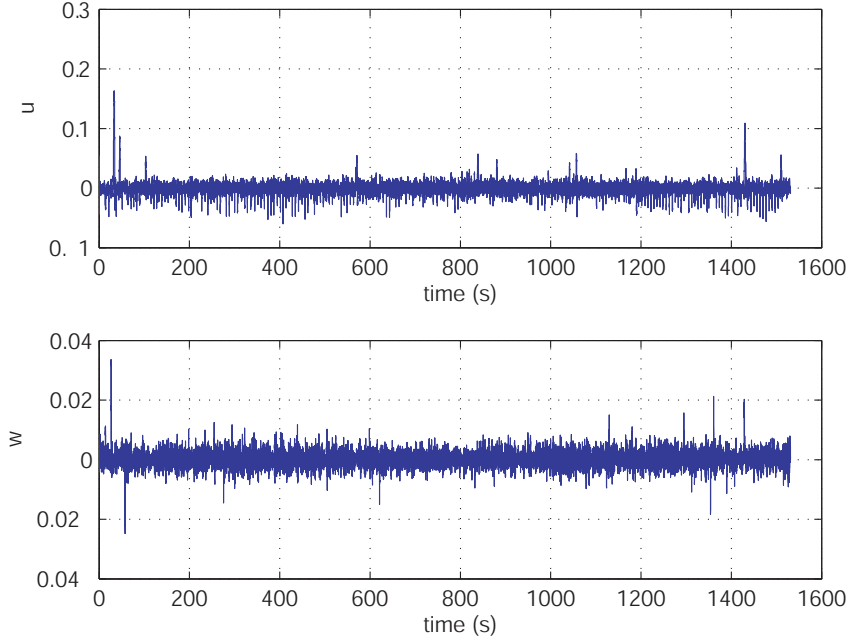


FIGURE 5.10. Long-term low distance displacement. Velocities estimates.

and

$$\begin{aligned} A_{FF} &= -\tau_F^{-1} I_3 \\ A_{\Gamma\Gamma} &= -\tau_\Gamma^{-1} I_3 \\ A_{HH} &= -\tau_H^{-1} I_5 \end{aligned}$$

According to the general equation of measurement (39)

$$\begin{cases} C_{VQ} = \partial_Q Y_V & C_{VF} = \partial_F Y_V \\ C_{\Omega\Omega} = \partial_\Omega Y_\Omega \\ C_{MM} = \partial_M Y_M \end{cases}$$

with $C_{VF} = C_{\Omega\Omega} = C_{MM} = I_3$.

5.5.1. Ignoring the properties of the magnetic field. — When the properties of the magnetic field are ignored, a linear system $\frac{d}{dt}\Delta X =$

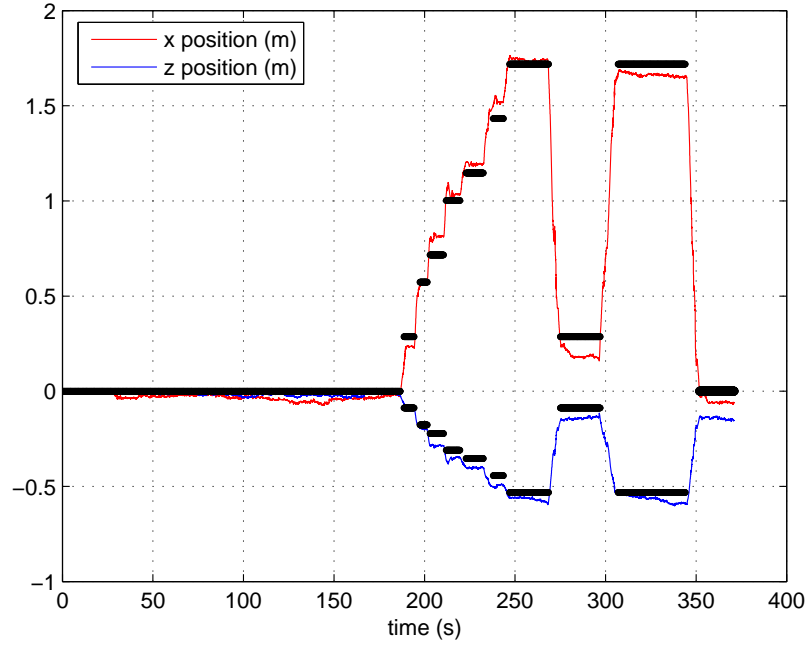


FIGURE 5.11. Succession of steps when the experimental testbed is pointing down with a 15 deg angle. Position estimates.

$A\Delta X$, $\Delta Y = C\Delta X$ is obtained. Matrices A and C are, respectively,

$$A = \begin{bmatrix} 0 & A_{XV} & A_{XQ} & 0 & 0 & 0 \\ 0 & A_{VV} & 0 & A_{V\Omega} & A_{VF} & 0 \\ 0 & 0 & A_{QQ} & A_{Q\Omega} & 0 & 0 \\ 0 & 0 & 0 & 0 & 0 & A_{\Omega\Gamma} \\ 0 & 0 & 0 & 0 & A_{FF} & 0 \\ 0 & 0 & 0 & 0 & 0 & A_{\Gamma\Gamma} \end{bmatrix}$$

$$C = \begin{bmatrix} 0 & 0 & C_{VQ} & 0 & C_{VF} & 0 \\ 0 & 0 & 0 & C_{\Omega\Omega} & 0 & 0 \end{bmatrix}$$

$$\mathcal{O} = [C \quad CA \quad CA^2 \dots CA^{17}]^T$$

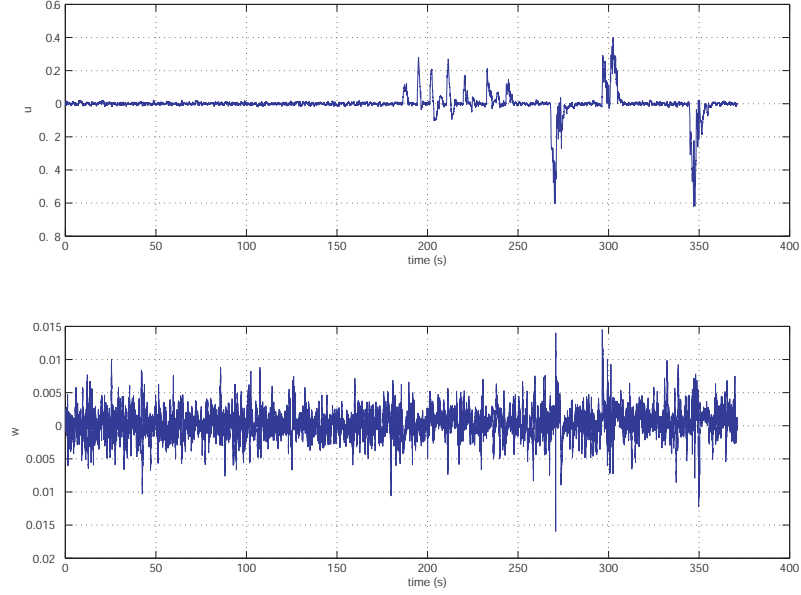


FIGURE 5.12. Succession of steps when the experimental testbed is pointing down with a 15 deg angle. Velocities estimates.

$$(46) \quad A = \begin{bmatrix} 0 & A_{XV} & A_{XQ} & 0 & 0 & 0 & 0 & 0 \\ 0 & A_{VV} & 0 & A_{V\Omega} & A_{VF} & 0 & 0 & 0 \\ 0 & 0 & A_{QQ} & A_{Q\Omega} & 0 & 0 & 0 & 0 \\ 0 & 0 & 0 & 0 & 0 & A_{\Omega\Gamma} & 0 & 0 \\ 0 & 0 & 0 & 0 & A_{FF} & 0 & 0 & 0 \\ 0 & 0 & 0 & 0 & 0 & A_{\Gamma\Gamma} & 0 & 0 \\ 0 & A_{MV} & A_{MQ} & A_{M\Omega} & 0 & 0 & A_{MM} & A_{MH} \\ 0 & 0 & 0 & 0 & 0 & 0 & 0 & A_{HH} \end{bmatrix}$$

$$(47) \quad C = \begin{bmatrix} 0 & 0 & C_{VQ} & 0 & C_{VF} & 0 & 0 & 0 \\ 0 & 0 & 0 & C_{\Omega\Omega} & 0 & 0 & 0 & 0 \\ 0 & 0 & 0 & 0 & 0 & 0 & C_{MM} & 0 \end{bmatrix}$$

When computing the observability matrix \mathcal{O} , one easily realizes that the first two columns are equal to zero. The positions and velocities are not observable.

The rank of O is equal to $rank(C_{VQ}) + rank(C_{VF}A_{FF}) + rank(C_{\Omega\Omega}) + rank(C_{\Omega\Omega}A_{\Omega\Gamma}) = 11$.

5.5.2. Taking the properties of the magnetic field into account.

— If we account for the discussed three properties of the magnetic field, and extend the state as previously presented, we obtain a linear system with A and C matrices given in equations (46) and (47). When computing the observability matrix $O = [C \ CA \ CA^2 \dots \ CA^{25}]^T$, one can easily realize that only the first column is equal to zero (due to the term A_{MV} which corresponds to the partial derivative of the magnetic fields with respect to the velocity V). The rank of O is equal to

$$\begin{aligned} rank(O) &= rank(C_{MM}A_{MV}) + \max(rank(A_{MQ}), rank(C_{VQ})) \\ &\dots + rank(C_{\Omega\Omega}) + rank(C_{VF}) + rank(C_{\Omega\Omega}A_{\Omega\Gamma}) + rank(C_{MM}) \\ &\dots + rank(A_{MH}) = 18 + \max(rank(A_{MQ}), rank(C_{VQ})) \geq 20 \end{aligned}$$

We believe that further investigations of the sub-blocks A_{MQ} , and C_{VQ} would reveal that the rank is actually 21. The defect in observability is now of $6 = 26 - 20$ which is lower than the previously obtained value of $7 = 18 - 11$. It is due to the impact of the velocity onto the magnetic field, as previously stressed. Inspecting the observability matrix O , one can also note that H can only appear in the successive derivatives of the measurements under the form of the matrix product $A_{MH}H$. This vector is of dimension 3 instead of the original 5 dimensional vector H . Two unobservable modes are in fact taking their origin in this rank loss. This indirectly shows that from the original 12 configuration variables, at most 4 linear combinations are lost. Due to the role of velocities in the magnetic field, we believe that, this gain of observability rank primarily focus on velocities variables. A substantially positive impact on the velocity estimation error can be observed.

CHAPTER 6

DIRECT MEASUREMENT OF MAGNETIC-FIELD GRADIENTS FOR NAVIGATION

Dans ce chapitre, nous utilisons, comme au chapitre précédent, l'équation de Maxwell gouvernant le champ magnétique. Cette fois, on utilise une mesure directe des gradients du champs (obtenus par un dispositif spécifique que nous avons construit) pour obtenir des informations de vitesses.

In this chapter, we focus again on Maxwell's equations, but this time, we propose a specific device to directly measure magnetic-field gradients. This yields direct information about the velocity.

6.1. Introduction

This chapter is organized as follows. In Section 6.2, we define the position estimation problem. In Section 6.3, we describe our use of magnetic disturbances and of sensors. In particular, we prove the observability of the velocity in the case considered here. In Section 6.4, we present experimental results, discuss implementation details, and comment on calibration issues.



FIGURE 6.1. A typical platoon of soldiers in action as envisioned in the BOA projet. ©F. Blanchard-BD Médias for Délégation Générale pour l'Armement (DGA). A team leader keeps track of his soldiers thanks to real-time position information reported on his arm held display.

6.2. Measuring magnetic fields gradients to derive velocity

Using the same notations as in Chapter 5, in the body frame, one can differentiate (43) to get the following differential equation (thanks to a chain rule)

$$(48) \quad \dot{M} = -\Omega \times M + R\nabla^2 h R^T V$$

In the previous Chapter, we considered this equation by assuming that $\nabla^2 h$ was unknown, and modeled its components by first order dynamics driven by white noises ν_H . We extended the state by adding the magnetic field M and the independent gradients H . Due to the three properties presented above, there are only five independent gradients to

reconstruct. These are, in the inertial frame:

$$H \triangleq [h_{xx} \quad h_{xy} \quad h_{xz} \quad h_{yy} \quad h_{yz}]^T \in \mathbb{R}^5$$

Some experiments have shown that strongly varying magnetic fields are difficult to estimate using this approach.

In this Chapter, we use a set of magnetometers to evaluate $\nabla^2 h$. Three 3-axis magnetometers are precisely mounted on a board, see Figure 6.2. The exact locations are defined by vector lever arms $l1$, $l2$, and $l3$ which define a direct orthogonal trihedron. The sought after variables H are obtained from finite difference schemes. Further, we model their dynamics by a white noise

$$(49) \quad \dot{H} = \nu_H$$

Slopes depicted in Figure 5.3 suggest that spatial derivatives of H are not negligible. For sake of performance, it is recommended to include some higher order dynamics in both measurement and dynamics equations. For sake of simplicity, we do not present them here, but they can be easily taken into account.

Under the preceding assumptions, the vector of measurement obtained from the IMU, and the orthogonal trihedron of magnetometers is modeled as

$$(50) \quad \begin{cases} Y_V = F - Rg + B_V + \mu_V \\ Y_\Omega = \Omega + B_\Omega + \mu_\Omega \\ Y_{M_0} = M + \mu_{M_0} \\ Y_{M_1} = M + R\nabla^2 h R^T l1 + \mu_{M_1} \\ Y_{M_2} = M + R\nabla^2 h R^T l2 + \mu_{M_2} \\ Y_{M_3} = M + R\nabla^2 h R^T l3 + \mu_{M_3} \end{cases}$$

As will now appear, Equation (44) plays a key role in this observation problem. It is the only one giving direct information on V .

6.3. Gain of observability

6.3.1. Linearization. — In a general approach, let us consider the system obtained by linearizing the dynamics (42)-(48)-(49), and the measurement Equation (50). We denote by $\partial_X f$ the partial derivative of f with respect to X , $\partial_X f = \frac{\partial f}{\partial x}$.

From Equations (42)-(48)-(49), we obtain

$$\left\{ \begin{array}{l} A_{XV} = \partial_V \dot{X}, \quad A_{XQ} = \partial_Q \dot{X} \\ A_{VV} = \partial_V \dot{V}, \quad A_{V\Omega} = \partial_\Omega \dot{V}, \quad A_{VF} = \partial_F \dot{V} \\ A_{QQ} = \partial_Q \dot{Q}, \quad A_{Q\Omega} = \partial_\Omega \dot{Q} \\ A_{FF} = 0 \\ A_{\Gamma\Gamma} = 0 \\ A_{MV} = \partial_V \dot{M}, \quad A_{MQ} = \partial_Q \dot{M}, \quad A_{M\Omega} = \partial_\Omega \dot{M} \\ A_{MM} = \partial_M \dot{M}, \quad A_{MH} = \partial_H \dot{M} \\ A_{HH} = 0 \end{array} \right.$$

with

$$A_{XV} = R^T$$

$$A_{MV} = R\nabla^2 h R^T$$

$$A_{VF} = A_{Q\Omega} = A_{\Gamma\Omega} = I_3$$

$$A_{VV} = A_{MM} = \begin{bmatrix} 0 & r & -q \\ -r & 0 & p \\ q & -p & 0 \end{bmatrix}$$

$$A_{V\Omega} = \begin{bmatrix} 0 & -w & v \\ w & 0 & -u \\ -v & u & 0 \end{bmatrix}$$

$$A_{M\Omega} = \begin{bmatrix} 0 & -M_z & M_y \\ M_z & 0 & -M_x \\ -M_y & M_x & 0 \end{bmatrix}$$

$$A_{Q\Omega} = \begin{bmatrix} 1 & \sin(\phi) \tan(\theta) & \cos(\phi) \tan(\theta) \\ 0 & \cos(\phi) & -\sin(\phi) \\ 0 & \frac{\sin(\phi)}{\cos(\theta)} & \frac{\cos(\phi)}{\cos(\theta)} \end{bmatrix}$$

and

$$A_{QQ} = \begin{bmatrix} \frac{(qc\phi - rs\phi)s\theta}{c\theta} & \frac{qs\phi + rc\phi}{c\theta^2} & 0 \\ -qs\phi - rc\phi & 0 & 0 \\ \frac{qc\phi - rs\phi}{c\theta} & \frac{(qs\phi + rc\phi)c\theta}{\tan(\theta)} & 0 \end{bmatrix}$$

From Equation (50), we derive

$$\left\{ \begin{array}{l} C_{VQ} = \partial_Q Y_V, \quad C_{VF} = \partial_F Y_V \\ C_{\Omega\Omega} = \partial_\Omega Y_\Omega \\ C_{M_0M} = \partial_M Y_{M_0} \\ C_{M_1M} = \partial_M Y_{M_1}, \quad C_{M_1Q} = \partial_Q Y_{M_1}, \quad C_{M_1H} = \partial_H Y_{M_1} \\ C_{M_2M} = \partial_M Y_{M_2}, \quad C_{M_2Q} = \partial_Q Y_{M_2}, \quad C_{M_2H} = \partial_H Y_{M_2} \\ C_{M_3M} = \partial_M Y_{M_3}, \quad C_{M_3Q} = \partial_Q Y_{M_3}, \quad C_{M_3H} = \partial_H Y_{M_3} \end{array} \right.$$

with $C_{VF} = C_{\Omega\Omega} = C_{M_0M} = C_{M_1M} = C_{M_2M} = C_{M_3M} = I_3$.

One can easily realize that the position X is not observable (it does not appear anywhere in the right-hand side of the dynamics). We now focus on the reduced state $[V; Q; \Omega; F; M; H]^T$.

6.3.2. Ignoring the properties of the magnetic field. — When the properties of the magnetic field are ignored, a linear system $\dot{\Sigma} = A\Sigma$, $\Delta Y = C\Sigma$ is obtained from the preceding linearization. The state vector is $[V; Q; \Omega; F]^T \in \mathbb{R}^{12}$. Matrices A and C are, respectively,

$$A = \begin{bmatrix} A_{VV} & 0 & A_{V\Omega} & A_{VF} \\ 0 & A_{QQ} & A_{Q\Omega} & 0 \\ 0 & 0 & 0 & 0 \\ 0 & 0 & 0 & 0 \end{bmatrix}$$

$$C = \begin{bmatrix} 0 & C_{VQ} & 0 & C_{VF} \\ 0 & 0 & C_{\Omega\Omega} & 0 \end{bmatrix}$$

$$\mathcal{O} = [C; CA; CA^2; \dots; CA^{11}]$$

When computing the observability matrix \mathcal{O} , one easily realizes that its first column is identically equal to zero. In fact, the rank of \mathcal{O} is

$$\text{rank}[\mathcal{O}] = \text{rank}[C_{VQ}A_{QQ}] + \text{rank}[C_{VF}] + \text{rank}[C_{\Omega\Omega}] = 8$$

When ignoring the properties of the magnetic field, it appears that V and ψ are not observable. Using only gyroscopes and accelerometers, only ϕ , θ , Ω , and F can be observed.

6.3.3. Accounting for the properties of the magnetic field. —

In this setup, we consider the full state $[V; Q; \Omega; F, M, H]^T \in \mathbb{R}^{20}$. We obtain another linear system $\dot{\Sigma} = A\Sigma$, $\Delta Y = C\Sigma$ with

$$A = \begin{bmatrix} A_{VV} & 0 & A_{V\Omega} & A_{VF} & 0 & 0 \\ 0 & A_{QQ} & A_{Q\Omega} & 0 & 0 & 0 \\ 0 & 0 & 0 & 0 & 0 & 0 \\ 0 & 0 & 0 & 0 & 0 & 0 \\ A_{MV} & A_{MQ} & A_{M\Omega} & 0 & A_{MM} & A_{MH} \\ 0 & 0 & 0 & 0 & 0 & 0 \end{bmatrix}$$

$$C = \begin{bmatrix} 0 & C_{VQ} & 0 & C_{VF} & 0 & 0 \\ 0 & 0 & C_{\Omega\Omega} & 0 & 0 & 0 \\ 0 & 0 & 0 & 0 & C_{MM} & 0 \\ 0 & C_{M_1Q} & 0 & 0 & C_{MM} & C_{M_1H} \\ 0 & C_{M_2Q} & 0 & 0 & C_{MM} & C_{M_2H} \\ 0 & C_{M_3Q} & 0 & 0 & C_{MM} & C_{M_3H} \end{bmatrix}$$

$$\mathcal{O} = [C; CA; CA^2; \dots; CA^{19};]$$

The observability matrix is \mathcal{O} . In its first column, a term appears, namely A_{MV} (which corresponds to the partial derivative of the magnetic fields with respect to the velocity V). In details,

$$\begin{aligned} \text{rank}[\mathcal{O}] \geq & \text{rank}[A_{MV}] + \text{rank} \begin{bmatrix} C_{VQ} \\ A_{MQ} \end{bmatrix} + \text{rank}[C_{\Omega\Omega}] \\ & + \text{rank}[A_{MV}A_{VF}] + \text{rank}[C_{MM}] + \text{rank} \begin{bmatrix} C_{M_1H} \\ C_{M_2H} \\ C_{M_3H} \end{bmatrix} \end{aligned}$$

As proven later on, \mathcal{O} is full rank (20) under the following conditions:

- $|\theta| < \frac{\pi}{2}$
- $\nabla^2 h$ is invertible
- $\nabla^2 h$ is not of the diagonal form $\text{diag}(a, a, -2a)$, $a \in \mathbb{R}$ and at least one of the first two components of $R_\theta^T R_\phi^T V$ is non zero.

If the last condition is not satisfied, then $\text{rank}(\mathcal{O}) = 19$ and the non observable state is ψ . It is possible to get some physical insight into these conditions: the first two components of $R_\theta^T R_\phi^T V$ correspond (up to a R_ψ rotation) to the coordinates of the velocity vector in the inertial frame (x, y) -plane. At least, one of these has to be non zero, so that ψ can be recovered. Also, if the $\nabla^2 h$ is of the mentioned diagonal form, then the magnetic disturbances are insufficient to recover the heading variable.

6.3.4. Observability. — We wish to compute the observability matrix $\mathcal{O} = [C; CA; \dots; CA^{19}]$ with C and A defined in Section 6.4. \mathcal{O} is given in the following equation. Bold elements (in brackets) play a key role in the rank computation.

$$\mathcal{O} = \begin{bmatrix}
0 & [\mathbf{Cvq}] & 0 & C_{VF} & 0 & 0 \\
0 & 0 & [\mathbf{C}\Omega\Omega] & 0 & 0 & 0 \\
0 & 0 & 0 & 0 & [\mathbf{C}_{MM}] & 0 \\
0 & C_{M_1Q} & 0 & 0 & C_{MM} & [\mathbf{C}_{M_1H}] \\
0 & C_{M_2Q} & 0 & 0 & C_{MM} & [\mathbf{C}_{M_2H}] \\
0 & C_{M_3Q} & 0 & 0 & C_{MM} & [\mathbf{C}_{M_3H}] \\
0 & C_{VQ}A_{QQ} & C_{VQ}A_{Q\Omega} & 0 & 0 & 0 \\
0 & 0 & 0 & 0 & 0 & 0 \\
A_{MV} & [\mathbf{A}Mq] & A_{M\Omega} & 0 & A_{MM} & A_{MH} \\
[\mathbf{A}MV] & C_{M_1Q}A_{QQ} + A_{MQ} & C_{M_1Q}A_{Q\Omega} + A_{M\Omega} & 0 & A_{MM} & A_{MH} \\
A_{MV} & C_{M_2Q}A_{QQ} + A_{MQ} & C_{M_2Q}A_{Q\Omega} + A_{M\Omega} & 0 & A_{MM} & A_{MH} \\
A_{MV} & C_{M_3Q}A_{QQ} + A_{MQ} & C_{M_3Q}A_{Q\Omega} + A_{M\Omega} & 0 & A_{MM} & A_{MH} \\
0 & * & * & 0 & * & * \\
0 & * & * & 0 & * & * \\
* & * & * & [\mathbf{A}MV\mathbf{A}VF] & * & *
\end{bmatrix}$$

We have seen that

$$\begin{aligned} \text{rank}[\mathcal{O}] &= \text{rank}[A_{MV}] + \text{rank} \begin{bmatrix} C_{VQ} \\ A_{MQ} \end{bmatrix} + \text{rank}[C_{\Omega\Omega}] \\ &+ \text{rank}[A_{MV}A_{VF}] + \text{rank}[C_{MM}] + \text{rank} \begin{bmatrix} C_{M_1H} \\ C_{M_2H} \\ C_{M_3H} \end{bmatrix} \end{aligned}$$

We now study each of these terms.

First, $\text{rank}[A_{MV}] = 3$, provided that $\nabla^2 h$ is invertible. Then, as is proven in Proposition 5, $\text{rank} \begin{bmatrix} C_{VQ} \\ A_{MQ} \end{bmatrix} = 3$. Simply, $\text{rank}[C_{\Omega\Omega}] = 3$. Provided that $\nabla^2 h$ is invertible, $\text{rank}[A_{MV}A_{VF}] = \text{rank}[A_{MV}] = 3$. Directly, $\text{rank}[C_{MM}] = 3$. And finally, $\text{rank} \begin{bmatrix} C_{M_1H} \\ C_{M_2H} \\ C_{M_3H} \end{bmatrix} = 5$, as is proven in Proposition 4.

Proposition 4. — $\text{rank} \begin{bmatrix} C_{M_1H} \\ C_{M_2H} \\ C_{M_3H} \end{bmatrix} = 5$

Proof. — Let us now consider the measurement Equation (50) for the four magnetometers. We note the lever arm in the inertial frame for each magnetometer j by $l_{j_i} = [l_{j_{xi}} \ l_{j_{yi}} \ l_{j_{zi}}]^T = R^T l_j$. Considering the j^{th} , magnetometer we get

$$\begin{aligned} C_{M_jH} &= \frac{\partial R \nabla^2 h R^T l_j}{\partial H} \\ &= R \frac{\partial}{\partial H} \left(\begin{bmatrix} h_{xx} & h_{xy} & h_{xz} \\ h_{xy} & h_{yy} & h_{yz} \\ h_{xz} & h_{yz} & -(h_{xx} + h_{yy}) \end{bmatrix} \begin{bmatrix} l_{j_{xi}} \\ l_{j_{yi}} \\ l_{j_{zi}} \end{bmatrix} \right) \\ &= R \begin{bmatrix} l_{j_{xi}} & l_{j_{yi}} & l_{j_{zi}} & 0 & 0 \\ 0 & l_{j_{xi}} & 0 & l_{j_{yi}} & l_{j_{zi}} \\ -l_{j_{zi}} & 0 & l_{j_{xi}} & -l_{j_{zi}} & l_{j_{yi}} \end{bmatrix} \end{aligned}$$

Yet, $\text{rank} \begin{bmatrix} C_{M_1H} \\ C_{M_2H} \\ C_{M_3H} \end{bmatrix} = \text{rank} \begin{bmatrix} R^T C_{M_1H} \\ R^T C_{M_2H} \\ R^T C_{M_3H} \end{bmatrix}$. This last matrix is, in fact,

$$\begin{bmatrix} R^T C_{M_1H} \\ R^T C_{M_2H} \\ R^T C_{M_3H} \end{bmatrix} = \begin{bmatrix} \mathbf{l1}_{xi} & \mathbf{l1}_{yi} & \mathbf{l1}_{zi} & 0 & 0 \\ 0 & l1_{xi} & 0 & \mathbf{l1}_{yi} & \mathbf{l1}_{zi} \\ -l1_{zi} & 0 & l1_{xi} & -\mathbf{l1}_{zi} & \mathbf{l1}_{yi} \\ \mathbf{l2}_{xi} & \mathbf{l2}_{yi} & \mathbf{l2}_{zi} & 0 & 0 \\ 0 & l2_{xi} & 0 & \mathbf{l2}_{yi} & \mathbf{l2}_{zi} \\ -l2_{zi} & 0 & l2_{xi} & -\mathbf{l2}_{zi} & \mathbf{l2}_{yi} \\ \mathbf{l3}_{xi} & \mathbf{l3}_{yi} & \mathbf{l3}_{zi} & 0 & 0 \\ 0 & l3_{xi} & 0 & \mathbf{l3}_{yi} & \mathbf{l3}_{zi} \\ -l3_{zi} & 0 & l3_{xi} & -\mathbf{l3}_{zi} & \mathbf{l3}_{yi} \end{bmatrix}$$

The bold elements in the three first columns correspond to $(R^T[l1l2l3])^T$ which is of rank 3, then the rank of the lines 1, 4 and 7 is 3. Now let us consider the last two columns. By computing the three 2×2 determinants, we obtain: $l1_{yi}^2 + l1_{zi}^2$ for the first one and $l2_{yi}^2 + l2_{zi}^2$ and $l3_{yi}^2 + l3_{zi}^2$ for the other two. Assuming that these determinants are all zero, the last conditions are exclusive. If the first one holds, then the rotation R is around the x axis. If the second holds, then the rotation R is around the z axis (with an angle of $-\pi/2$). If the third holds, then the rotation R is around the y -axis (with an angle of $\pi/2$). At least, one of the determinants must be non zero. This gives the conclusion. \square

Proposition 5. — Assuming that $|\theta| < \frac{\pi}{2}$, $\text{rank} \begin{bmatrix} C_{VQ} \\ A_{MQ} \end{bmatrix} \geq 2$. Sufficient conditions for $\text{rank} \begin{bmatrix} C_{VQ} \\ A_{MQ} \end{bmatrix} = 3$ are that, at least one of the first two components of $R_\theta^T R_\phi^T V$ is non zero and that $\nabla^2 h$ is not of the form $\text{diag}(a, a, -2a)$, $a \in \mathbb{R}$.

Proof. — By definition,

$$\begin{aligned} C_{VQ} &= \frac{\partial}{\partial Q}(-Rg) \\ &= g \begin{bmatrix} 0 & -\cos(\theta) & 0 \\ \cos(\theta)\cos(\phi) & -\sin(\theta)\sin(\phi) & 0 \\ -\sin(\phi)\cos(\theta) & -\sin(\theta)\cos(\phi) & 0 \end{bmatrix} \end{aligned}$$

which always satisfy, provided $|\theta| < \frac{\pi}{2}$, $\text{rank}(C_{VQ}) = 2$.

The possible extra rank may come from the third column $A_{M\psi} = \frac{\partial M}{\partial \psi}$ of A_{MQ}

$$\begin{aligned} A_{M\psi} &= \frac{\partial}{\partial \psi}(R\nabla^2 h R^T V) \\ &= \frac{\partial}{\partial \psi}(R_\phi R_\theta R_\psi \nabla^2 h R_\psi^T R_\theta^T R_\phi^T V) \\ &= R_\phi R_\theta \frac{\partial}{\partial \psi}(R_\psi \nabla^2 h R_\psi^T R_\theta^T R_\phi^T V) \end{aligned}$$

Note $R_\theta^T R_\phi^T V = \tilde{V}$, it follows that

$$\begin{aligned} &\left\{ \frac{\partial}{\partial \psi}(R_\psi \nabla^2 h R_{-\psi} \tilde{V}) = 0 \right\} \\ &\Rightarrow \left\{ \forall (\psi_1, \psi_2) \in \mathcal{R}^2, R_{\psi_1} \nabla^2 h R_{\psi_1}^T \tilde{V} = R_{\psi_2} \nabla^2 h R_{\psi_2}^T \tilde{V} \right\} \end{aligned}$$

By evaluating these last conditions for particular points: $(\psi_1 = \frac{\pi}{2}, \psi_2 = 0)$, $(\psi_1 = -\frac{\pi}{2}, \psi_2 = 0)$ and $(\psi_1 = \pi, \psi_2 = 0)$, we obtain, after some calculus, that $\frac{\partial}{\partial \psi}(R_\psi \nabla^2 h R_{-\psi} \tilde{V}) = 0$ implies that either: $(\tilde{u}, \tilde{v}) = (0, 0)$ or $\nabla^2 h$ is of the form $\text{diag}(a, a, -2a)$, $a \in \mathbb{R}$.

Conversely, if this condition fails, then $\frac{\partial}{\partial \psi}(R_\psi \nabla^2 h R_{-\psi} \tilde{V}) \neq 0$ which concludes the proof. □

6.4. Filter design and experimental results

Thanks to the discussed observability property of the system (42)-(48)-(49)-(50), we implemented an extended Kalman filter (EKF) to reconstruct the state $[V, Q, \Omega, F, M, H]^T \in \mathbb{R}^{20}$, and, eventually, use it to estimate the position $X \in \mathbb{R}^3$.

6.4.1. Filter design. — In practice, the state of our EKF is composed of 45 variables including configuration states (12 variables), magnetic field and its independent first and second derivatives (3+5+7 variables), forces and torques (3+3 variables), sensors biases (6 variables). We used equally valued tuning parameters for the 3 axis. These are chosen to capture fast dynamics ($\sigma_{acceleration} = 8 \text{ m.s}^{-2}$, $\sigma_{torque} = 4 \text{ rad.s}^{-2}$). Classically, discrete-time updates are implemented. Updates are synchronized with the 75 Hz measurements from the IMU.

The EKF state X evolves according to the following continuous time model $\dot{X} = F(X, U)$ where U is the input variable.

First, a prediction from time k to $k+1$ is performed, this gives X_p and P_p , and then the EKF estimates the state from the measurements, yielding X_e and P_e . We note T the sampling time, Q and R being the covariances matrix of the zero-mean dynamic and sensors white noises, respectively.

6.4.2. Experimental testing bench and calibration issues. —

6.4.2.1. Testing bench:— Our experimental testing bench is designed to illustrate the relevance of our approach in standard buildings inside which the magnetic field is unknown and has significant 3-dimensional variations. Off the shelves IMUs are used (e.g. a 3DMGX1 from Microstrain®)

Four IMUs are fixed on a board which can simultaneously rotate and translate in 3D. Only one out of the four is actually used as an IMU. The remaining three are used as 3-D magnetometers. This board has been used in different rooms in our building. Obtained results are very similar.

6.4.2.2. Calibration issues. — While the four IMU are supposed to be very similar, experimentally, a serious practical issue is sensors calibration. Even if mechanical tolerances are indeed small, we quickly realized that it was absolutely necessary to determine bias, misalignment angles,

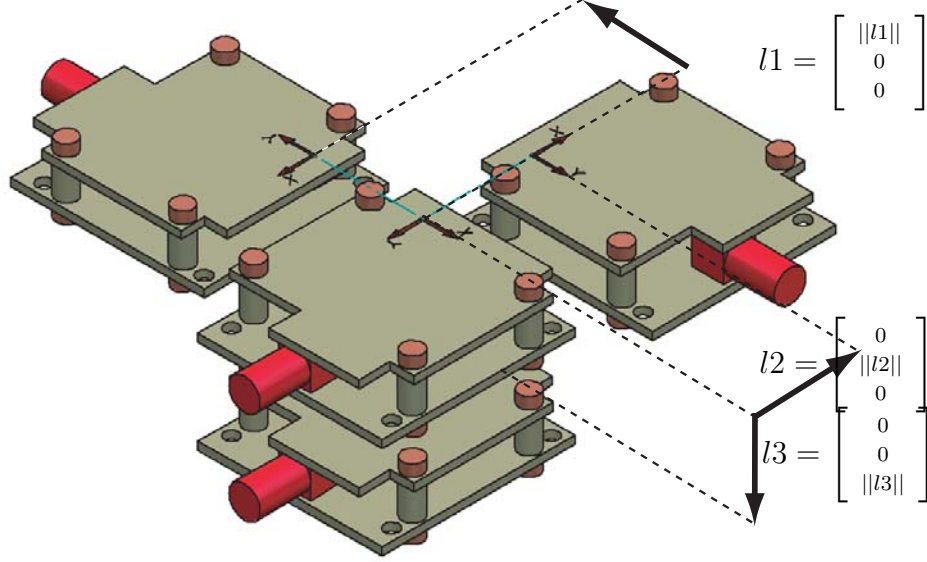


FIGURE 6.2. Experimental testing bench with the four IMU, one giving accelerations, raw data, magnetic field and the three other used as simple external magnetometers

and scale factors for every magnetometer. Each magnetometer measurement is modeled as follows, for j , ($j = 0 \dots 3$),

$$Y_{jm} = \alpha_j R_j Y_j + \beta_j \quad \text{with } \beta = [\beta_{j1} \ \beta_{j2} \ \beta_{j3}]^T$$

$$R_j = \begin{bmatrix} 1 & \psi_j & -\theta_j \\ -\psi_j & 1 & \phi_j \\ \theta_j & -\phi_j & 1 \end{bmatrix} \quad \alpha_j = \begin{bmatrix} \alpha_{j1} \\ \alpha_{j2} \\ \alpha_{j3} \end{bmatrix}$$

The small scale of possible measurements (± 1 G) prevents us from using comparisons with a calibrated induction. Rather, we compute the unknown parameters α_j , β_j and R_j as the minimizers of a least square problem under the constraints that the reconstructed vector

$$(h_{xx}, h_{xy}, h_{xz}, h_{yx}, h_{yy}, h_{yz}, h_{zx}, h_{zy}, h_{zz})$$

must define a symmetric Hessian $\nabla^2 h$ with zero trace. A large number of experimental data was used to define this least-square problem.

6.4.3. Experimental results. — We consider the following normalized experiment. Sequentially, the board is moved forward along a 1 m straight line in 10 cm steps. This motion is accurately measured. No a priori information about the trajectory is given to the filter. Data are transferred to a remote PC and treated off-line. For sake of comparisons, we present position estimation results obtained with three different methods. The first one is presented here, it uses the four magnetometers. The second method was presented in [84]. As already discussed, it uses a single magnetometer. Finally, results obtained with inertial calculations (using only gyroscopes and accelerometers) are presented.

For each conducted experiment, we expose speed and position estimates histories. Blue plots refer to the x-axis, green plots refer to the y-axis and red plots refer to the z-axis.

Ignoring the magnetometers, position estimates diverge over time see Figure 6.3(e). The filter can not get rid of errors in velocities.

Using a single magnetometer, we obtain much better results. This time, velocities, reported in Figure 6.3(c), remain close to zero when the IMU is at rest. This prevents the position estimates from diverging.

Most interestingly, when using the four magnetometers, we improve the accuracy a lot. Results are reported in Figure 6.3(a)(b). Errors in positions fall under ± 2 cm.

6.5. Future directions

In this chapter, we have improved on the results obtained in Chapter 5. By considering, as we did previously, Equation (44), we have reconciled the velocity estimate with the magnetic-field disturbances. In contrast to our original approach, we designed and used an experimental orthogonal trihedron of four magnetometers, which gives, through finite difference schemes, a direct measurement of the spatial partial derivatives of the magnetometer field.

Accurate calibration of the sensors is a key issue that remains to be explored further; it can be improved upon by using second-order centered schemes. The real-time implementation was duplicated using a laptop PC running MATLAB. The computational requirements could be reduced

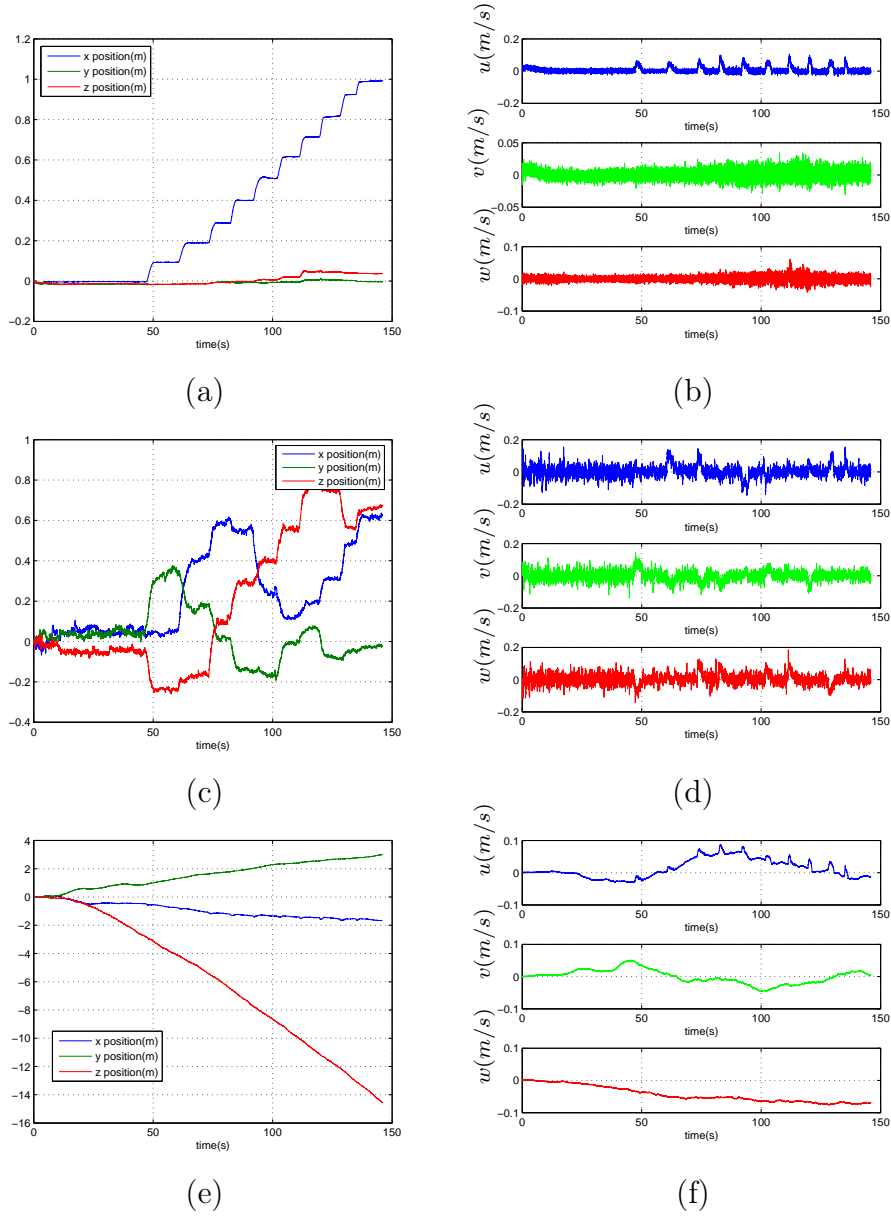


FIGURE 6.3. Succession of steps when the experimental testing bench is horizontal. Three methods are compared. Top: using the presented four magnetometers method. Middle: using a single magnetometer. Bottom: without magnetometer. Position estimates (a),(c),(e). Velocity estimates (b), (d), (f)

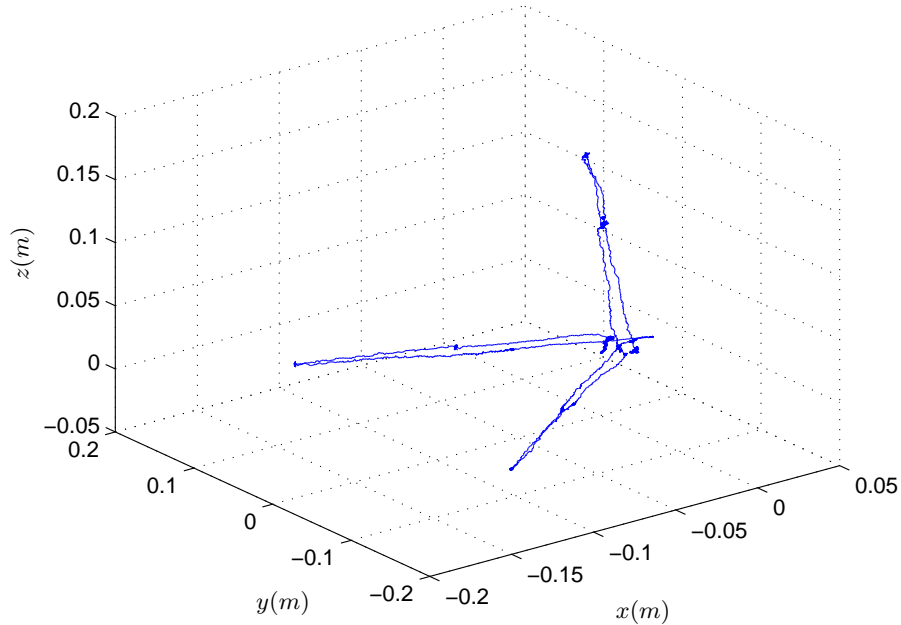


FIGURE 6.4. The body is sequentially moved along the three axis of an orthogonal trihedron, position estimates are reported

by neglecting some non-crucial states in the EKF. We have carried out some experiments, reported in Figure 6.3, to quantitatively compare the improvement over other methods.

Finally, we give some preliminary 3-D experimental results. Measuring the 3-D displacement requires some specific instrumentation that could not be used at the time of writing. Quantifying the accuracy obtained remains to be done, but the results seem promising. In an initial experiment, the rigid body was moved (sequentially) along the three axes of an orthogonal trihedron. This motion is easily recognizable in Figure 6.4. Larger-scale results were obtained by following a loop-shaped corridor in the basement of our laboratory. Results are presented in Figure 6.5. The position error did not exceed 50 cm.

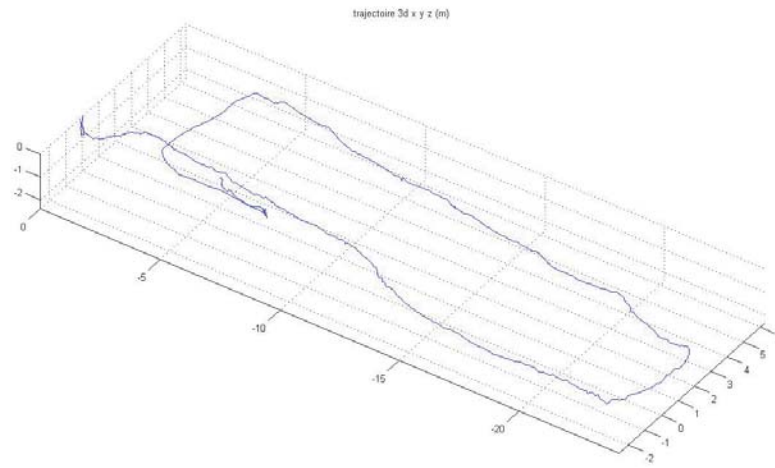


FIGURE 6.5. Walking through a loop shaped corridor. (3D)
Position estimates.

BIBLIOGRAPHY

- [1] P. Abbeel, A. Coates, M. Quigley, and A. Y. Ng. An application of reinforcement learning to aerobatic helicopter flight. *Neural Information Processing Systems (NIPS) 19*, 2007.
- [2] R. Abraham, J. E. Marsden, and T. Ratiu. *Manifolds, Tensor Analysis, and Applications*. Springer, second edition, 1988.
- [3] Federal Aviation Administration. Rotorcraft flying handbook. In *Washington : U.S. Government Printing Office, 2000, 208 p.*, 2000.
- [4] A. P. Aguiar, J. P. Hespanha, and P. Kokotovic. Limits of performance in reference-tracking and path-following for nonlinear systems. In *Proc. of the 16th IFAC World Congress*, 2005.
- [5] A. P. Aguiar, J. P. Hespanha, and P. Kokotovic. Path-following for non-minimum phase systems removes performance limitations. *IEEE Transactions on Automatic Control*, 50(2):234–239, 2005.
- [6] S. A. Al-Hiddabi and N. H. McClamroch. Aggressive longitudinal aircraft trajectory tracking using nonlinear control. *Journal of Guidance, Control, and Dynamics*, 25(1):26–32, 2002.
- [7] S. A. Al-Hiddabi and N. H. McClamroch. Tracking and maneuver regulation control for nonlinear nonminimum phase systems: Application to flight control. *IEEE Transactions on Control Systems Technology*, 10(6):780–792, 2002.

- [8] J. C. Avila-Vilchis, B. Brogliato, A. Dzul, and R. Lozano. Nonlinear modelling and control of helicopters. *Automatica*, 39(9):1583–1596, 2003.
- [9] G. J. Balas. Flight control law design : An industry perspective in fundamental issues in control. In *Special issue of European Journal of Control*, 2003.
- [10] R. Bhattacharya. OPTRAGEN a Matlab toolbox for optimal trajectory generation. User’s manual, Aerospace Engineering Department, Texas A& M University, 2006.
- [11] E. Børhaug, A. Pavlov, and K. Y. Pettersen. *Cross-track formation control of underactuated autonomous underwater vehicles*. Group Coordination and Cooperative Control. Springer Verlag, 2006.
- [12] E. Børhaug and K. Y. Pettersen. Cross-track control for underactuated autonomous vehicles. In *Proc. of the 44th IEEE Conf. on Decision and Control, and the European Control Conference 2005*, 2005.
- [13] E. Børhaug and K. Y. Pettersen. Los path following for underactuated underwater vehicle. In *7th IFAC Conference on Manoeuvring and Control of Marine Craft (MCMC’2006)*, 2006.
- [14] M. Caccamo, Th. Baker, A. Burns, G. Buttazzo, and L. Sha. Real-time scheduling for embedded systems. In D. Hristu-Varsakelis and W. S. Levine, editors, *Handbook of networked and embedded control systems*. Birkhäuser, 2005.
- [15] P. Castillo, A. Dzul, and R. Lozano. Real-time stabilization and tracking of a four rotor mini rotorcraft. *IEEE Trans. Control Systems Technology*, 12(4):510–516, 2004.
- [16] P. Castillo, R. Lozano, and A. E. Dzul. *Modelling and control of mini-flying machines*. Advances in industrial control. Springer, 2005.
- [17] D. E. Chang and J. E. Marsden. Gyroscopic forces and collision avoidance with convex obstacles. *Nonlinear Dynamics and Control*, 295:145–160, 2003.

- [18] D. E. Chang, S. Shadden, J. E. Marsden, and R. Olfati-Saber. Collision avoidance for multiple agent systems. In *Proc. of the 42nd IEEE Conf. on Decision and Control*, 2003.
- [19] S. Changey, D. Beauvois, and V. Fleck. A mixed extended-unscented filter for attitude estimation with magnetometer sensor. In *Proc. of the 2006 American Control Conference*, 2006.
- [20] F. Chaplais and N. Petit. Inversion in indirect optimal control. In *Proc. of the 7th European Control Conf.*, 2003.
- [21] F. Chaplais and N. Petit. Inversion in indirect optimal control: constrained and unconstrained cases. In *Proc. of the 46th IEEE Conf. on Decision and Control*, 2007.
- [22] F. Chaplais and N. Petit. Inversion in indirect optimal control of multivariable systems. *ESAIM: Control, Optimisation and Calculus of Variations*, 14:294–317, 2008.
- [23] J. Cheng, Y. Lu, E. R. Thomas, and J. A. Farrell. Data fusion via Kalman filter: GPS and INS. In Sam. S. Ge and F. L. Lewis, editors, *Autonomous mobile robots*, Control engineering series. Taylor and Francis, 2006.
- [24] Cloud Cap Technologies. <http://www.cloudcaptech.com>. Hood River, OR, USA, 2004.
- [25] L. B. Cremean, T. B. Foote, J. H. Gillula, G. H. Hines, D. Kogan, K. L. Kriechbaum, J. C. Lamb, J. Leibs, L. Lindzey, C. E. Rasmussen, A. D. Stewart, J. W. Burdick, and R. M. Murray. Alice: An information-rich autonomous vehicle for high-speed desert navigation. *Journal of Field Robotics*, (9), 2005.
- [26] P. Fabiani, V. Fuertes, G. Le Besnerais, R. Mampey, A. Piquereau, and F. Teichteil-Königsbuch. ReSSAC: UAV exploring, deciding and landing in a partially known environment. In *IAV 07*, 2007.
- [27] P. Fabiani, V. Fuertes, G. Le Besnerais, A. Piquereau, R. Mampey, and F. Teichteil-Königsbuch. ReSSAC: Flying an autonomous

- helicopter in a non-cooperative uncertain world. In *AHS Specialist Meeting on Unmanned Rotorcraft*, 2007.
- [28] P. Faurre. *Navigation inertielle et filtrage stochastique*. Méthodes mathématiques de l'informatique. Dunod, 1971.
- [29] M. Fliess, J. Lévine, P. Martin, and P. Rouchon. Flatness and defect of nonlinear systems: introductory theory and examples. *Int. J. Control*, 61(6):1327–1361, 1995.
- [30] M. Fliess, J. Lévine, P. Martin, and P. Rouchon. A Lie-Bäcklund approach to equivalence and flatness of nonlinear systems. *IEEE Trans. Automat. Control*, 44:922–937, 1999.
- [31] M. Fruchard, P. Morin, and C. Samson. A framework for the control of nonholonomic mobile manipulators. In *I. J. Robot. Res.* 25(8)., 2006.
- [32] V. Gavrillets, B. Mettler, and E. Feron. Nonlinear model for a small-size acrobatic helicopter. In *AIAA Guidance, Navigation and Control Conference*, 2001.
- [33] V. Gavrillets, B. Mettler, and E. Feron. Human-inspired control logic for automated maneuvering of miniature helicopter. *Journal of Guidance, Control, and Dynamics*, 27(5):752–759, 2004.
- [34] V. Gavrillets, A. Shterenberg, M. A. Dahleh, and E. Feron. Avionics system for a small unmanned helicopter performing aggressive maneuvers. In *19th Digital Avionics Systems Conferences*, 2000.
- [35] M. S. Grewal, L. R. Weill, and A. P. Andrews. *Global positioning systems, inertial navigation, and integration*. Wiley Inter-science, 2001.
- [36] C. Guarino Lo Bianco, A. Piazzzi, and Romano M. Smooth motion generation for unicycle mobile robots via dynamic path inversion. *IEEE Tr. on robotics*, 20(5):884–892, 2004.
- [37] N. Guénard, T. Hamel, and L. Eck. Control laws for the teleoperation of an aerial vehicle known as an X4-Flyer. In *IROS*, 2006.

- [38] N. Guénard, T. Hamel, and R. Mahony. Practical visual servo control for a unmanned aerial vehicle. *IEEE-Transactions on Robotics and Automation*, to appear(): , 2008.
- [39] T. Hamel and R. Mahony. Image based visual servo-control for a class of aerial robotic systems. *Automatica*, 43(11):1975–1983, 2007.
- [40] A. Isidori. *Nonlinear Control Systems*. Springer, New York, 2nd edition, 1989.
- [41] C. Jekeli. Precision free-inertial navigation with gravity compensation by an onboard gradiometer. *J. Guidance, Control and Dynamics*, 29(3):704–713, 2006.
- [42] D. Jung, E. J. Levy, D. Zhou, R. Fink, J. Moshe, A. Earl, and P. Tsiotras. Design and development of a low-cost test-bed for undergraduate education in UAVs. In *Proc. of the 44th IEEE Conf. on Decision and Control, and the European Control Conference 2005*, 2005.
- [43] D. Jung and P. Tsiotras. Inertial attitude and position reference system development for a small UAV. In *AIAA Infotech at Aerospace*, 2007.
- [44] I. Kaminer, O. Yakimenko, V. Dobrokhodov, M. Lizaraga, and A. Pascoal. Cooperative control of small UAVs for naval applications. In *Proc. of the 43rd IEEE Conf. on Decision and Control*, 2004.
- [45] S. Kolb. *Théorie des bifurcations appliquée à l'analyse de la dynamique du vol des hélicoptères*. PhD thesis, Institut National Polytechnique de Grenoble, 2007.
- [46] E. Kyrkjebø and K. Y. Pettersen. Output synchronization control of euler-lagrange systems with nonlinear damping terms. In *Proc. of the 44th IEEE Conf. on Decision and Control, and the European Control Conference 2005*, 2005.

- [47] J.-P. Laumond. Nonholonomic motion planning for mobile robots. In *Proc. of the ICRA 1998, IEEE International Conference on Robotics and Automation*, 1998.
- [48] J.-P. Laumond, P. E. Jacobs, M. Taix, and R. M. Murray. A motion planner for nonholonomic robots. *IEEE T. Robotics and Automation*, 5:577–593, 1994.
- [49] F. Le-Bras, T. Hamel, and R. Mahony. Nonlinear observer-based visual control of a VTOL UAV. In *Proc. of the 9th European Control Conf.*, 2007.
- [50] S. Lee, T. Lee, S. Park, and C. Kee. Flight test results of UAV automatic control using a single-antenna GPS receiver. In *AIAA Guidance, Navigation, and Control Conference and Exhibit*, 2003.
- [51] P. Lefort and J. Hamann. *L'hélicoptère*. Chiron, 2e edition., 1988.
- [52] R. Mahony, T. Hamel, and J.-M. Pflimlin. Complementary filter design on the special orthogonal group $SO(3)$. In *Proc. of the 44th IEEE Conf. on Decision and Control, and the European Control Conference 2005*, 2005.
- [53] P. Martin, S. Devasia, and B. Paden. A different look at output tracking: control of a VTOL aircraft. In *Proc. 33rd IEEE Conf. Decision and Control, San Antonio*, pages 2376–2381, Lake Buena Vista, 1994.
- [54] B. Mettler. *Identification Modeling and Characteristics of Miniature Rotorcraft*. Boston :Kluwer Academic Publishers, 2003.
- [55] B. Mettler, M. B. Tischler, and T. Kanade. Attitude control optimization for a small-scale unmanned helicopter. In *AIAA Guidance, Navigation and Control Conference*, 2000.
- [56] B. Mettler, M. B. Tischler, and T. Kanade. System identification of a model-scale helicopter. Technical Report CMU-RI-TR-00-03, Carnegie Mellon University, january 2000.

- [57] B. Mettler, M. B. Tischler, and T. Kanade. System identification modeling of a small-scale unmanned rotorcraft for flight control design. *Journal of the American Helicopter Society*, 47:50–63, 2002.
- [58] Micro Pilot. <http://www.micropilot.com>. Stony Mountain, Canada, 2004.
- [59] M. B. Milam. *Real-time optimal trajectory generation for constrained systems*. PhD thesis, California Institute of Technology, 2003.
- [60] M. B. Milam, K. Mushambi, and R. M. Murray. A new computational approach to real-time trajectory generation for constrained mechanical systems. In *IEEE Conference on Decision and Control*, 2000.
- [61] K. A. Morgansen and R. W. Brockett. Nonholonomic control based on approximate inversion. In *Proc. of the 1999 American Control Conference*, 1999.
- [62] K. A. Morgansen, P. A. Vela, and J. W. Burdick. Trajectory stabilization for a planar carangiform robot fish. In *Proc. of the ICRA 2002, IEEE International Conference on Robotics and Automation*, 2002.
- [63] P. Morin and C. Samson. Practical stabilization of driftless systems on lie groups: The transverse function approach. *IEEE Transactions on Automatic Control*, 48(9):1496–1508, 2003.
- [64] P. Morin and C. Samson. Control with transverse functions and a single generator of underactuated mechanical systems. In *Proc. of the 45th IEEE Conf. on Decision and Control*, 2006.
- [65] P. Morin and C. Samson. *Trajectory tracking for nonholonomic vehicles*. Robot Motion Control: Recent Developments", K.Kozlowski. Springer, 2006.
- [66] P. Morin and C. Samson. Trajectory tracking for nonholonomic vehicles. In K. Kozlowski, editor, *Robot Motion Control: Recent Developments*. Springer, 2006.

- [67] Motorola. MPC555 / MPC556 user's manual. User's manual, Motorola, 2000.
- [68] R. M. Murray, J. Hauser, A. Jadbabaie, M. B. Milam, N. Petit, W. B. Dunbar, and R. Franz. Online control customization via optimization-based control. In T. Samad and G. Balas, editors, *Software-Enabled Control, Information technology for dynamical systems*, pages 149–174. Wiley-Interscience, 2003.
- [69] A. Y. Ng, A. Coates, M. Diel, V. Ganapathi, J. Schulte, B. Tse, E. Berger, and E. Liang. Inverted autonomous helicopter flight via reinforcement learning. In *International Symposium on Experimental Robotics*, 2004.
- [70] Department of Defense. Network centric warfare. Technical report, Report to Congress, 2001.
- [71] G. D. Padfield. *Helicopter Flight Dynamics*. Blackwell Publishing, 2007.
- [72] E. Panteley, A. Loria, and A. Teel. Relaxed persistency of excitation for uniform asymptotic stability. *IEEE Trans. on Automat. Contr.*, 46(12):1874–1886, 2001.
- [73] N. Petit, M. B. Milam, and R. M. Murray. Inversion based constrained trajectory optimization. In *5th IFAC Symposium on Nonlinear Control Systems*, 2001.
- [74] N. Petit, M. B. Milam, and R. M. Murray. A new computational method for optimal control of a class of constrained systems governed by partial differential equations. In *Proc. of the 15th IFAC World Congress*, 2002.
- [75] K.Y. Pettersen and E. Lefeber. Way-point tracking control of ships. In *Proc. of the 40th IEEE Conf. on Decision and Control*, 2001.
- [76] R. W. Prouty. *Helicopter Performance, Stability, and Control*. Malabar : Krieger Publishing Company Inc., 2003.

- [77] R. Rao, V. Kumar, and C. Taylor. Visual servoing of a UGV from a UAV using differential flatness. In *Proc. of the 2003 IEEE/RSJ Int. Conference on Intelligent Robots and Systems*, 2003.
- [78] K. V. Rozhdestvensky. *Aerodynamics of a Lifting System in Extreme Ground Effect*. 1st Edition, Springer-Verlag, 2000.
- [79] A. Teel, R. M. Murray, and G. C. Walsh. Nonholonomic control systems: from steering to stabilization with sinuoids. *International Journal of Control* 62, 4:849–870, 1995.
- [80] D. Tsakiris, K. Kapellos, C. Samson, P. Rives, and J.-J. Orrelly. *Experiments in Real-time Vision-based Point Stabilization of a Non-holonomic Mobile Manipulator*. Experimental Robotics V: The Fifth International Symposium, A. Casals et A. de Almeida. Springer-Verlag, 1998.
- [81] P. A. Vela, K. A. Morgansen, and J. W. Burdick. Underwater locomotion from oscillatory shape deformations. In *Proc. of the 41th IEEE Conf. on Decision and Control*, 2002.
- [82] D. Vissière, P.-J. Bristeau, A. P. Martin, and N. Petit. Experimental autonomous flight of a small-scaled helicopter using accurate dynamics model and low-cost sensors. In *Proc. of the 17th IFAC World Congress*, 2008.
- [83] D. Vissière, D. E. Chang, and N. Petit. Experiments of trajectory generation and obstacle avoidance for a UGV. In *Proc. of the 2007 American Control Conference*, 2007.
- [84] D. Vissière, A. P. Martin, and N. Petit. Using magnetic disturbances to improve IMU-based position estimation. In *Proc. of the 9th European Control Conf.*, 2007.
- [85] D. Vissière, A. P. Martin, and N. Petit. Using spatially distributed magnetometers to increase IMU-based velocity estimation in perturbed areas. In *Proc. of the 46th IEEE Conf. on Decision and Control*, 2007.

- [86] D. Vissière, A. P. Martin, and N. Petit. Système fournissant vitesse et position d'un corps en utilisant les variations du champ magnétique évaluées grâce aux mesures de un ou des magnétomètres et de une ou des centrales inertielles. In *Brevet n°07/02431*, déposé le 3 avril 2007.
- [87] D. Vissière and N. Petit. Choix des missions. Technical report, Ecole des Mines de Paris-DGA, 2005.
- [88] D. Vissière and N. Petit. Scénarios opérationnels d'emploi des drones. Technical report, Ecole des Mines de Paris-DGA, 2005.
- [89] D. Vissière and N. Petit. Analyse du besoin en positionnement des drones aériens ou terrestres. Technical report, Ecole des Mines de Paris-DGA, 2006.
- [90] D. Vissière and N. Petit. An embedded system for small-scaled autonomous vehicles. In *Proc. of the ICINCO 2008, IEEE International Conference on Informatics in Control, Automation and Robotics*, 2008.
- [91] Y. Xiaokui and Y. Jianping. Study on low-cost GPS/DMU integrated navigation system. In *AIAA/AAS Astrodynamics Specialist Conference and Exhibit*, 2002.
- [92] Y. Yang and J.A. Farrell. Magnetometer and differential carrier phase GPS-aided INS for advanced vehicle control. *IEEE Trans. Robotics Automation*, 19(2):269–282, 2003.
- [93] H. Zhao and R. Shibasaki. A vehicle-borne urban 3-d acquisition system using single-row laser range scanners. *IEEE Trans. on Systems, Man and Cybernetics, Part B*, 33(4):658–666, 2003.